Title
van der Waals Heterostructure Devices — From Two-dimensional Materials to Hybrid Perovskites

Author
Cheng, Hung-Chieh

Publication Date
2016

Peer reviewed|Thesis/dissertation

UNIVERSITY OF CALIFORNIA

Los Angeles

van der Waals Heterostructure Devices —

From Two-dimensional Materials to Hybrid Perovskites

A dissertation submitted in partial satisfaction of the

requirements for the degree Doctor of Philosophy

in Materials Science and Engineering

by

Hung-Chieh Cheng

2016

ABSTRACT OF THE DISSERTATION

van der Waals Heterostructure Devices —

From Two-dimensional Materials to Hybrid Perovskites

by

Hung-Chieh Cheng

Doctor of Philosophy in Materials Science and Engineering

University of California, Los Angeles, 2016

Professor Yu Huang, Chair

Graphene, since its discovery in 2004, has stimulated considerable interest in two-dimensional layered materials research (2DLMs). Various applications have been investigated with the ever-expanding family of 2D materials, ranging from electronic, optoelectronic, sensing, energy storage and catalytic applications, etc. With weak van der Waals forces between layers, generally, 2DLMs can be exfoliated into atomically thin sheets and reassembled in a designed sequence for building artificial heterostructures, namely, van der Waals heterostructures (vdWHs). Except for the most common 2D material — graphene, the building blocks for vdWHs also include semiconductors, insulators and even metallic materials. Such versatility has rendered vdWHs become a promising platform for high performance electronic and optoelectronic devices. Researchers have shown that the devices based vertically stacked vdWHs could be the

candidates for transistors (barristors), photodetectors, light-emitting diodes and flexible electronics, etc. Particularly, the unique electronic properties of graphene have been playing very important roles in these vertically stacked vdWH devices. In addition to the transparency and extraordinary electrical conductivity of graphene, the work function of graphene can be modulated by varying the gate electric field, enabling a tunable electrical contact with other materials. With the experience we have built up with 2D materials, we further explored the possibilities of integrating a new category of materials – organic-inorganic hybrid perovskites. The hybrid perovskites are the newly emerging materials for high performance optoelectronic applications, which are mostly investigated for solar cell applications. The perovskite based solar cells have shown an astonishing improvement in power conversion efficiency from 3.8 to 22.1% in just few years. Such prominent performance has attracted tremendous research interests from different perspectives. However, these perovskite materials are generally not compatible with conventional nanodevice fabrication due to their considerable solubility in polar organic solvent and water. Despite such fabrication difficulties, we have proposed several approaches to fabricate electronic and optoelectronic devices based on the integration of perovskites and 2D materials.

In this dissertation, I will show how we develop a universal water-free dry transfer method to solve the fabrication problems of perovskites and how we build new types of vdWHs with perovskites and 2D materials. We have realized the first van der Waals heterojunction devices based on perovskites and 2D materials, and achieved a high photo-responsivity (950 A/W) and a very high photoconductive gain (~2200) with graphene/perovskite/graphene vertical structure. Moreover, a unique and prominent gate-

tunable photovoltaic effect has been observed in the vertically stacked perovskite/WSe_2 heterojunction devices. Finally, we have investigated the doping effect induced by ionic solid and the ion migration in perovskites. A switchable p-n junction formation has been demonstrated on a monolayer WSe_2 device by electrical poling, along with a very high external quantum efficiency up to 93% under the excitation of 532 nm laser. I believe that in the near future, such platform can enable more possibilities in both electronic and optoelectronic applications with the expanding 2D materials family and hybrid perovskites with compositional tunability.

The dissertation of Hung-Chieh Cheng is approved.

Dwight C. Streit

Paul S. Weiss

Xiangfeng Duan

Yu Huang, Committee Chair

University of California, Los Angeles

2016

Table of Contents

List of Figures

ACKNOWLEDGEMENTS

First and foremost, I am deeply indebted to my PhD advisor Professor Yu Huang for giving me this great opportunity to join her lab, where I met so many talented people and outstanding researchers. I will never forget her patience and invaluable guidance over these years, and the mentorship and financial support she had provided throughout my PhD studies. I would also like to express my sincere appreciation to Professor Xiangfeng Duan for his insightful advice and guidance on my research projects. He taught me how to tackle difficult problems in the most efficient way while still picking up valuable details from various perspectives. I am also thankful to his patience allowing me to have enough time to explore new things as well as developing my problem-solving skills. Without their inspiration and support, I could not have accomplished my PhD studies.

I would additionally like to extend my sincere gratitude to the committee members in my PhD qualifying and defense exam, Professors Dwight C. Streit and Paul S. Weiss, for spending their precious time participating my qualifying and defense exam as well as reading my dissertation and providing their valuable comments and feedback. It is such a great honor for me to have both Prof. Streit, who is the former vice president of Northrop Grumman, and Prof. Weiss, who is the editor-in-chief of ACS Nano, to review my dissertation.

I feel very fortunate to work with many great people from both Prof. Huang and Prof. Duan's group. Dr. Dehui Li, Yuan Liu, Qiyuan He, Woojong Yu, Mengning Ding and Rui Cheng have been very helpful when I encountered problems in my research projects. Your insightful suggestions and valuable experience have become a very strong support in my PhD research. I would like to express my special thanks to Dr. Yu Chen,

who is always willing to listen and share his experience to me since I have been in the US. I also want to thank my dear friend and roommate Enbo Zhu for your company and your help on anything during these days, you are one of the most generous and kind people I have ever met. Thanks to Hao, I will never forget those night we stayed up and worked for the silicide project. I also enjoyed the time we took classes together with Jianjin Dong, who is a former master student in the group. I appreciate Dr. Zheng Fan, who is always willing to help me with TEM and SEM. I also want to thank Dr. Chin-Yi Chiu for giving me useful suggestions for my future career, and Dr. Gongming Wang, Anxiang Yin and Jonathan Shaw for their help on the experimental setup for my projects. Thanks to Chen Wang for his maintenance on several instruments in the lab, and also Dr. Zhaoyang Lin for his help on all sorts of matters regarding chemistry department. I would also like to thank Dr. Wei-Hsuan Chang from Professor Yang Yang's group for his help in my early days of study and life in LA.

I also want to thank some of the former and current group members from MSE and Chemistry department for your help and company during my PhD study, Zipeng Zhao, Hui-Ying Shiu, Yun-Chiao Huang, Jiming Sheng, Jian Guo, Nathan Weiss, Ya-Hsuan Chuang, Yue-Shun Su, Udayabagya Halim, Chain Lee, Ben Papandrea, Freda Lam, Michelle Flores, Sung-Joon Lee, Hyunpil Boo, Chung Suk Choi, Mufan Li, and Dr. Yung-Chen Lin, Hailong Zhou, Gang Liu, Teng Xue, Shan Jiang, Yongjia Li and Lingyan Ruan as well as some visiting scholars from China, Dr. Hong Zhou, Shengnan Lu, Yang Xu, Yu Zhang and Shengxue Yang. Thank you all for making these days memorable and colorful.

Finally, I would like to extend my deepest gratitude to my grandmother, who raised me with love and care. I also want to thank my parents, my parents-in-law and brother-in-

law for their unconditional support of my life in the US. And most of all, my wife Lin-Han, who quit her high-paying job in Taiwan and moved to me. During these days, I am deeply grateful to her for her love, patience and understanding of my pressure and absence for the research projects even at night and weekend. I couldn't have asked for a better wife! Without her encouragement and support, I could never have completed my PhD study.

BIOGRAPHY

Hung-Chieh Cheng received his M.S. and B.S. in Materials Science and Engineering from National Tsing Hua University, Hsinchu, Taiwan in 2007 and 2005, respectively. He joined Professor Yu Huang's group in 2011 (co-advised by Professor Xiangfeng Duan) and conducted the research of van der Waals heterostructures based electronic and optoelectronic devices. Prior to doctoral studies, he was a research assistant at the Institute of Atomic and Molecular Sciences, Academia Sinica, Taipei, Taiwan where he conducted research on synthesis of silicon nanowires and biosensor studies based on graphene and silicon nanowires. He has two-conference papers, two first-author and 13 co-author papers published in peer-reviewed journals. He gave an oral presentation in the Conference on Lasers and Electro-Optics (CLEO:2016) in San Jose. His research interests include low-dimensional materials based electronic and optoelectronic devices.

INTRODUCTION

van der Waals heterostructures (vdWHs) based on graphene and other two-dimensional 2D layered materials (2DLMs) have sparked considerable interest in recently new designs of various electronic device applications including transistors, barristors and flexible electronics.[1-4] On the other hand, optoelectronic device applications such as photodetectors and light-emitting diodes have also attracted wide attention.[5-8] Distinct from traditional heterostructures formed by direct deposition or epitaxy, vdWHs allow highly disparate materials to stack layer by layer without the consideration of lattice matching.[1, 2, 9] In addition, the building blocks of vdWHs can range from 0D (such as nanoparticles or quantum dots), 1D (nanowires or nanotubes), 2D (layered materials) to 3D (bulk materials).[2] Various materials can be integrated and held together by van der Waals forces with the desired stacking order through specifically designed materials transfer method. The state-of-art material transfer methods are capable of integrating materials in any desired angles and positions with sub-micrometer accuracy, enabling a broad range of fundamental device studies with the combination of new materials. In such vdWHs based devices, graphene is widely adopted as the electrodes for the devices due to its semi-metal nature and finite density of states, which allows external tunability on its work function.[2-4, 8, 10-13] For example, the first graphene/boron nitride (BN) based tunneling transistors have opened up a new avenue toward tunable vertically stacked heterostructures devices.[10] With the external electrical field applying from the back-gate, the electrical tunneling through an atomically thin BN layer across two superimposed graphene layer is controllable through externally applied electric field. Such tunable properties of graphene have triggered further device studies on the unique vertical transport, including resonant

tunneling transistors, barristors, and etc.[3, 4, 11, 14] These new type of transistors have been investigated by incorporating with a traditional bulk semiconductors and other two-dimensional materials, such as the transition metal dichalcogenides (TMDCs).[3, 4, 11] Unlike gapless graphene, these TMDCs may have finite band gaps ranging from the visible to the near-infrared region, enabling vast intriguing applications including vertical transistors, photodetectors and light-emitting diodes.[3, 4, 6-8, 10, 11] For examples, vertical transistors based on molybdenum disulfide (MoS_2) has been shown to carry high current density with an ON-OFF ratio over 10^3, such vertical based transport also enables the design of flexible electronics.[11, 15] On the hand, the vertical configuration of such devices is especially benefit to the optoelectronic applications which usually requires a maximized photosensitive area. From the efficiency point of view, the collection or injection of carriers in vdWHs based optoelectronic devices can be further optimized by the tunable and transparent graphene contact and thus higher efficiency can be achieved through the controllable external electric field.[8] Such design strategy with the use of graphene has set up a paradigm in future vdWHs based optoelectronic devices. For some optoelectronic applications, such as light-emitting devices, usually requires a direct band gap semiconductor as the photoactive layer for effective radiative recombination of electron-hole pairs. However, the widely used TMDCs materials are mostly indirect band gap materials except for their monolayers. To insert a monolayer TMDC into two graphene layers would result in considerable tunneling between top and bottom graphene layers, which is not suitable for light emission that requires efficient carrier injection and recombination.

Recently, a new category of direct band gap materials has emerged in solar cell research with a remarkable high power-conversion efficiency of over 22%.[16-19] This type

of materials is a hybrid organic-inorganic perovskite, consisting of organic components sitting in large interstices between inorganic octahedra formed by lead (or tin) halides. These perovskites have several advantages in terms of optoelectronic properties, including high optical absorption coefficient and long carrier diffusion length.[16, 18, 20] However, these perovskites are not very stable in ambient condition due to irreversible degradation induced by moisture. Another issue is that these perovskites can be dissolved in the most popular solvents, such as acetone, alcohols and water, thus they are not compatible with traditional nanodevice fabrication process.[12] In this dissertation, I will present my efforts to overcome these fabrication difficulties and build vdWHs devices based on organic-inorganic hybrid perovskites and 2DLMs through conventional nanodevice fabrication process, as well as studying their fundamental electronic and optoelectronic properties. The integration of 2DLMs and perovskites could be even more versatile because of ever-expanding family of 2DLMs and compositional tunable band structures of perovskite materials. I believe these findings can serve as a new type of vdWHs devices for future high performance electronic and optoelectronic devices.

References

1. Geim, A. K.; Grigorieva, I. V. *Nature* **2013,** 499, (7459), 419-425.
2. Liu, Y.; Weiss, N. O.; Duan, X.; Cheng, H.-C.; Huang, Y.; Duan, X. *Nature Reviews Materials* **2016,** 1, 16042.
3. Yang, H.; Heo, J.; Park, S.; Song, H. J.; Seo, D. H.; Byun, K.-E.; Kim, P.; Yoo, I.; Chung, H.-J.; Kim, K. *Science* **2012,** 336, (6085), 1140.
4. Yu, W. J.; Li, Z.; Zhou, H.; Chen, Y.; Wang, Y.; Huang, Y.; Duan, X. *Nature Mater.* **2013,** 12, (3), 246-252.
5. Britnell, L.; Ribeiro, R. M.; Eckmann, A.; Jalil, R.; Belle, B. D.; Mishchenko, A.; Kim, Y. J.; Gorbachev, R. V.; Georgiou, T.; Morozov, S. V.; Grigorenko, A. N.; Geim, A. K.; Casiraghi, C.; Neto, A. H. C.; Novoselov, K. S. *Science* **2013,** 340, (6138), 1311.
6. Withers, F.; Del Pozo-Zamudio, O.; Mishchenko, A.; Rooney, A. P.; Gholinia, A.; Watanabe, K.; Taniguchi, T.; Haigh, S. J.; Geim, A. K.; Tartakovskii, A. I.; Novoselov, K. S. *Nature Mater.* **2015,** 14, (3), 301-306.
7. Withers, F.; Del Pozo-Zamudio, O.; Schwarz, S.; Dufferwiel, S.; Walker, P. M.; Godde, T.; Rooney, A. P.; Gholinia, A.; Woods, C. R.; Blake, P.; Haigh, S. J.; Watanabe, K.; Taniguchi, T.; Aleiner, I. L.; Geim, A. K.; Fal'ko, V. I.; Tartakovskii, A. I.; Novoselov, K. S. *Nano Lett.* **2015,** 15, (12), 8223-8228.
8. Yu, W. J.; Liu, Y.; Zhou, H.; Yin, A.; Li, Z.; Huang, Y.; Duan, X. *Nature Nanotech.* **2013,** 8, (12), 952-958.
9. Novoselov, K. S.; Mishchenko, A.; Carvalho, A.; Castro Neto, A. H. *Science* **2016,** 353, (6298).

10. Britnell, L.; Gorbachev, R. V.; Jalil, R.; Belle, B. D.; Schedin, F.; Mishchenko, A.; Georgiou, T.; Katsnelson, M. I.; Eaves, L.; Morozov, S. V.; Peres, N. M. R.; Leist, J.; Geim, A. K.; Novoselov, K. S.; Ponomarenko, L. A. *Science* **2012,** 335, (6071), 947.
11. Georgiou, T.; Jalil, R.; Belle, B. D.; Britnell, L.; Gorbachev, R. V.; Morozov, S. V.; Kim, Y.-J.; Gholinia, A.; Haigh, S. J.; Makarovsky, O.; Eaves, L.; Ponomarenko, L. A.; Geim, A. K.; Novoselov, K. S.; Mishchenko, A. *Nature Nanotech.* **2013,** 8, (2), 100-103.
12. Cheng, H.-C.; Wang, G.; Li, D.; He, Q.; Yin, A.; Liu, Y.; Wu, H.; Ding, M.; Huang, Y.; Duan, X. *Nano Lett.* **2016,** 16, (1), 367-373.
13. Liu, Y.; Wu, H.; Cheng, H.-C.; Yang, S.; Zhu, E.; He, Q.; Ding, M.; Li, D.; Guo, J.; Weiss, N. O.; Huang, Y.; Duan, X. *Nano Lett.* **2015,** 15, (5), 3030-3034.
14. Britnell, L.; Gorbachev, R. V.; Geim, A. K.; Ponomarenko, L. A.; Mishchenko, A.; Greenaway, M. T.; Fromhold, T. M.; Novoselov, K. S.; Eaves, L. *Nat. Commun.* **2013,** 4, 1794.
15. Liu, Y.; Zhou, H.; Cheng, R.; Yu, W.; Huang, Y.; Duan, X. *Nano Lett.* **2014,** 14, (3), 1413-1418.
16. Dong, Q.; Fang, Y.; Shao, Y.; Mulligan, P.; Qiu, J.; Cao, L.; Huang, J. *Science* **2015,** 347, (6225), 967.
17. Lee, M. M.; Teuscher, J.; Miyasaka, T.; Murakami, T. N.; Snaith, H. J. *Science* **2012,** 338, (6107), 643.
18. Stranks, S. D.; Eperon, G. E.; Grancini, G.; Menelaou, C.; Alcocer, M. J. P.; Leijtens, T.; Herz, L. M.; Petrozza, A.; Snaith, H. J. *Science* **2013,** 342, (6156), 341.

19. Yang, W. S.; Noh, J. H.; Jeon, N. J.; Kim, Y. C.; Ryu, S.; Seo, J.; Seok, S. I. *Science* **2015,** 348, (6240), 1234.

20. De Wolf, S.; Holovsky, J.; Moon, S.-J.; Löper, P.; Niesen, B.; Ledinsky, M.; Haug, F.-J.; Yum, J.-H.; Ballif, C. *J. Phys. Chem. Lett.* **2014,** 5, (6), 1035-1039.

CHAPTER I: WATER-FREE DRY-TRANSFER APPROACH FOR BUILDING VAN DER WAALS HETEROSTRUCTURE DEVICES

A. Introduction

Graphene and other two-dimensional layered materials (2DLMs) have recently become attractive building blocks for heterostructure devices due to their unique geometry and unusual physical properties.[1-4] For example, graphene is one of the strongest materials in the world, along with remarkable electrical conductivity, finite density of states and partial optical and electrostatic transparency, rendering it a promising candidate for transparent and work-function tunable electrode for vdWH based devices.[5-12] On the other hand, similar to graphene, other 2DLMs can also be exfoliated into atomically thin flakes. These 2DLMs can be metallic materials, semiconductors or even insulators, enabling various designs for high performance electronic or optoelectronic devices.[9, 13] In order to integrate different types of nanomaterials, a material transfer method is usually required.[7, 9, 14-16] In general, a material transfer method involves two main manipulations of nanostructured materials, namely, "pickup" and "release". Such manipulations require the understanding of the van der Waals force interaction between the material of interest (MOI) and the target materials. To realize such manipulations, transfer mediums include polydimethylsiloxane (PDMS) and poly(methyl methacrylate) (PMMA) are the mostly adopted solutions for material transfer.[9, 16]

PDMS-based transfer

PDMS is a highly transparent polymer, which can be easily cured into different shapes with specially designed molds, along with a hydrophobic nature and low surface

energy surface (~19.8 mJ/m^2).[17] This hydrophobic nature of PDMS can facilitate the removal of hydrophobic materials from hydrophilic substrate, similar approaches has been used in wedging transfer and PDMS-assisted transfer.[18, 19] Moreover, the viscoelasticity of PDMS allows rate-determined adhesion forces to the MOI. A rapid acquisition of MOI gives a stronger adhesion between PDMS and MOI, so that MOI can be picked up by the PDMS.[20] In contrast, a slow retraction of PDMS after the MOI has been engaged with the target can release/print the MOI on the target materials. Such properties of PDMS has been widely applied in transfer printing approach.[21]

PMMA-based transfer

On the other hand, PMMA is known as widely adopted positive tone polymer resist with high transparency for electron-beam lithography (EBL). PMMA is usually prepared by dissolving solid-state polymer powder in an organic solvent, which can be spun onto different substrates and dissolve in acetone easily. Its hydrophobic nature also renders it the mostly used transfer medium in chemical vapor deposition (CVD) grown graphene and other 2DLMs.[22] In CVD grown 2DLMs, the materials usually grow on a substrate where cannot be directly used as the device substrate. Thus, relocation of materials is needed to bring MOI to another target substrate for further studies. The growth substrates are usually dissolved in a water-based etchant, allowing the hydrophobic PMMA layer to strip MOI from the growth substrate and float on the water/etchant surface. Then the target substrate is inserted under the floating PMMA, followed by scooping up the floating PMMA (with MOI). The target substrate is then pulled out of water, and dried to ensure MOI is attached to the target substrate. The MOI can now be used for further studies after dissolving the carrier PMMA.

Aligned transfer of materials

In 2010, Dean C. R. *et al.* reported an approach to transfer an exfoliated graphene monolayer to a hexagonal boron-nitride (h-BN) flakes.[15] Since both the exfoliated graphene and hexagonal boron nitride are randomly distributed on the substrate, a positioning transfer method is required. They first exfoliated graphene on the top of PMMA sitting on a water-soluble layer coated substrate. Then a glass slide with a small opening is used to scoop up the floating PMMA membrane (with graphene facing up), which allows PMMA membrane to suspend over the opening. Subsequently, the suspended PMMA membrane is turned upside down and aligned to face the target. The PMMA membrane with graphene is then brought into contact with the target h-BN substrate. After heating up the substrate, the PMMA layer (with graphene) is released and attached to the target substrate. This approach has opened up many new possibilities toward building complex vdWHs as well as enabling novel studies on the physical properties of various atomically thin heterostructures.

B. A water-free dry transfer approach

In order to investigate the unique properties of vdWHs, a precise layer-by-layer assembly approach is a crucial step to build a variety of heterostructures.[7, 9] The aforementioned transfer method using glass slide with suspended PMMA membrane has been demonstrated to have few micrometers accuracy of the desired position. However, the rigid glass slide is difficult to perfectly reach the target. To ensure complete contact between glass slide and the target substrate, the transfer setup (including micromanipulators) has to be dedicated to a microscope after strict alignment process.

Some transfer setups are even integrated with commercial mask aligner to ensure a perfect alignment for both surfaces.[23] To address on this problem, PDMS stamp has emerged to become a possible solution to resolve this problem since it can adapt to the surface of the target substrate, which facilitates the engagement of both surface.[16] However, unlike hydrophilic glass slide, PDMS stamp is extremely hydrophobic, causing problems when transferring PMMA onto PDMS stamp in water. Due to hydrophobic effect, the PMMA layers are always get wrinkled as they are scooped up from water surface by PDMS stamps. Another issue with water-assisted transfer is that some materials are inherently vulnerable to water or even water-soluble, such as some ionic solids including lead halides and organohalide perovskites. In addition, these materials are also hydrophilic, making them difficult to be stripped from hydrophilic substrate (e.g., silicon oxide) by a hydrophobic PMMA or PDMS. To address on these problems, a universal, water-free dry transfer is of interest to develop. Here I proposed a completely dry materials transfer method, which can be applied to all kinds of 2DLMs and most nanostructured materials. Figure 1-1 is the schematic illustration of my transfer setup. To realize a completely dry process, we investigated the possibility to directly lift PMMA layer (with MOI on top) off from silicon wafer. The feasibility to separate PMMA from substrate is determined by the surface energy of silicon wafer. In general, substrates with lower surface energy can facilitate the removal of PMMA layer, however, a surface with low surface energy also has low wettability for PMMA to spread during spin-coating, such as PDMS surface. Self-assembly monolayer (SAM) is known as an effective treatment to change the surface properties of silicon wafer. In our study, two different types of SAMs were investigated, including octadecyltrichlorosilane (OTS) and hexamethyldisilazane (HMDS). It has been reported

that the surface energy of bare SiO_2 substrate, HMDS and OTS functionalized ones are 61.4, 43.6 and 28.1 mJ/m^2 respectively.[24] As expected, PMMA was completely thrown off the OTS-treated wafer during spin-coating process because of its low surface energy. On the other hand, PMMA can be spin-coated on both bare SiO_2 and HMDS-treated substrate. Moreover, HMDS-treated substrate allows mechanical peel-off of the PMMA without the sacrificial layer involved. More importantly, the HMDS-substrate is completely reusable even immediately after each peel-off (see the full process in Figure 1-2). Unlike traditional water-assisted transfer requiring water-soluble layer, no additional cleaning or regeneration process is required for our HMDS-assisted process.

C. van der Waals heterostructure devices using graphene as the contact electrodes

To explore the unique electronic properties of 2DLMs, there has been a rapid growth of device research centered on two-dimensional semiconductors (2DSC).[3, 25-27] Some transition metal dichalcogenides (TMDCs) such as MoS_2 and WSe_2 are the most studied 2DSCs.[3] However, it has been shown that the electrical properties of TMDC devices are largely dominated by the electrical contacts.[25-28] To achieve the best performance of the device, a number of metals were investigated as contacts for the devices. In general, metals with lower work function forms lower Schottky barrier with n-type 2DSC (e.g., MoS_2).[26] However, in some cases, such as monolayer of few-layer MoS_2, energetic deposition of metal may change or damage the covalent bonds of MoS_2 and introduce defects into atomically thin lattice, resulting in Fermi-level pinning and large contact resistance.[25] Recently, graphene has been reported as an alternative for contact materials due to its high conductivity and unique, gapless band structure. In particular,

graphene provides a non-destructive contact, and the work function of graphene can be modulated because of its finite density of states and linear dispersion relationship, making graphene an attractive candidate for 2DSCs.[5, 6, 8-12, 14, 25, 29-31]

D. Lateral van der Waals heterostructure devices

In a recent study, we investigated the MoS_2 field-effect transistors with graphene as electrical contacts. We have demonstrated that zero contact barrier can be achieved in monolayer and multilayer MoS_2 field-effect transistor even down to 1.9 K, and observed a metal-insulator transition (MIT) in two-terminal devices.[25]

To fabricate the device, two neighboring monolayer graphene strips were first exfoliated the silicon oxide (300 nm)/highly doped silicon substrate. Followed by transferring a MoS_2 flake with our HMDS-assisted dry transfer method. The electrodes were defined on top of graphene by electron-beam lithography and Cr/Au (20nm/80nm) evaporation. Figure 1-3 shows current-voltage characteristics of a monolayer and a 20 layers MoS_2 devices with bottom monolayer graphene contacts. Linear I-V curves are observed in both 1L and 20L devices, even at 1.9K, indicating complete elimination of the Schottky barrier. With low barrier contacts at low temperature, we were able to observe MIT in monolayer and multilayer devices, As shown in Figure 1-4, the conductivity monotonically decreases with temperature at lower gate voltage, indicating an insulating characteristic. In contrast, both 1L and 20L devices show metallic behavior as the conductivity increases with decreasing temperature at high gate voltage. These characteristics may not be easily observed in non-ideal metal contacts.

To explore and optimize the device performance further, we encapsulated the devices with top and bottom boron nitride (BN). For BN encapsulated devices, the top BN was first exfoliated on the top of polymer stack PMMA/PPC (polypropylene carbonate) on HMDS-functionalized substrate. After slowly peeling off the polymer stack (with top BN), the polymer stack was attached to a PDMS adhered glass slide. The glass slide is then used to pick up a separately prepared MoS_2 strip and two graphene electrodes. Finally, the top BN/MoS_2/graphene stack was transferred to a bottom BN layer sitting on a silicon oxide/highly-doped silicon substrate. Since the graphene strips were covered by top BN layer, two edge contacts were formed by etching BN/graphene/BN stack with CHF_3/O_2 plasma, followed by standard metal evaporation as previously described.

Despite the fact that the barriers are minimized in our graphene contacts devices, we note that the contact resistance could still play a substantial role in limiting two-terminal device performance. In order to probe the intrinsic carrier mobility, we examine field-effect mobility through the following equation.

$$\mu = \frac{L}{W} \cdot \frac{1}{CV_{DS}} \cdot \frac{dI_{DS}}{dV_G}$$

To minimize the contribution from contact resistance, we adopted a large L/W ratio (35 μm/1.7 μm) device. As shown in Figure 1-5, a long channel BN-encapsulated MoS_2 device was connected by two graphene flakes *via* edge contacts. The carrier mobility of this device can reach up to 1300 $cm^2/(V.s)$ at 1.9 K, which is a record high extrinsic field-effect mobility in MoS_2 based field-effect transistor.

In summary, we have achieved a barrier-free electrical contacts for MoS_2 with work function tunable graphene electrodes. In addition to tunable work function, with atomically smooth and dangling bond-free surface, graphene holds great promise as an excellent

electrical contact for electronic devices with ultrathin thickness. The low optical absorption of graphene in visible range also renders graphene as a candidate for transparent electrodes.

E. Vertical van der Waals heterostructure devices

Electronics

As the earliest 2DLM, graphene has attract considerable interest in various electronic applications, due to its exceptional electronic properties in atomically thin structure.[2, 15, 16] This two-dimensional sheets of carbon atoms was once considered to be a promising candidate for post-silicon electronics.[2, 32] However, the gapless, metallic nature of graphene has hampered its development in integrated electronics. To achieve high ON-OFF ratios, a vertical tunneling transistor based graphene/hexagonal boron nitride (h-BN) or molybdenum disulfide (MoS_2)/graphene heterostructure was proposed.[5] The vertical transport between top a bottom graphene is measured under different back-gate voltage. As the back-gate voltage is applied, the bottom and top graphene are unevenly doped by the varying bottom gate field. Specifically, due to the finite density of states and large quantum capacitance graphene, the work functions of bottom graphene can be readily modulated by the bottom gate, on the other hand, the top graphene is less "doped" by the bottom gate.[5, 8-12] In this case, the asymmetric contacts were formed at the top and bottom sides of h-BN or MoS_2, resulting a non-zero current flow at zero bias condition. In addition to gate-tunable work function of graphene, the barrier height of vertical transport can be further modulated by external bias voltage, resulting a large ON-OFF ratio. A 10^4 ON-OFF ration is achieved by using graphene/MoS_2/graphene vertical structure.[5] With tunable work function, unlike metals, graphene can form gate-tunable Schottky barrier with

semiconductors. The earliest barristor based on graphene/silicon has reached a ON-OFF ratio of 10^5 by effectively modulating the barrier height, thus enabling large shifts of diode threshold voltages.[10] In our previous study, we reported vertical field-effect transistor study with metal/MoS_2/graphene structures.[11] With asymmetric top (metal) and bottom (graphene) electrodes, the bias voltages with different polarity show distinct response to the external gate electric field. As depicted in Fig. 1-6, the bias voltage is applied to the bottom graphene electrode, whereas the top metal electrode is grounded. When bias voltage is positive, the device current is determined by the injecting electrons from the top metal electrode, which can hardly be modulated by the back-gate electric field because of effective Fermi level pinning and strong screening effect by the metal electrode. On the other hand, as the bias voltage is negative, the device current is now determined by the electron injection barrier at graphene/MoS_2 interface, which can be effectively modulated by the back-gate electric field owing to the tunable work function of graphene. With this device structure, a high current density over 5,000 A/cm^2 and a room temperature ON-OFF ratio > 10^3 was achieved.[11] These studies have confirmed a new paradigm of designing graphene based electronic devices, opening up a new avenue for future vdWH based devices.

Optoelectronics

In traditional optoelectronic devices, layer-by-layer, vertical configurations are mostly adopted in order to maximize the photoactive area. A typical optoelectronic device structure requires a p-n junction with at least one side of the electrode is transparent. In modern p-n junction designs, as shown in Figure 1-7, the junction can be further divided into effective electron and hole injection/transport layers and a photoactive layer to

emit/absorb the light. In vdWHs, graphene can serve a transparent electrode due to its high conductivity and low optical absorption in visible range. In a graphene/MoS_2/graphene (GMG) vertical device as shown in Fig. 1-8, the work function of bottom graphene can be electrostatically modulated by the bottom gate field, while the top graphene is less affected and can serve a transparent electrode allowing light to penetrate through the device. Due to a work function difference in top and bottom graphene, an internal field is established, which allows light excited electron-hole pairs to be separated and collected by both graphene electrodes. In heterostructure photodetectors devices, the band structure of each layers should be matched to achieve high carrier collection efficiency. With tunable work function, graphene offers an extra tunability to further optimize the efficiency. The external quantum efficiency of GMG structure is also tunable by varying the gate-voltage, and a EQE of 55% was demonstrated.[12] The vertical device structures with graphene contacts are the new design paradigms paving the way to future high performance vdWH based optoelectronics. Further optimization can be implemented by integrating new photoactive materials and better carrier collection/transport layers in graphene sandwich structures.

F. Summary

van der Waals heterostructures (vdWHs) is of great interest because of the availability to study atomic scale heterostructures without using expensive, state-of-art deposition technology. Unlike conventional heterostructures that requires the consideration of lattice matching, vdWHs allow a quick assessment of newly designed heterostructures built by different layered materials. In this chapter, we discussed our development with a new water-free dry transfer approach, which holds a great promise to facilitate the device

fabrication of some water-sensitive materials and could offer a design paradigm for any low-dimensional materials including 0D, 1D, 2D and 3D (bulk) materials. In addition, with tunable work function, graphene contact has been investigated as a promising alternative to conventional metal contact, along with its transparency and high conductivity. With our material transfer approach, we are able to further explore more diverse functional materials as well as opening up new opportunities for next generation electronics research.

G. Reference

1. Lopez-Sanchez, O.; Lembke, D.; Kayci, M.; Radenovic, A.; Kis, A. *Nature Nanotech.* **2013,** 8, (7), 497-501.
2. Novoselov, K. S.; Geim, A. K.; Morozov, S. V.; Jiang, D.; Zhang, Y.; Dubonos, S. V.; Grigorieva, I. V.; Firsov, A. A. *Science* **2004,** 306, (5696), 666.
3. RadisavljevicB; RadenovicA; BrivioJ; GiacomettiV; KisA. *Nature Nanotech.* **2011,** 6, (3), 147-150.
4. Wang, Q. H.; Kalantar-Zadeh, K.; Kis, A.; Coleman, J. N.; Strano, M. S. *Nature Nanotech.* **2012,** 7, (11), 699-712.
5. Britnell, L.; Gorbachev, R. V.; Jalil, R.; Belle, B. D.; Schedin, F.; Mishchenko, A.; Georgiou, T.; Katsnelson, M. I.; Eaves, L.; Morozov, S. V.; Peres, N. M. R.; Leist, J.; Geim, A. K.; Novoselov, K. S.; Ponomarenko, L. A. *Science* **2012,** 335, (6071), 947.
6. Britnell, L.; Ribeiro, R. M.; Eckmann, A.; Jalil, R.; Belle, B. D.; Mishchenko, A.; Kim, Y. J.; Gorbachev, R. V.; Georgiou, T.; Morozov, S. V.; Grigorenko, A. N.; Geim, A. K.; Casiraghi, C.; Neto, A. H. C.; Novoselov, K. S. *Science* **2013,** 340, (6138), 1311.
7. Novoselov, K. S.; Mishchenko, A.; Carvalho, A.; Castro Neto, A. H. *Science* **2016,** 353, (6298).
8. Georgiou, T.; Jalil, R.; Belle, B. D.; Britnell, L.; Gorbachev, R. V.; Morozov, S. V.; Kim, Y.-J.; Gholinia, A.; Haigh, S. J.; Makarovsky, O.; Eaves, L.; Ponomarenko, L. A.; Geim, A. K.; Novoselov, K. S.; Mishchenko, A. *Nature Nanotech.* **2013,** 8, (2), 100-103.

9. Liu, Y.; Weiss, N. O.; Duan, X.; Cheng, H.-C.; Huang, Y.; Duan, X. *Nature Reviews Materials* **2016,** 1, 16042.

10. Yang, H.; Heo, J.; Park, S.; Song, H. J.; Seo, D. H.; Byun, K.-E.; Kim, P.; Yoo, I.; Chung, H.-J.; Kim, K. *Science* **2012,** 336, (6085), 1140.

11. Yu, W. J.; Li, Z.; Zhou, H.; Chen, Y.; Wang, Y.; Huang, Y.; Duan, X. *Nature Mater.* **2013,** 12, (3), 246-252.

12. Yu, W. J.; Liu, Y.; Zhou, H.; Yin, A.; Li, Z.; Huang, Y.; Duan, X. *Nature Nanotech.* **2013,** 8, (12), 952-958.

13. Geim, A. K.; Grigorieva, I. V. *Nature* **2013,** 499, (7459), 419-425.

14. Cheng, H.-C.; Wang, G.; Li, D.; He, Q.; Yin, A.; Liu, Y.; Wu, H.; Ding, M.; Huang, Y.; Duan, X. *Nano Lett.* **2016,** 16, (1), 367-373.

15. Dean, C. R.; Young, A. F.; MericI; LeeC; WangL; SorgenfreiS; WatanabeK; TaniguchiT; KimP; Shepard, K. L.; HoneJ. *Nature Nanotech.* **2010,** 5, (10), 722-726.

16. Wang, L.; Meric, I.; Huang, P. Y.; Gao, Q.; Gao, Y.; Tran, H.; Taniguchi, T.; Watanabe, K.; Campos, L. M.; Muller, D. A.; Guo, J.; Kim, P.; Hone, J.; Shepard, K. L.; Dean, C. R. *Science* **2013,** 342, (6158), 614.

17. van Krevelen, D. W. *Properties of Polymers* (Elsevier, Amsterdam, 1997).

18. Li, H.; Wu, J.; Huang, X.; Yin, Z.; Liu, J.; Zhang, H. *ACS Nano* **2014,** 8, (7), 6563-6570.

19. Schneider, G. F.; Calado, V. E.; Zandbergen, H.; Vandersypen, L. M. K.; Dekker, C. *Nano Lett.* **2010,** 10, (5), 1912-1916.

20. Andres, C.-G.; Michele, B.; Rianda, M.; Vibhor, S.; Laurens, J.; Herre, S. J. v. d. Z.; Gary, A. S. *2D Materials* **2014,** 1, (1), 011002.

21. Meitl, M. A.; Zhu, Z.-T.; Kumar, V.; Lee, K. J.; Feng, X.; Huang, Y. Y.; Adesida, I.; Nuzzo, R. G.; Rogers, J. A. *Nature Mater.* **2006,** 5, (1), 33-38.

22. Jiao, L.; Fan, B.; Xian, X.; Wu, Z.; Zhang, J.; Liu, Z. *J. Am. Chem. Soc.* **2008,** 130, (38), 12612-12613.

23. Zomer, P. J.; Dash, S. P.; Tombros, N.; van Wees, B. J. *Appl. Phys. Lett.* **2011,** 99, (23), 232104.

24. Yoshikawa, G.; Sadowski, J. T.; Al-Mahboob, A.; Fujikawa, Y.; Sakurai, T.; Tsuruma, Y.; Ikeda, S.; Saiki, K. *Appl. Phys. Lett.* **2007,** 90, (25), 251906.

25. Liu, Y.; Wu, H.; Cheng, H.-C.; Yang, S.; Zhu, E.; He, Q.; Ding, M.; Li, D.; Guo, J.; Weiss, N. O.; Huang, Y.; Duan, X. *Nano Lett.* **2015,** 15, (5), 3030-3034.

26. Das, S.; Chen, H.-Y.; Penumatcha, A. V.; Appenzeller, J. *Nano Lett.* **2013,** 13, (1), 100-105.

27. Chen, J.-R.; Odenthal, P. M.; Swartz, A. G.; Floyd, G. C.; Wen, H.; Luo, K. Y.; Kawakami, R. K. *Nano Lett.* **2013,** 13, (7), 3106-3110.

28. Popov, I.; Seifert, G.; Tománek, D. *Physical Review Letters* **2012,** 108, (15), 156802.

29. Withers, F.; Del Pozo-Zamudio, O.; Schwarz, S.; Dufferwiel, S.; Walker, P. M.; Godde, T.; Rooney, A. P.; Gholinia, A.; Woods, C. R.; Blake, P.; Haigh, S. J.; Watanabe, K.; Taniguchi, T.; Aleiner, I. L.; Geim, A. K.; Fal'ko, V. I.; Tartakovskii, A. I.; Novoselov, K. S. *Nano Lett.* **2015,** 15, (12), 8223-8228.

30. Britnell, L.; Gorbachev, R. V.; Geim, A. K.; Ponomarenko, L. A.; Mishchenko, A.; Greenaway, M. T.; Fromhold, T. M.; Novoselov, K. S.; Eaves, L. *Nat. Commun.* **2013,** 4, 1794.

31. Withers, F.; Del Pozo-Zamudio, O.; Mishchenko, A.; Rooney, A. P.; Gholinia, A.; Watanabe, K.; Taniguchi, T.; Haigh, S. J.; Geim, A. K.; Tartakovskii, A. I.; Novoselov, K. S. *Nature Mater.* **2015,** 14, (3), 301-306.
32. Schwierz, F. *Nature Nanotech.* **2010,** 5, (7), 487-496.

H. Figures and legends

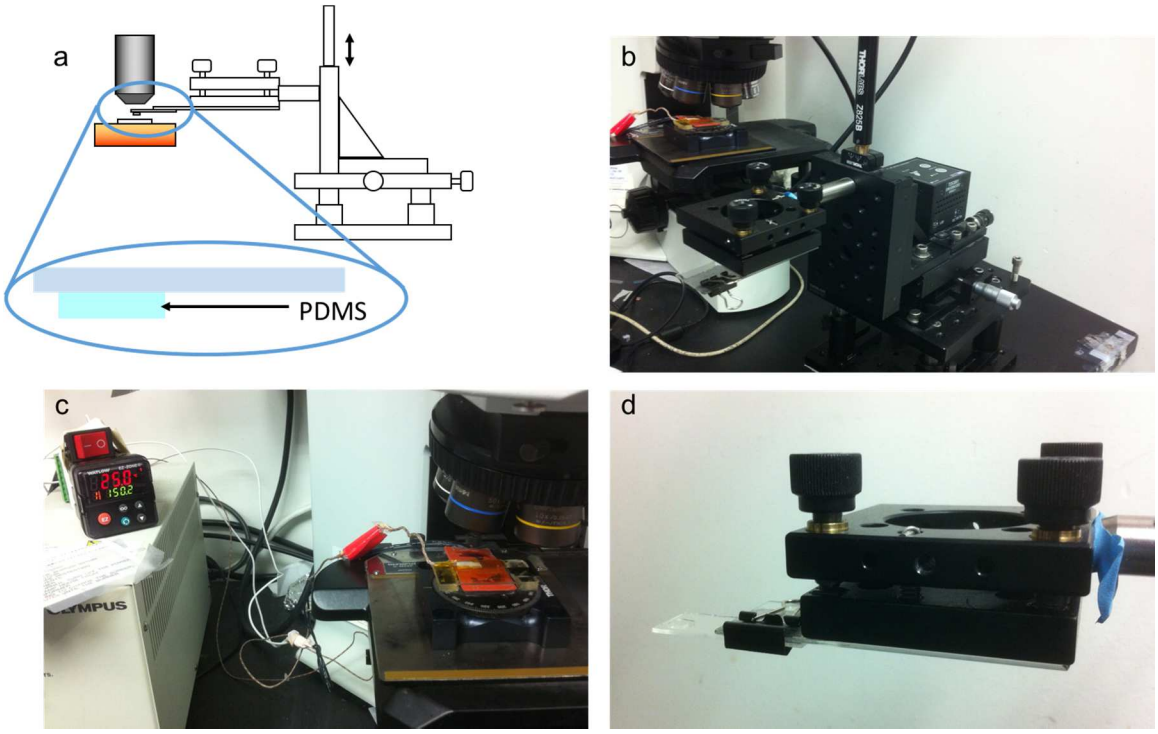

Figure 1-1. The homebuilt water-free dry transfer setup.

(a) The schematic illustration includes the micro-manipulator, the sample heating stage, objective lens (50X, long working distance) and the PDMS stamp attaching to a glass slide. (b) The perspective view of micro-manipulator. (c) The sample heating stage that assists the transfer process. (d) The glass slide holder attached to adjustable mirror mount, which is used for adjusting the alignment between sample and target.

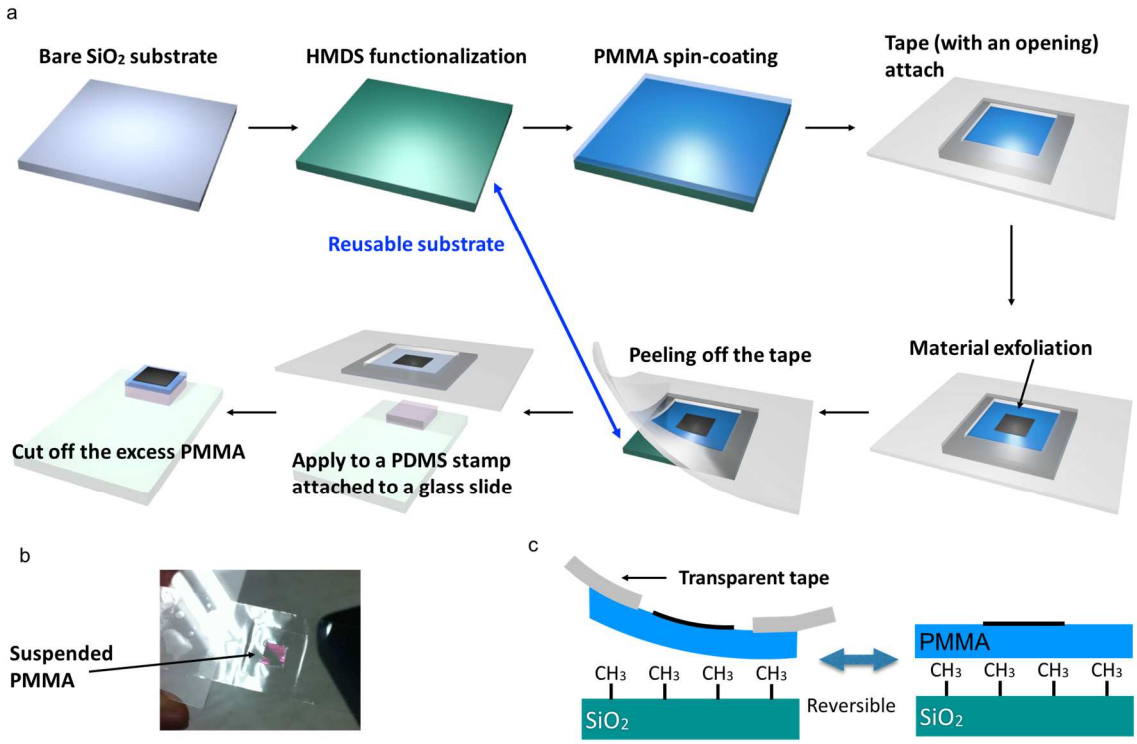

Figure 1-2. The water-free dry transfer approach.

(a) The bare SiO2 substrate is first cleaned with oxygen plasma. The following HMDS functionalization is performed by inserting the plasma cleaned substrate in the HMDS vapor chamber for 10 min at 120 °C. The PMMA layer is then spun onto the HMDS-treated substrate. A scotch tape with a small opening is attached to the substrate. The exposed area is now ready for material exfoliation. By peeling off the tape, the PMMA can be lifted off from the substrate and attach to the PDMS stamp. (b) The picture shows the lifted off PMMA (with exfoliated materials) (c) The schematic shows the cross-section view of HMDS assisted removal of PMMA.

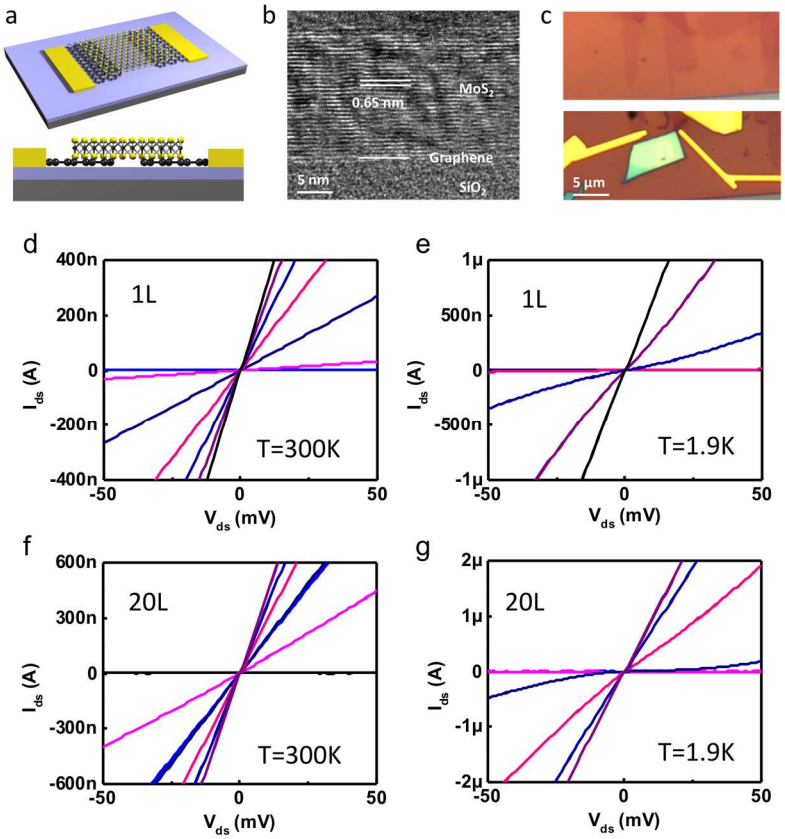

Figure 1-3. The schematic and output characteristics of graphene contact MoS_2 field-effect transistors (FETs).

(a) The schematic illustration of a bottom graphene contacted MoS_2 FET. (b) A cross-section TEM view of the MoS_2/graphene device. (c) The optical images of the exfoliated graphene electrodes (upper panel) and the MoS_2 device fabricated by transferring a MoS_2 flake onto graphene electrodes (lower panel). (d,e) The output characteristics of a monolayer MoS_2 FET at 300 K and 1.9 K, respectively (f,g) The output characteristics of a 20 layer MoS_2 FET at 300 K and 1.9 K, respectively. (Adapted from [25])

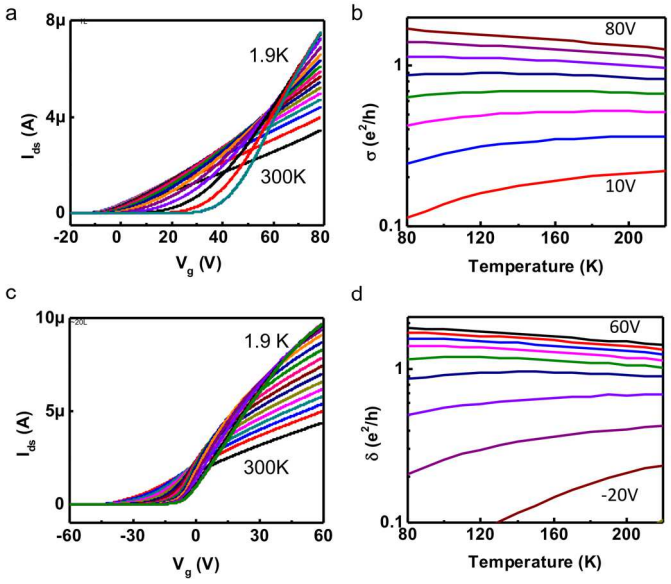

Figure 1-4. Transfer characteristics of MoS_2 FETs.

(a) The temperature dependent transfer curves of a monolayer MoS_2 FET. (b) The corresponding sheet conductivity extracted from (a) (V_g varies from 10 V to 80 V with a increment of 10 V). (c) The temperature dependent transfer curves of a multilayer MoS_2 FET. (d) The corresponding sheet conductivity extracted from (c) (V_g varies from -20 V to 60 V with a increment of 10 V). (Adapted from [25])

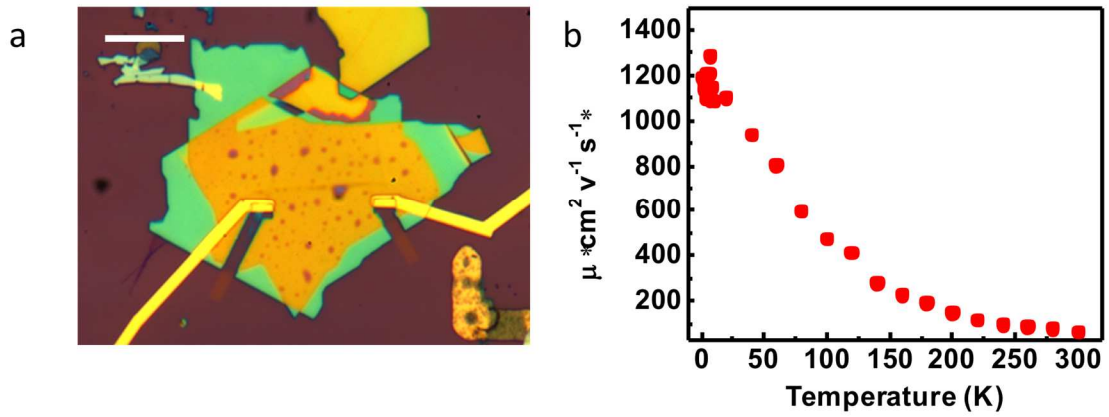

Figure 1-5. The long channel few layer MoS_2 FET encapsulated in top and bottom boron nitride with graphene contact electrodes.

(a) The optical image of the device. The white scale bar is 10 μm. (b) The carrier mobility estimated from two-terminal configuration versus temperature. The highest mobility is 1300 cm^2/V.s. (Adapted from [25])

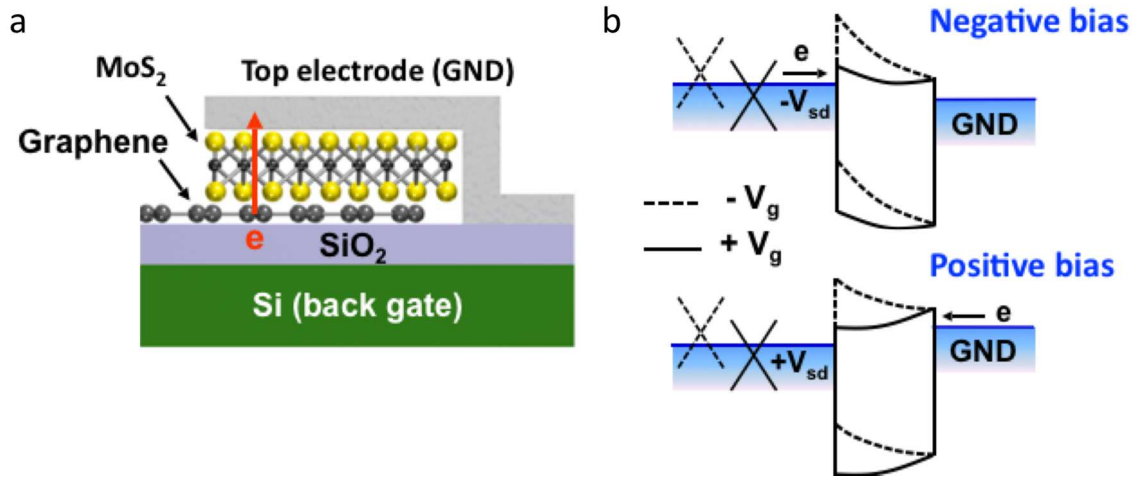

Figure 1-6. The schematic and band diagram of a graphene/MoS_2/metal vertical device.

(a) Schematic illustration of a vertical graphene/MoS_2/metal device. (b) The band diagram depicts the gate-tunable barrier height under negative (upper panel) and positive (lower panel) bias voltage. Under negative bias, the device current is dominated by injecting electrons from graphene to MoS_2, which can be largely modulated by the gate voltage. On the other hand, when bias is positive, the electron injection is now controlled by the metal/MoS_2 junction which can hardly be modulated by the gate field. (Adapted from [11])

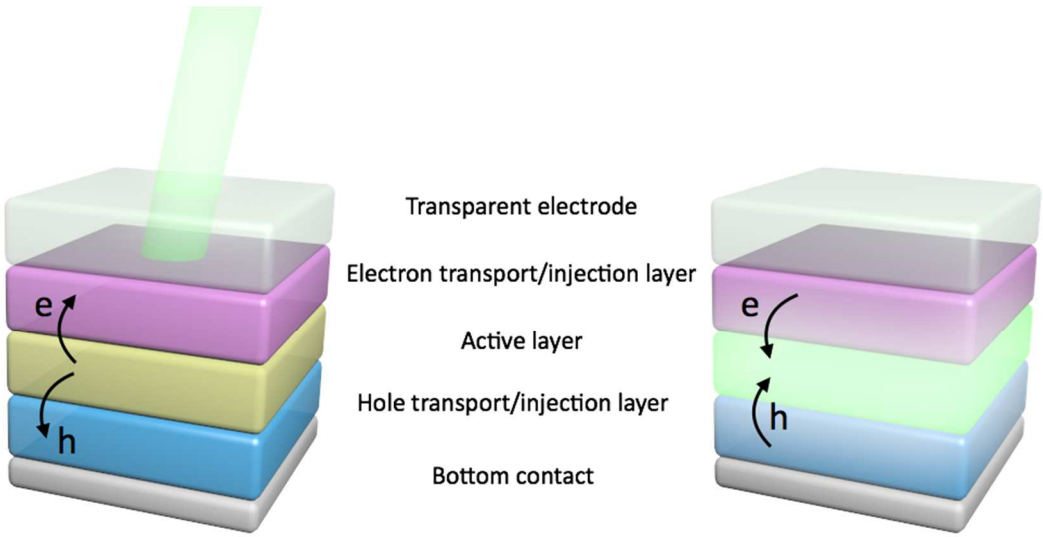

Figure 1-7. Schematic illustration of basic layered structures of optoelectronic devices.

The left panel is photodetectors and while the right on is light-emitting diodes.

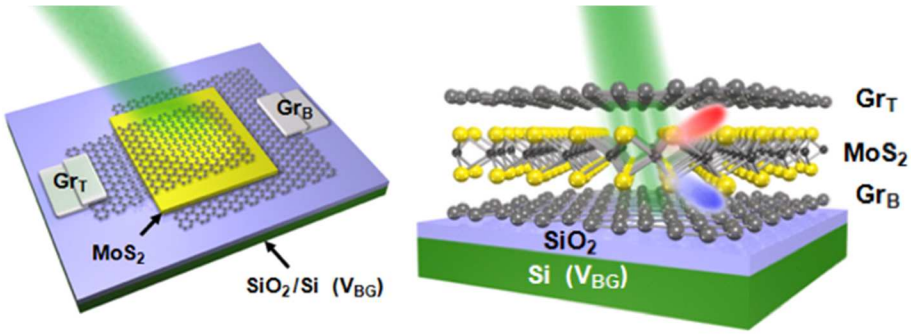

Figure 1-8. Schematic illustration of graphene/MoS_2/graphene photodetectors.

By varying the bottom gate field, the work function of bottom layer graphene (Gr_B) can be tuned to facilitate photo-carrier extraction. (Adapted from [12])

CHAPTER II: FROM TWO-DIMENSIONAL MATERIALS TO ORGANOMETAL HALIDE PEROVSKITE BASED ELECTRONIC DEVICES

A. Introduction

Recently, the newly emerged organometal halide perovskites has made a revolutionary breakthrough in solar cell research — the reported power conversion efficiency of perovskite-based cells is growing in an unprecedented rate over the past five years, achieving 20.1% from 3.8%.[1, 2] The record has now improved to 22.1%, which is much higher than 13.6% of amorphous silicon cell, and approaching 27.6% of crystalline silicon and 29.1% of GaAs single junction cell.[3] Such exceptional performance can be attributed to their strong optical absorption and micrometer-long carrier diffusion length.[4-7] Moreover, the band gap of these perovskites are direct and compositionally tunable, offering more possibilities in optoelectronic applications.[8]

In the very beginning, perovskites were used in dye-sensitized solar cell (DSSC). These DSSCs containing mesoporous n-type TiO_2, light-absorbing dye and redox-active electrolyte, in which perovskites are employed as light absorbers.[2] However, the perovskite absorbers dissolve in the electrolyte, degrading the cells and limiting the efficiency to 6.5%.[5] Later, an improved stability and higher efficiency up to 9.7% was reported, in which they replaced the liquid electrolyte with solid-state hole transporting layer.[9] Another important finding was reported in 2012, Snaith and his co-workers reported an efficiency improvement of 10.9% by replacing the mesoporous n-type TiO_2 with insulating Al_2O_3, demonstrating that these cells are no longer sensitized solar cells.[10] The Al_2O_3 only acts as a mesoporous scaffold, implying that perovskite itself can serve as a high efficient photoactive layer. Previous studies show that these perovskites can be even more versatile.

For example, optoelectronic devices based on perovskites, including photodetectors, light-emitting devices and lasers have been widely investigated.[11-18]

The organometal perovskites share a similar ABX_3 crystal structure with other inorganic perovskites (Figure 2-1). The larger A sites are occupied by organic molecule-based cations, while the smaller B sites are occupied by group 14 divalent cations (e.g., Pb, Sn). The corner-sharing octahedra BX_6 are formed by B metal cations and halide anions (Cl^-, Br^- and I^-) with B–X–B bonds (180° angle of bonds). In our studies, we mainly focus on the most popular organometal perovskites -- methylammonium lead iodide perovskites ($CH_3NH_3PbI_3$ or $MAPbI_3$)) which has been wide investigated in various applications, such as photovoltaics, light-emitting devices and lasers.[11-18] These $MAPbI_3$ are commonly synthesized by spin-coating technique. Specifically, PbI_2 solution is first spun on the growth substrate and following by CH_3NH_3I (MAI) solution. Alternatively, other lead halide based perovskites can also be obtained by exposing lead halides in the vapor or solution of MAI/alkylammonium halides that hold the structure of the perovskites. By selecting different organic molecules, the lead halide octahedra in perovskites can be further separated into layers with organic molecules as the spacers. Such layered organometal perovskites have the Ruddlesden–Popper crystal structure, which are described by this formula, $(R\text{-}NH_3)_2(MA)_{n-1}Pb_nI_{3n+1}$.[19] The $MAPbI_3$ is obtained as $n = \infty$. As n decreases from ∞ to 1, the thickness of each layer increases, resulting in increasing band gaps due to quantum confinement effect, which can offers more design capabilities for perovskite based optoelectronics.[20]

B. Conversion of layered lead iodide flakes

As we have discussed in the last section, organometal perovskites can be converted from metal halides, in particular, lead iodide is used for $MAPbI_3$ conversion.[21-23] During this conversion process, the crystal structure of layered lead halide undergoes a structural rearrangement as the organic cations are inserted into the interstice of corner sharing PbI_6 octahedra as shown in Figure 2-2. In our study, we mechanically exfoliate lead iodide into thin flakes. To obtain lead iodide crystal, we first dissolve 0.4 g in 100 mL hot water (100 °C). The solution is fully stirred at 100 °C and slowly cooled down to room temperature. Due to much lower solubility of lead iodide in water at room temperature. The precipitated crystal is growing during the cooling down process. After cooled down to room temperature, we pour the precipitated solution into a crystalized dish (see Figure 2-3a) and use pipette to draw clear solution out to reduce the quantity of liquid. These precipitated crystals are then dried further in oven (see Figure 2-3b). The crystal can be easily exfoliated from into thinner crystal using conventional "scotch tape" method, here we use Nitto tape to peel off the thick crystal (Figure 2-3c). Taking advantage of layered nature of lead iodide, we are able to thin down the crystal thickness to several nanometer or even down to monolayer. Figure 2-4 shows the lead iodide flakes exfoliated by tape method, a clear layered structure can be observed in AFM images. The thinnest part is around 0.8 nm which is close to previously suggested thickness of monolayer lead iodide.[24] However, the exfoliated lead iodide flakes are not stable in ambient condition due to the attack of moisture. To further converted these exfoliated lead iodide thin flakes into $MAPbI_3$, we employed a quartz furnace tube to perform vapor phase intercalation.[25] The experimental setup is shown in Figure 2-5, in which we place a sapphire boat with powder of MAI near the center of tube furnace, while a sample with exfoliated lead iodide thin flakes (on the

oxidized silicon substrate) is placed at the downstream.[23] By heating up to 130 °C, the MAI vapor carried by argon gas is brought to the sample sitting at the downstream. The reaction time could take around 1 to 3 hours to complete. Figure 2-6a, b shows the comparison before and after conversion process on the same flake. A obvious color contrast change is observed after the conversion process. In addition, the photoluminescence (PL) spectrum taken from the same spot before and after conversion is shown in Figure 2-6c. A very prominent PL peak at 760 nm is observed after the conversion process, which is a clear evidence indicated a successful conversion to $MAPbI_3$.[23] On the other hand, the PL from ultrathin PbI_2 is too weak to be detected in our measurement system.

C. Thickness dependent perovskite formation from layered lead iodides

Despite the fact that PbI_2 has relatively week PL signal that can hardly detected by our setup. We still observe PL signals from much thicker PbI_2. Figure 2-7 shows an optical image of a lead iodide flakes. We performed spot PL measurement on different spots of flakes with different thickness. The results clearly indicate the band gap of lead iodide blue shifts as the thickness of flakes decreases, which is due to quantum confinement effect. To further understand the conversion dynamics of perovskite, we changed the position of sample at downstream, we found that as the sample place toward the center, the perovskites cannot be fully converted, in contrast, if the sample is moved away from the center, the perovskites will be over-converted. This may be due to the temperature of sample during conversion process. The higher substrate temperature leads to the lower MAI vapor density, on the contrary, the lower substrate temperature can increase the density of MAI vapor, which in turn leads over-conversion within the same amount of reaction time. By controlling the position of sample, we examined a partially converted perovskites from a

several hundreds of nanometer thick lead iodide. As shown in Figure 2-8, both lead iodide and perovskite peaks can be observed, on the other hand, the color contrast of lead iodide flakes (before and after) does not show obvious change, suggesting PL can be a sensitive probe for the conversion of perovskites. In the case of over-converted perovskites, we found that the converted perovskite can no longer keep the shape of lead iodide, in fact, they tend to become discrete dots which still have very strong PL intensity. As shown in the optical images in Figure 2-9, after over-conversion process, the thicker part became larger particles, while the thinner part became smaller particles which can still keep a "shape" of the original lead iodide flakes. To further inspect the morphology of these over-converted perovskites, AFM images were obtained from the same lead iodide flakes before and after over-conversion (Figure 2-9). In Figure 2-9f, an unambiguous layer-dependent particle formation is shown, indicating that the conversion is taken place locally with the flake, thus resulting size-controllable nanoparticles formation. Such dispersion-free method for perovskite quantum dots formation could be further studied and applied to the design of solid-state high performance optoelectronics.

D. Lateral conversion of hybrid perovskites

As we have discussed in the previous section, the conversion of perovskite is an intercalation process of organic molecules into the lead iodide lattice. To understand how organic molecules interact with layered lead iodide, the surface of lead iodide was covered with graphene in order to block the entry of organic molecules from out of plane direction during conversion process. It is found that that the conversion process can still proceed laterally even without out of plane reaction. As shown in Figure 2-10a, an exfoliated

monolayer graphene was transferred onto a thin flake of lead iodide using our previously developed water-free dry-transfer method (see Chapter I). After dissolving the top PMMA layer in chloroform, the flake shows a color contrast change at the part that is not covered by graphene. We later found that this is due to partly dissolution of lead iodide by the residual solvent of PMMA. To characterize the lateral conversion of perovskites, the PL map (509 nm) was acquired near the edge of graphene, showing that the area protected by graphene has stronger PL intensity than the exposed area (Figure 2-10). After the 1-hour conversion process, the PL (509 nm) intensity for the converted region (under graphene) is significantly reduced, while the unconverted region exhibits stronger emission of PbI_2. On the other hand, the existence of $MAPbI_3$ can be evident by the emission peak at 760 nm. In Figure 2-10f, a moderate emission from $MAPbI_3$ was detected in the converted region (under graphene) where the PbI_2 signal is strongly reduced. This indicated that PbI_2 can be successfully converted to $MAPbI_3$, despite the fact that it was covered by graphene.

E. Laterally converted graphene/perovskite/graphene devices

In previous section, we have investigated the possibility to laterally convert the graphene covered lead iodide into perovskites. In order to further explore the electrical as well as the optoelectronic properties of perovskites, we fabricated the basic vertical electronic devices by using monolayer graphene as the top and bottom electrodes, which enables incident light to interact with the perovskites because of the transparency of graphene. To build a vertical graphene contact perovskite device, we build the devices by directly converting the graphene/lead iodide/graphene (GLG) devices into the graphene/perovskite/graphene (GPG) through aforementioned lateral conversion process.

Device fabrication

A layer of PMMA is first spun on a hexamethyldisilazane (HMDS) treated silicon substrate (see chapter I), followed by coating another layer of polypropylene carbonate (PPC). The PbI_2 typically with a thickness of 50~80 nm are exfoliated onto the PMMA/PPC polymer stack. Then the polymer stack is peeled off from HMDS treated silicon substrate and attached to a PDMS (polydimethylsiloxane) stamp with PbI_2 side up. The PDMS stamp with PbI_2 sitting on PMMA/PPC stack is positioned on a prepared monolayer graphene exfoliated on 290 nm SiO_2/Si substrate. Then PDMS and the PbI_2 are brought to contact with graphene. The polymer stack is then released from PDMS stamp by heating up the substrate to 120 °C. After transfer, the polymer stack is dissolved in chloroform for 10 min. Another graphene serving as top electrode is prepared on another PMMA coated silicon substrate, which is transferred immediately on the PbI_2/graphene stack after removal of PMMA. The electrodes are defined by e-beam lithography followed by metal evaporation (Cr/Au 20 nm/ 80 nm) and lift-off in chloroform for 10 min. The graphene/PbI_2/graphene stack was later converted into perovskite laterally using vapor phase reaction with methylammonium iodide vapor carried by argon gas flow.

Device characterization

The electrical measurements were carried out in commercial probe station (Lakeshore, TTP4). The power of illuminated while light source is 8.65 mW/cm^2 (at 633 nm). The electrical measurement was conducted with precision source/measure unit (Agilent, B2902A). The photoluminescence spectra were taken with a commercial confocal micro-Raman system (Horiba LABHR) excited by the Ar-ion laser (488 nm) with an excitation power ~3.8 μW. The PL map was conducted by collecting the spectra while

moving the stage within a specified area. The AFM images were taken from Bruker Dimension 5000 Icon scanning probe microscope.

Result and discussion

To probe the intrinsic optoelectronic properties of the vertical GLG device, we conducted the electrical measurement in vacuum under dark and light illumination. Figure 2-11 shows the optical image and the output characteristics of a typical GLG device. A significant increase in conductivity was observed under white light excitation (8.65 mW/cm^2). The output curve under light excitation shows a current saturation as sweeping at large bias voltage, which may be due to the limited density of states of lead iodide. To further convert the GLG device into GPG device, we first perform two-hour conversion. Similar to our previous results with lateral conversion, a discernible boundary was formed under graphene. The corresponding output characteristic of the partially converted GPG device shows a ~3 orders of magnitude increase in both dark current and light current, indicating that the perovskite part has dominated the vertical current transport due to its higher conductivity compared to lead iodide. With further conversion on the same device, the device can be laterally and completely converted into graphene/perovskite/graphene (GPG) device. As shown in Figure 2-12, the optical image shows the device after 15-hour conversion. The converted region is now spread throughout the entire overlapping area of the devices. However, we did not observe an obvious increase in device current as expected. This may be due to the increasing ion migration in the as-converted perovskite since the intercalated organic ions can move with enough defect density under strong electric field. To eliminate the impact of the defects as well as the ion migration in the as-converted device, we annealed the sample at 120 °C for 10 min to reduce the defects formed

during lateral conversion process. As shown in the Figure 2-12c, around two orders of magnitude increase in device current was observed, suggesting that GPG device can be directly derived from GLG device, along with nearly 4 orders of magnitude increase in conductivity.

F. Summary

In summary, we have demonstrated that the most studied organometal perovskites $MAPbI_3$ can be converted by intercalating MAI into exfoliated layered lead iodide. Taking advantage of the layered characteristic of lead iodide, we are able to explore the properties of atomically thin PbI_2 which can be further converted into perovskites. It was found that the over-conversion of perovskites leads to thickness dependent particle formation. That is, the size of over-converted perovskite nanoparticles (quantum dots) decreases with decreasing thickness of lead iodide, demonstrating that the conversion is taken place locally. Such thickness dependent quantum dots requires further studies on their optical properties and electrical properties, which may open up new opportunities in optoelectronic devices. By employing graphene as the reaction blocker, we have observed the lateral conversion of perovskites. The organic molecules can penetrate into the lattice of PbI_2 laterally to form the perovskite under the protection of graphene, which provides the insight of perovskite conversion dynamics and the possibility to integrate with graphene and other two-dimensional materials for the future high performance optoelectronic devices.

G. References

1. Yang, W. S.; Noh, J. H.; Jeon, N. J.; Kim, Y. C.; Ryu, S.; Seo, J.; Seok, S. I. *Science* **2015,** 348, (6240), 1234.
2. Kojima, A.; Teshima, K.; Shirai, Y.; Miyasaka, T. *J. Am. Chem. Soc.* **2009,** 131, (17), 6050-6051.
3. National Center for Photovoltaics at the National Renewable Energy Laboratory, Research cell efficiency records, http://www.nrel.gov/ncpv/ (accessed 23 Sep 2016).
4. Dong, Q.; Fang, Y.; Shao, Y.; Mulligan, P.; Qiu, J.; Cao, L.; Huang, J. *Science* **2015,** 347, (6225), 967.
5. Im, J.-H.; Lee, C.-R.; Lee, J.-W.; Park, S.-W.; Park, N.-G. *Nanoscale* **2011,** 3, (10), 4088-4093.
6. De Wolf, S.; Holovsky, J.; Moon, S.-J.; Löper, P.; Niesen, B.; Ledinsky, M.; Haug, F.-J.; Yum, J.-H.; Ballif, C. *J. Phys. Chem. Lett.* **2014,** 5, (6), 1035-1039.
7. Stranks, S. D.; Eperon, G. E.; Grancini, G.; Menelaou, C.; Alcocer, M. J. P.; Leijtens, T.; Herz, L. M.; Petrozza, A.; Snaith, H. J. *Science* **2013,** 342, (6156), 341.
8. Jeon, N. J.; Noh, J. H.; Yang, W. S.; Kim, Y. C.; Ryu, S.; Seo, J.; Seok, S. I. *Nature* **2015,** 517, (7535), 476-480.
9. Kim, H.-S.; Lee, C.-R.; Im, J.-H.; Lee, K.-B.; Moehl, T.; Marchioro, A.; Moon, S.-J.; Humphry-Baker, R.; Yum, J.-H.; Moser, J. E.; Grätzel, M.; Park, N.-G. *Sci. Rep.* **2012,** 2, 591.
10. Lee, M. M.; Teuscher, J.; Miyasaka, T.; Murakami, T. N.; Snaith, H. J. *Science* **2012,** 338, (6107), 643.

11. Stranks, S. D.; Snaith, H. J. *Nature Nanotech.* **2015,** 10, (5), 391-402.

12. Dou, L.; Yang, Y.; You, J.; Hong, Z.; Chang, W.-H.; Li, G.; Yang, Y. *Nat. Commun.* **2014,** 5, 5404.

13. Lee, Y.; Kwon, J.; Hwang, E.; Ra, C.-H.; Yoo, W. J.; Ahn, J.-H.; Park, J. H.; Cho, J. H. *Adv. Mater.* **2015,** 27, (1), 41-46.

14. Tan, Z.-K.; Moghaddam, R. S.; Lai, M. L.; Docampo, P.; Higler, R.; Deschler, F.; Price, M.; Sadhanala, A.; Pazos, L. M.; Credgington, D.; Hanusch, F.; Bein, T.; Snaith, H. J.; Friend, R. H. *Nature Nanotech.* **2014,** 9, (9), 687-692.

15. Zhu, H.; Fu, Y.; Meng, F.; Wu, X.; Gong, Z.; Ding, Q.; Gustafsson, M. V.; Trinh, M. T.; Jin, S.; Zhu, X. Y. *Nature Mater.* **2015,** 14, (6), 636-642.

16. Chin, X. Y.; Cortecchia, D.; Yin, J.; Bruno, A.; Soci, C. *Nat. Commun.* **2015,** 6, 7383.

17. Cho, H.; Jeong, S.-H.; Park, M.-H.; Kim, Y.-H.; Wolf, C.; Lee, C.-L.; Heo, J. H.; Sadhanala, A.; Myoung, N.; Yoo, S.; Im, S. H.; Friend, R. H.; Lee, T.-W. *Science* **2015,** 350, (6265), 1222.

18. Veldhuis, S. A.; Boix, P. P.; Yantara, N.; Li, M.; Sum, T. C.; Mathews, N.; Mhaisalkar, S. G. *Adv. Mater.* **2016,** 28, (32), 6804-6834.

19. Tsai, H.; Nie, W.; Blancon, J.-C.; Stoumpos, C. C.; Asadpour, R.; Harutyunyan, B.; Neukirch, A. J.; Verduzco, R.; Crochet, J. J.; Tretiak, S.; Pedesseau, L.; Even, J.; Alam, M. A.; Gupta, G.; Lou, J.; Ajayan, P. M.; Bedzyk, M. J.; Kanatzidis, M. G.; Mohite, A. D. *Nature* **2016,** 536, (7616), 312-316.

20. Stoumpos, C. C.; Cao, D. H.; Clark, D. J.; Young, J.; Rondinelli, J. M.; Jang, J. I.; Hupp, J. T.; Kanatzidis, M. G. *Chem. Mater.* **2016,** 28, (8), 2852-2867.

21. Chen, Q.; Zhou, H.; Hong, Z.; Luo, S.; Duan, H.-S.; Wang, H.-H.; Liu, Y.; Li, G.; Yang, Y. *J. Am. Chem. Soc.* **2014,** 136, (2), 622-625.
22. Ha, S. T.; Liu, X.; Zhang, Q.; Giovanni, D.; Sum, T. C.; Xiong, Q. *Adv. Opt. Mater.* **2014,** 2, (9), 838-844.
23. Wang, G.; Li, D.; Cheng, H.-C.; Li, Y.; Chen, C.-Y.; Yin, A.; Zhao, Z.; Lin, Z.; Wu, H.; He, Q.; Ding, M.; Liu, Y.; Huang, Y.; Duan, X. *Sci. Adv.* **2015,** 1, (9).
24. Sandroff, C. J.; Kelty, S. P.; Hwang, D. M. *J. Chem. Phys.* **1986,** 85, (9), 5337-5340.
25. Cheng, H.-C.; Wang, G.; Li, D.; He, Q.; Yin, A.; Liu, Y.; Wu, H.; Ding, M.; Huang, Y.; Duan, X. *Nano Lett.* **2016,** 16, (1), 367-373.

H. Figures and legends

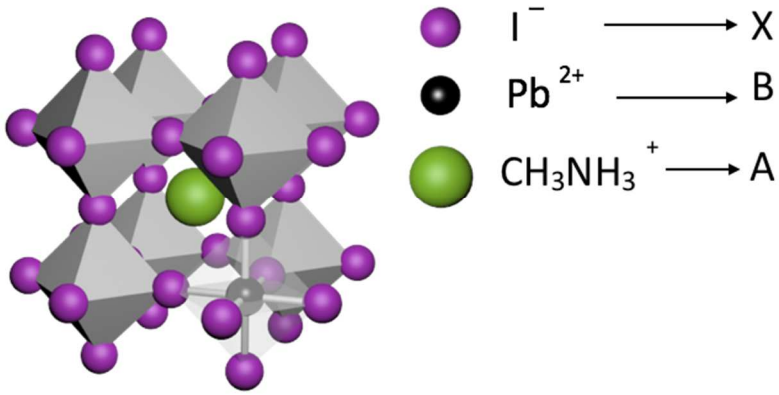

Figure 2-1. The crystal structure of $MAPbI_3$ ($CH_3NH_3PbI_3$).

The larger A sites are occupied by organic molecule-based cations, while the smaller B sites are occupied by group 14 divalent cations (e.g., Pb, Sn). The corner-sharing octahedra BX_6 are formed by B metal cations and halide anions (Cl^-, Br^- and I^-) with B–X–B bonds (180° angle of bonds).

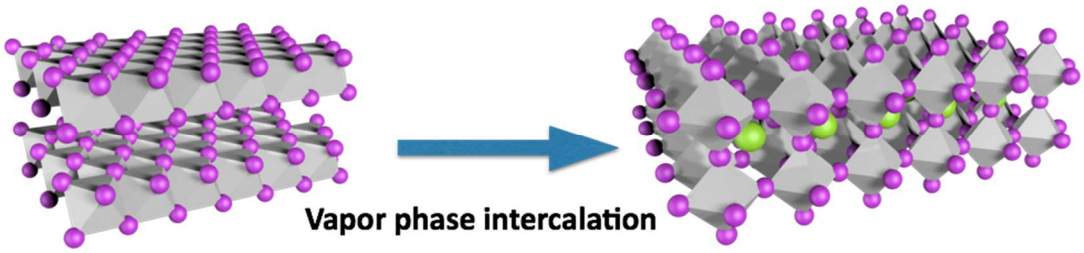

Figure 2-2. The vapor phase conversion from PbI_2 to $MAPbI_3$.

During this conversion process, the crystal structure of layered lead halide undergoes a structural rearrangement as the organic cations are inserted into the interstice of corner sharing PbI_6 octahedra. (Adapted from [25])

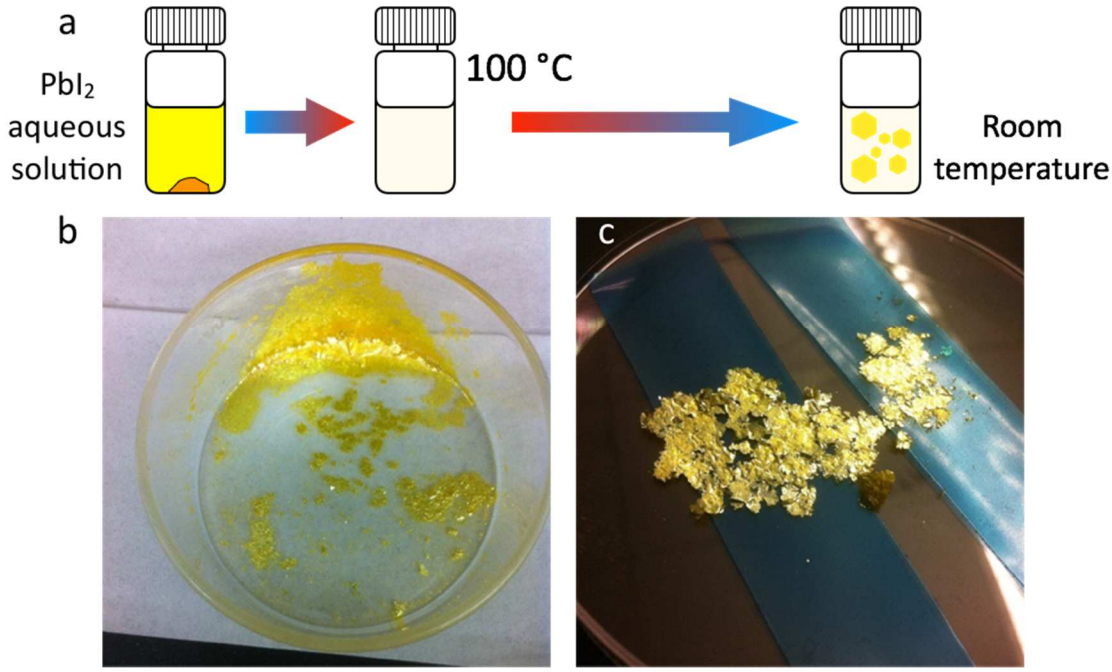

Figure 2-3. The formation of PbI_2 crystals for exfoliation.

(a) 0.4 g PbI_2 is first dissolved in 100 mL hot water (100 °C). The solution is fully stirred at 100 °C and slowly cooled down to room temperature. Due to much lower solubility of lead iodide in water at room temperature. The precipitated crystal is growing into large flakes during the cooling down process. (b) After cooled down to room temperature, the precipitated solution is poured into a crystalized dish and dried in oven. (c) The dried crystal can be picked up by the tape. (Adapted from [25])

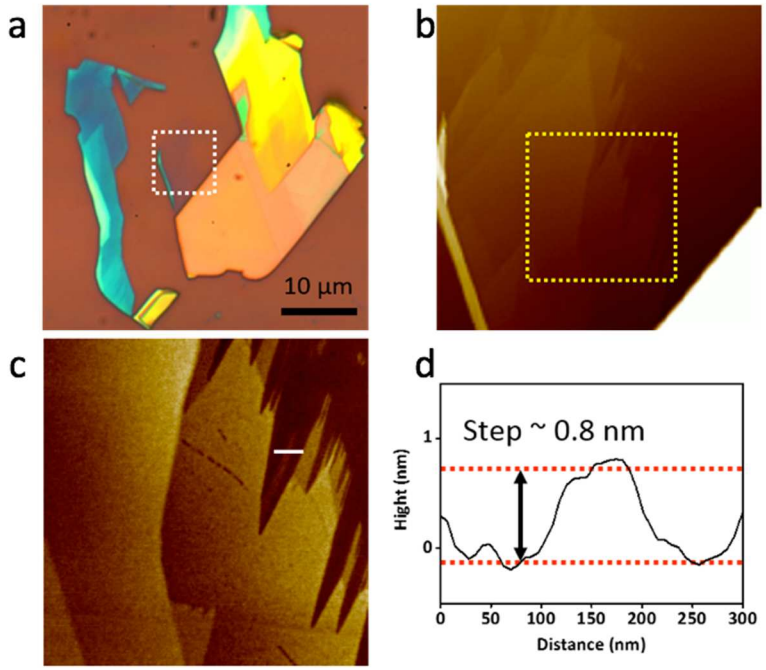

Figure 2-4. The optical and AFM images of the exfoliated PbI_2.

(a) The optical image of an exfoliated PbI_2 thin flake. (b) The AFM image of the area framed in white dashed window. (c) The AFM image of a zoom-in scan in (b). (d) The step profile of the thinnest flake in (c) marked by a white solid line. The step is 0.8 nm which is close to previously reported thickness of monolayer. (Adapted from [25])

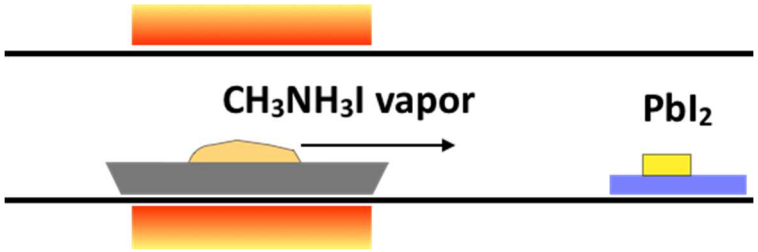

Figure 2-5. The furnace used for $MAPbI_3$ conversion from lead iodide.

A quartz furnace tube is employed to perform vapor phase intercalation. A sapphire boat with powder of MAI is placed near the center of furnace tube. An exfoliated lead iodide thin flake (on the oxidized silicon substrate) is placed at the downstream. By heating up to 130 °C, the MAI vapor carried by argon gas is brought to react with the lead iodide sample and form $MAPbI_3$.

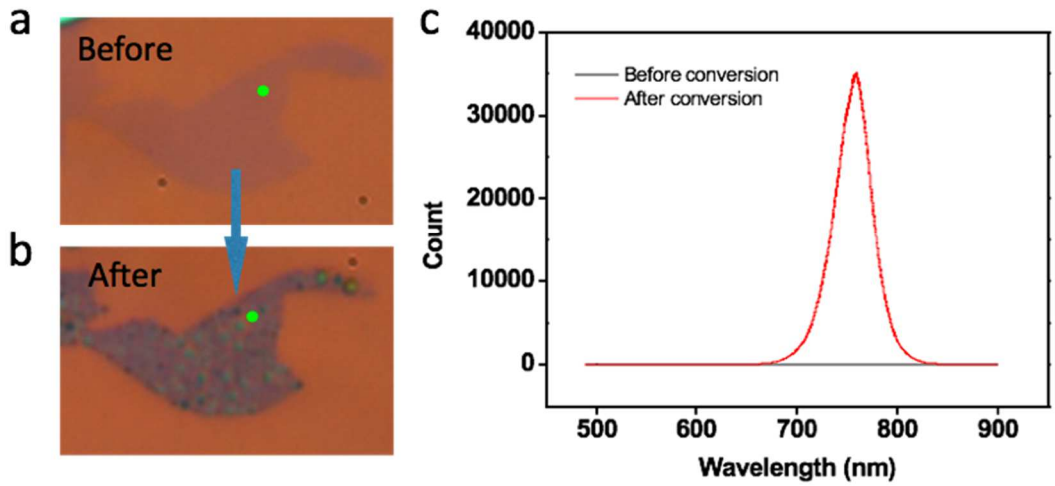

Figure 2-6. The optical image and PL spectra obtained from a thin PbI_2 before and after conversion process.

(a) The optical image of a thin PbI_2 flake on 290 nm SiO_2/Si. (b) The optical image of the PbI_2 flake shown in (a) was taken after perovskite conversion process. (c) The comparison of the PL spectra taken from the green spots in (a) and (b).

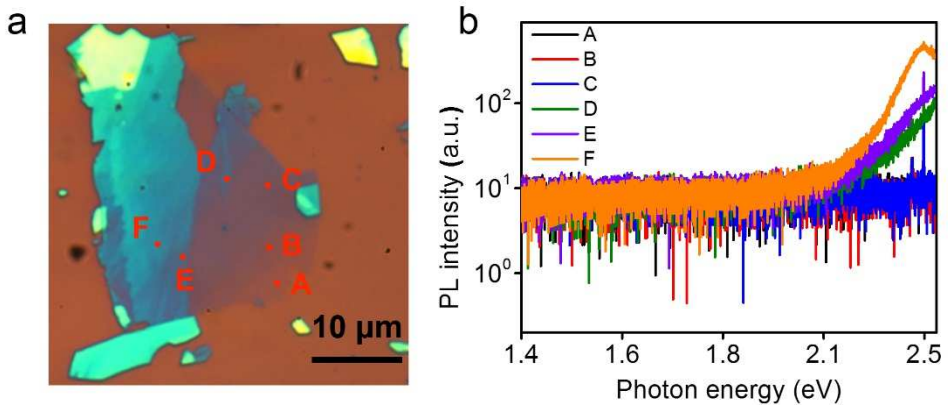

Figure 2-7. Photoluminescence spectra of a few layer PbI_2.

(a) The optical image of a few layer PbI_2. (b) The PL spectra taken from the corresponding spots in (a). For ultrathin PbI_2, the PL peaks are around 2.5 eV. As the thickness of PbI_2 decreases, the peaks blue shift and fall below the detection limit of the detectors.

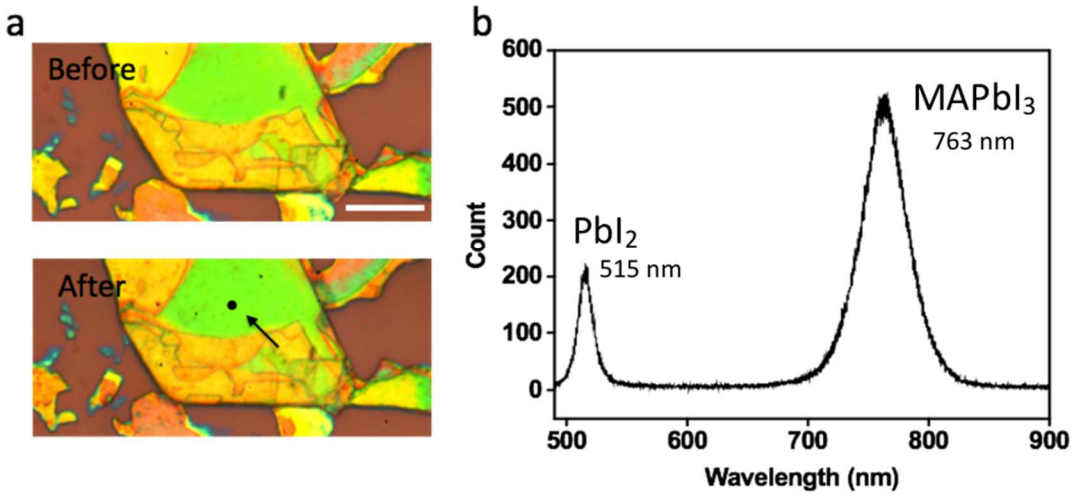

Figure 2-8. Optical image and PL spectrum of a partially converted PbI_2 flake.

(a) The optical image of a thick PbI_2 flake before (upper panel) and after (lower panel) conversion. (b) The PL of spectrum taken from a partially converted PbI_2 (indicated by a black solid spot). Both PbI_2 (515 nm) and perovskite (763 nm) peaks can be observed.

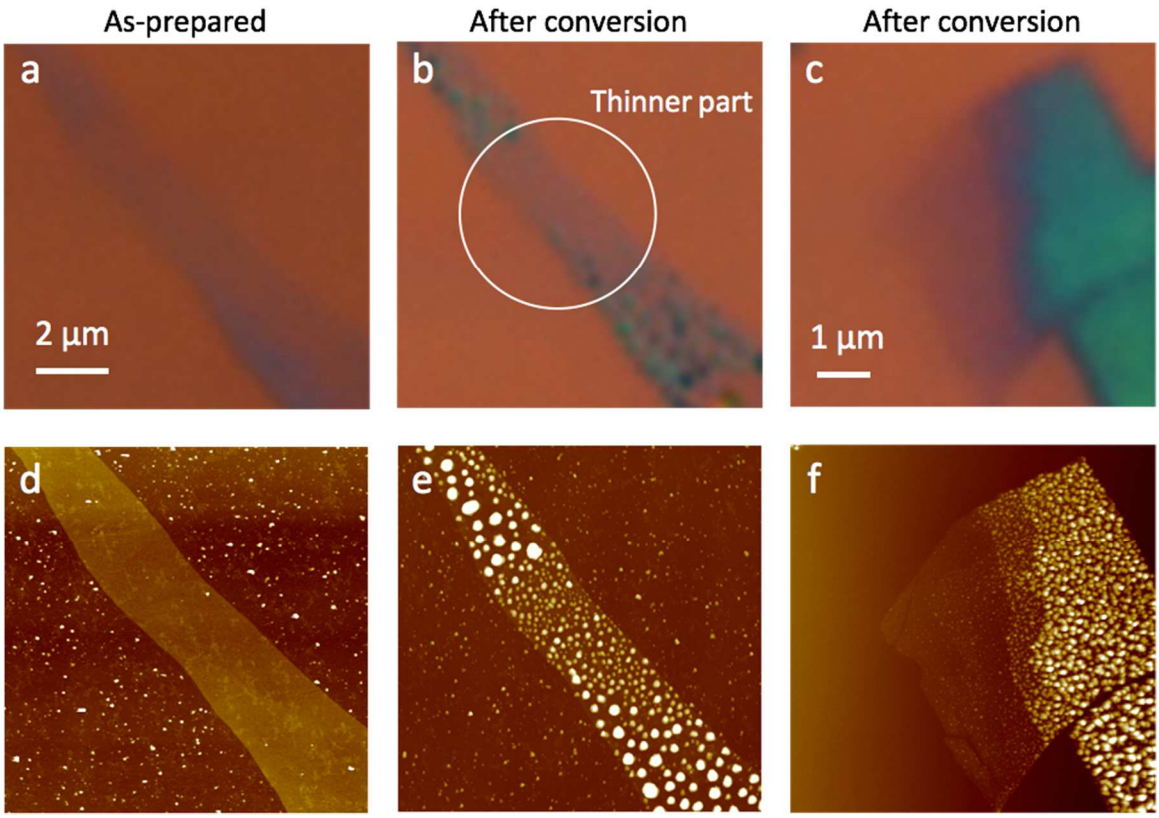

Figure 2-9. Optical and AFM images of over-converted perovskite.

(a,b) The optical images of a PbI_2 thin fake before and after over-conversion process. The white scale bar is 2 µm. (c) The optical image of an over-converted perovskites with different initial thickness. (d,e) The AFM images (on the same scale) of the samples at the corresponding condition in (a) and (b), respectively. (f) The AFM image of (c). An obvious thickness dependent perovskite nanoparticles formation.

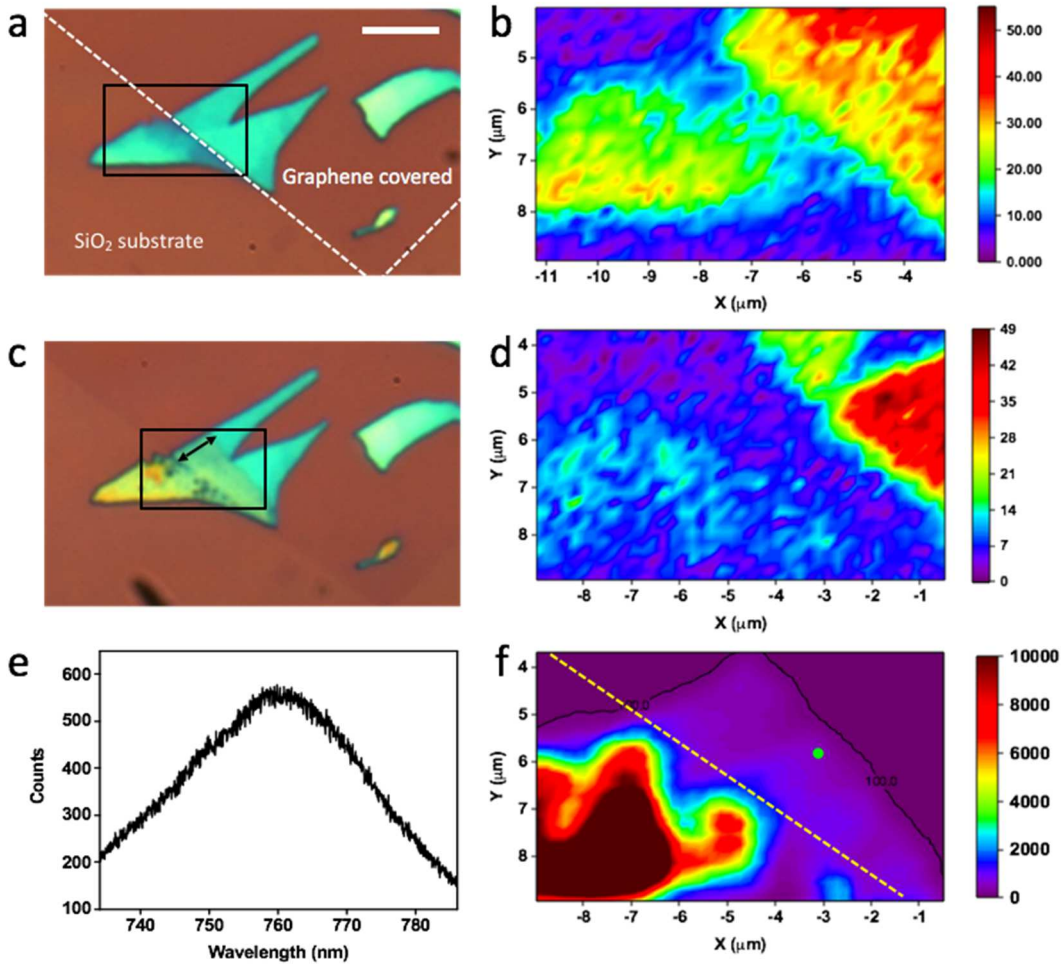

Figure 2-10. The characterization of laterally converted perovskite.

(a) The optical image of a PbI_2 flake which is partially covered by graphene. The white dashed line shows the edge of graphene, while the white scale bar is 5 μm. (b) The PL map (center at 509 nm) of the area enclosed by a black frame in (a). The PL signals indicate the emission from PbI_2. (c) The optical image was taken after 1 hr conversion from the same flake shown in (a). The black arrow indicate the lateral conversion depth is up to 2.6 μm from the edge of graphene. (d) The PL map (centered at 509 nm) shows the remaining signals behind the border of conversion. It is noted that the signals of PbI_2 is completely eliminated in the converted region. (e) The PL spectrum taken at the green spot shown in (f). (f) The PL map (centered at 760 nm) was taken from the same area as (d). The yellow dashed line marks the edge of graphene.

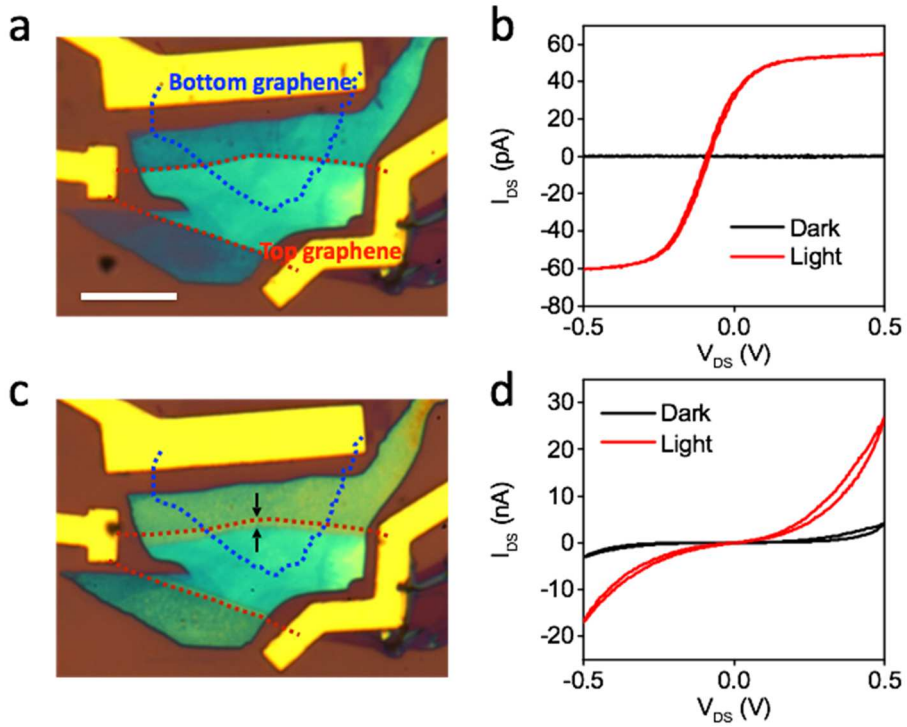

Figure 2-11. The optical images and out characteristics of a GLG device before and after partial conversion.

(a) The optical image of the as-fabricated GLG device. The blue dashed line shows the edge of bottom graphene, while the red dashed line indicates the edge of top graphene. The white scale bar is 10 μm. (b) The output characteristics of a GLG device measured under dark and illuminated condition. (c) The optical image of the device shown in (a) after partial conversion (2-hour conversion). The black arrows indicate the converted depth which is ~1 μm. (d) The output characteristics of the device shown in (c) measured under dark and illuminated condition. The device current shows a 3 orders of magnitude increase after 2-hour conversion.

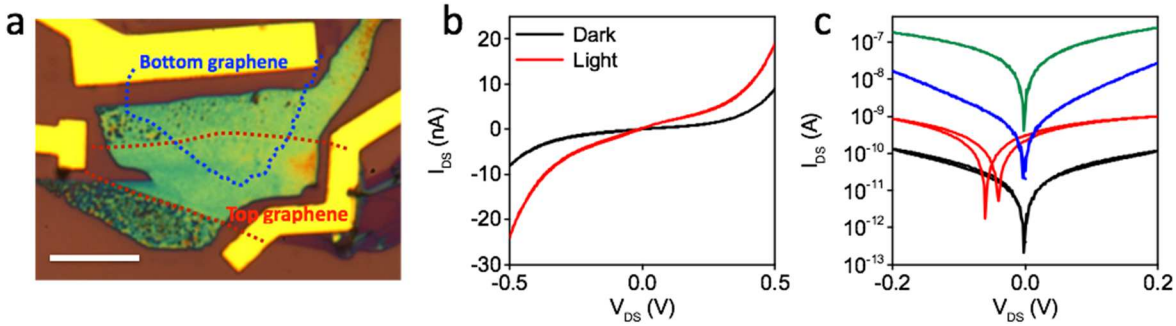

Figure 2-12. The optical images and out characteristics of a GLG device after full conversion.

(a) The optical image of a fully converted GLG device (15 hr conversion). (b) The output characteristics of the device shown in (a) by measuring under dark and illuminated condition. (c) The logarithmic of the output characteristics of the device shown in (a). The black and blue curves were measured under dark condition before and after thermal annealing process, respectively. The red and green curves were measured under illuminated condition before and after thermal annealing process, respectively. It is noted that the device current shows a 2 orders of magnitude increase after thermal annealing.

CHAPTER III: VAN DER WAALS HETEROJUNCTION DEVICES BASED ON ORGANOHALIDE PEROVSKITES AND TWO-DIMENSIONAL MATERIALS

A. Introduction

In this chapter, we mainly focus on the heterojunction devices based on organohalide perovskites and two-dimensional materials.[1] The recently discovered organic-inorganic hybrid perovskites (*e.g.*, $CH_3NH_3PbI_3$) have been demonstrated to be an attractive material for solution-processed solar cell[2-14] with a record high power conversion efficiency (PCE) of ~20.1%.[11] Such high PCE have been generally attributed to their strong light absorption[15] and long free carrier diffusion length.[4, 9, 10, 16-18] In addition to solar cell, the perovskites have also been explored for several applications, such as light-emitting diodes,[19, 20] lasers[21, 22] and photodetectors,[23-26] which have rendered them promising candidates in optoelectronic applications.

However, the solubility of $CH_3NH_3PbI_3$ in many common solvents including water, acetone and alcohol, and their instability in ambient condition have impeded their development in conventional device fabrication, and the studies to date have largely been limited to spin-coated perovskite thin films.[17, 20, 26] To fully explore their electronic and optoelectronic properties, it is important to integrate the perovskite materials into different device structures. Here we propose a new approach for the fabrication of complex perovskite devices, and demonstrate a new type of vertical photoconductive and photovoltaic perovskite devices with graphene as electrodes through a layer-by-layer van der Waals assembly process.[27-31] Taking advantage of the layered characteristics of lead iodide (PbI_2),[32-34] as we discussed in Chapter II, we are able to exfoliate PbI_2 crystal (Figure 2-3) into thin flakes (Figure 2-4) that can then be converted into $CH_3NH_3PbI_3$ under

methylammonium iodide (MAI) vapor phase reaction.[3, 34] As we have shown in Chapter II, we are able to control the conversion process by change the position of sample. Figure 3-1a, b shows the comparison of mechanically-exfoliated PbI_2 flakes before and after the full conversion process. With the intercalation of MAI in PbI_2, the averaged flake thickness increased around 1.9 times from 22.7 nm to 43.2 nm (Figure 3-1c), which is comparable to previous report on synthetic nanoplatelets.[35] Such transformation accompanied with increased thickness can be attributed to the volume expansion results from organic molecule intercalation (Figure 3-1d). Moreover, Figure 3-1e shows the photoluminescence (PL) spectrum taken from the same spot before and after conversion. The PL emission from ultrathin PbI_2 (~2 nm) flake is too weak to be detected in our measurement (Figure 2-7). On the other hand, a prominent single PL peak around ~1.63 eV appeared after conversion process, which indicates a successful conversion from PbI_2 to $CH_3NH_3PbI_3$.[34]

B. Methods

Device fabrication

Unlike the fabrication process described in Chapter II, we investigated the properties of graphene/perovskite/graphene (GPG) devices by transferring top graphene immediately after the conversion process. The carrier PMMA that we used for top graphene transfer can serve as the resist for e-beam lithography. The device is then prepared after a vacuum metallization (Cr/Au: 20 nm/80 nm) and lift-off process in chloroform. For BN-covered GPG device, the carrier PMMA is dissolved in chloroform after top-graphene transfer. Subsequently, another separately prepared boron nitride (BN) is used to cover the entire area of perovskite. Sometimes the graphene electrodes are fully covered by BN. To

make electrical contacts with BN covered graphene, we create edge contacts by etching the BN with fluoroform/O_2 (35/5 sccm) plasma for 1 min. The BN etching rate is faster than graphene, so we can always make good electrical contacts with graphene. For graphene/WSe_2/perovskite/graphene (GWPG) device, the WSe_2 (~50 nm) flakes are first transferred onto exfoliated monolayer graphene using PMMA/PPC stack. After dissolve polymer stack in chloroform, the WSe_2/graphene stack is now ready for PbI_2 transfer. The following steps are same as those described above.

Device characterization.

The electrical and low temperature measurements were both carried out in commercial probe station (Lakeshore, TTP4) equipped with a 532 nm laser (Coherent, 532-100). The electrical measurement was conducted with precision source/measure unit (Agilent, B2902A). The photoluminescence spectra were taken with a commercial confocal micro-Raman system (Horiba LABHR) excited by the Ar-ion laser (488 nm) with an excitation power ~3.8 μW. The photocurrent map was conducted in the same system by monitoring the current under the irradiation of focused laser (488 nm, < 300 nW) while moving the stage within a specified area. The AFM images were taken from Bruker Dimension 5000 Icon scanning probe microscope.

C. Vertical graphene/perovskite/graphene photoconductors

In order to understand the basic photoconductive properties of $CH_3NH_3PbI_3$, similar to the GLG device we previously studied in Chapter II. we have first created a graphene/perovskite/graphene (GPG) heterostructure device, in which graphene is used as both the top- and bottom-electrodes to sandwich the perovskite in the middle. Instead of

using the perovskite as the sensitizer[24] and measuring the conductivity change in graphene, we measured the current transport from the top- to bottom-graphene directly through the perovskite channel. Since both PbI_2 and perovskite are quite sensitive to the moisture in ambient condition, and soluble in common solvents that are usually used in fabrication process. We adopted a particular dry-process for creating designed heterostructures as described in Figure 3-2 and Methods. Figure 3-3 shows schematic illustration and an optical image of an as-fabricated GPG device. Electrical characterization was conducted in vacuum at room temperature. Figure 3-3b shows the current-voltage (I_{DS}-V_{DS}) characteristics measured under 532 nm laser with an equivalent power ~1.52 nW on the device area. By applying a constant bias voltage, the device worked as a photoconductor, the photocurrent $I_{ph} = (I_{illuminated} - I_{dark})$ increased with bias voltage as a consequence of the reduction of the carrier transit time. The photocurrent at bias 1 V is ~1.45 μA, which yields a photoresponsivity ~950 A/W and a photoconductive gain ~2200. However, during the time-domain measurement, the current drop quickly before reaching a stable state under a constant bias, which could be attributed to the ion movement in perovskite material driven by the electric field.[17, 20] Figure 3-3c shows the photocurrent response versus time after the current reaches a stable state. The photocurrent rise time is ~22 ms and the fall time is ~37 ms, which is reasonable for a high gain photoconductor. In order to spatially characterize the photocurrent contribution, we performed the spatially-resolved photocurrent map under focused laser beam (488 nm) in air (Figure 3-3d). The photocurrent map results show that the photocurrent is uniformly contributed from the graphene/perovskite/graphene overlapping area, indicating that the majority of photo-induced carriers travel in vertical direction.

D. Gate tunable vertical graphene/perovskite/graphene devices

Despite the protection by the top-graphene, the GPG devices still suffer from the attack of moisture during the measurement in air. To further improve device stability, we have transferred another boron nitride (BN) layer as an ultrathin protection layer[36] for the GPG stack. The protection by BN can also allow us using subsequent lithography process for the fabrication of GPG device. Since the top- and bottom-graphene may be covered by the BN, we have used edge metal contacts[27, 28] for both the top- and bottom-graphene electrodes (see Methods). Figure 3-4a shows the schematic illustration and optical image of BN-covered GPG device. Our study has proved that BN-protected devices show no considerable degradation in terms of photocurrent characteristics after 210 days from the first measurement (see Figure 3-5), demonstrating BN can serve as an effective protection for organohalide perovskite to significantly extend the lifetime of GPG device.

To explore semiconducting characteristics of perovskite, we measured the device current under different back-gate voltage. However, there is no obvious gate-modulation observed in our device at room temperature, which could be attributed to the gate-induced ion movement in $CH_3NH_3PbI_3$ compensating/screening the electric field from the back gate.[20] To minimize the effect of ion movement, we have conducted the measurement at 77 K. The I_{DS}-V_{DS} characteristics under dark show asymmetric response to the gate voltage (Figure 3-4b), which can also be identified in the transfer curves (Figure 3-4c). It is evident that the charge transport across the vertical stack increases with increasing negative gate voltage, suggesting a p-type hole transport behavior. Overall, there is considerable gate response when a negative bias is applied to the top-graphene electrode, while there is little

gate-modulation when the top-graphene electrode is positively biased. The transfer curves obtained in the dark show that the current on/off ratio is only about ~5 when the top-graphene electrode is positively biased (Figure 3-4c, red curve), and can reach up to ~500 while the top-graphene electrode is negatively biased (Figure 3-4c, black curve). The reasons for such asymmetric effect can be explained by the gate-modulation to the graphene work function and the Schottky barrier for hole-injection at bottom-graphene/perovskite interface. With negative bias applied to the top-graphene electrode, the holes are injected from bottom-graphene to perovskite and thus the bottom-graphene/perovskite barrier dominates the charge transport. In this case, a negative (positive) gate voltage elevates (reduces) the graphene work function and decreases (increases) the Schottky barrier for hole injection from the bottom-graphene to the perovskite, and thus enhancing (suppressing) the current across the vertical stack (depicted in Figure 3-4c inset). On the other hand, with a positive bias applied to the top-graphene, the holes are injected from top-graphene to the perovskite, where the barrier is only weakly modulated by the back-gate bias, and therefore we expect much smaller gate-modulation of the current transport. These analyses also further confirm that the holes are the dominated carrier in our GPG devices.

We have also investigated the photovoltaic effect in our GPG device. The I_{DS}-V_{DS} curves are measured at varying gate voltages under laser illumination (Figure 3-4d), and plotted in the logarithmic scale to examine the open-circuit voltage (V_{OC}). Importantly, as the gate voltage is increased from -60 V to 60 V, we observed a consistent shift of V_{OC} from a negative value to a positive value (Figure 3-4e). To exclude the possibility of device instability or time-dependent V_{OC} shift, we performed the same measurement with reverse

gate voltage sequence from 60 V to -60 V (Fig. 3-6a). Our studies show that V_{OC} shift is consistent with the applied gate bias rather than sequence in the measurement, indicating the shift is indeed resulted from the gate-modulation. Such gate-modulation effect can be attributed to the asymmetric tuning of top- and bottom-graphene work function, which induced a built-in electric field across the entire GPG structure. Basically, an applied back-gate voltage can electrostatically dope bottom-graphene and therefore modify its work function, and thus creating a work-function difference between top- and bottom-graphene, which resulted in a built-in electrical field that can drive the separation and transport of the photogenerated electrons and holes in opposite direction to produce a non-zero photogenerated, short-circuit current (I_{SC}) at zero-bias condition. As depicted in Figure 3-4e inset, when $V_G < 0$ (> 0), an additional negative (positive) bias to top-graphene is needed to compensate the built-in field leading to negative (positive) V_{OC}. In the context of GPG symmetric vertical structure, the V_{OC} and its gate-tunability are considerably smaller than other system such as graphene/MoS_2/graphene,[37] which may be attributed to its distinct ion movement effect under applied gate-voltage. Considering the case when the negative (positive) gate voltage is applied (Figure 3-4e), the positively (negatively)-charged ions in perovskite tend to accumulate at the interface between bottom-graphene and perovskite, which counters the gate-field induced work function modulation in bottom-graphene and results in less built-in field and smaller I_{SC} in this GPG device.

E. Tunable p-n junction in vertical graphene/perovskite/WSe_2/graphene devices

To further increase the built-in potential across the GPG device and explore more tunability with gate voltage, we have inserted an extra WSe_2 layer between bottom-

graphene and perovskite to create a graphene/WSe_2/perovskite/graphene (GWPG) device (Figure 3-7a). By applying bias to the top-graphene with bottom-graphene grounded, we have investigated the transfer characteristic of this GWPG vertical device as shown in Figure 3-7b. We found the on/off ratio of negatively-biased device has been greatly improved to ~10^6 compared to that in the previous symmetric GPG device (~500) measured in the dark. Such distinct gate-tuning effect can be considered as the combination of the gate-modulation of the Schottky barrier height at bottom-graphene/WSe_2 (GW) interface and the modulation of the WSe_2/perovskite (WP) heterojunction interface. To elucidate the gate-modulation effect, we are now focusing on the I_{DS}-V_{DS} characteristics under dark condition (Figure 3-7c). A nearly symmetric I-V curve was obtained with gate voltage within the range from -60 V to -20 V, while gradually evolved into rectifying diode behavior as the gate voltage shifts toward more positive direction. Similar gate-tunable rectifying behavior has been reported on different system.[38] In our case, such effect can be attributed to the transition from p-p to n-p junction at WP interface due to the ambipolar nature of WSe_2 under different gate bias.[39] Indeed, our control experiment on graphene/WSe_2/graphene (GWG) sandwich device confirms that similar ambipolarity can be observed in WSe_2 in the vertical configuration (Fig. 3-8). In this way, under a large negative gate bias, the WSe_2 is p-type and therefore forms a p-p junction with the p-type perovskite. With increasing gate voltage toward positive direction, the WSe_2 is turned into n-type material, and therefore forms an n-p junction with the p-type perovskite.

In Figure 3-7d and 3-7e, we consider the device under illumination. While the heterojunction device is within the p-p region (V_G = -60 V to -20 V), a small V_{OC} and weak gate-modulation were observed, which can be explained by the relative small built-in

potential across WP junction since both WSe_2 and perovskite are p-doped by the gate bias. With the V_G applied from -20 V to 0 V, a dramatic change occurs due to the switch of carrier type in WSe_2. The WSe_2 is now becoming n-type and forming n-p junction with p-type perovskite. As the positive V_G increases, the WSe_2 is more n-doped, while the perovskite remains p-type, which further increases the V_{OC}. However, the increasing positive V_G also reduces the p-type nature of perovskite, thus a smaller gate tuning V_{OC} slope was observed in n-p region compared to the transition region (Figure 3-7e). It is interesting to note the V_{OC} shows most dramatic change while the GWPG device is being switched from the p-p junction to n-p junction. To further look into the gate modulation of V_{OC}, we have plotted the absolute current of the device versus gate voltage and source-drain bias in a two-dimensional color-contour plot (Figure 3-7f). The current minimum (corresponding to V_{OC}) shows an obvious dependence on the gate voltage, highlighting the gate modulation of V_{OC}. The same gate-dependent measurement under dark condition shows no drift of current minimum with V_G, (Figure 3-7f inset), further confirming the drift of current minimum under light illumination is resulted from the gate-tuning of the photo-induced V_{OC}. It should be noted that such p-p to n-p transition was not observed in room temperature measurement (Figure 3-9). At room temperature, the ion motion mediated by vacancies[40] in perovskite is able to compensate the gate-field and thus prevent gate-modulation of WSe_2 from p-type to n-type. This has also verified the ion motion plays a substantial role in perovskite-based device. We believe more fundamental studies and continued optimization of these unique perovskite-2D heterostructure are needed for designing high performance optoelectronic applications.

F. Summary

In summary, we have developed a unique approach to integrate perovskite with 2D materials. We realized a high photoconductive gain up to ~2200 and a high photoresponsivity of ~950 A/W in a vertical GPG device structure. With the effective protection of BN for perovskite, we are able to extend the lifetime of such perovskite-2D material heterostructures up to 7 months. The low temperature measurement revealed the possibility of gate-tunable photovoltaic behavior based on perovskite devices, and offered important insights on how the ion motion affect the electrical properties of GPG based vertical device. The GWPG devices uncovered the potential to build a high on/off ratio vertical transistor based on perovskite materials and a gate-tunable photodiode by integrating other 2D materials beyond graphene. By combining their advantages in either optoelectronic or electronic properties, we are able to explore more underlying physical properties of this new promising perovskite material. In the future, we believe such platform is interesting and versatile. In additional to integrate with various 2D materials, the organohalide perovskites themselves have great tunability in band gap by engineering their composition.[6] One feasible way is to replace MAI with other halides or different halogenated organic molecules to react with exfoliated starting material PbI_2. Further investigation on such perovskite-2D material heterostructures will be beneficial for designing next generation hybrid optoelectronic device.

G. Reference

1. Cheng, H.-C.; Wang, G.; Li, D.; He, Q.; Yin, A.; Liu, Y.; Wu, H.; Ding, M.; Huang, Y.; Duan, X. *Nano Lett.* **2016,** 16, (1), 367-373.
2. Abate, A.; Saliba, M.; Hollman, D. J.; Stranks, S. D.; Wojciechowski, K.; Avolio, R.; Grancini, G.; Petrozza, A.; Snaith, H. J. *Nano Lett.* **2014,** 14, (6), 3247-3254.
3. Chen, Q.; Zhou, H.; Hong, Z.; Luo, S.; Duan, H.-S.; Wang, H.-H.; Liu, Y.; Li, G.; Yang, Y. *J. Am. Chem. Soc.* **2014,** 136, (2), 622-625.
4. deQuilettes, D. W.; Vorpahl, S. M.; Stranks, S. D.; Nagaoka, H.; Eperon, G. E.; Ziffer, M. E.; Snaith, H. J.; Ginger, D. S. *Science* **2015,** 348, (6235), 683-686.
5. Green, M. A.; Ho-Baillie, A.; Snaith, H. J. *Nature Photon.* **2014,** 8, (7), 506-514.
6. Jeon, N. J.; Noh, J. H.; Yang, W. S.; Kim, Y. C.; Ryu, S.; Seo, J.; Seok, S. I. *Nature* **2015,** 517, (7535), 476-480.
7. Lee, M. M.; Teuscher, J.; Miyasaka, T.; Murakami, T. N.; Snaith, H. J. *Science* **2012,** 338, (6107), 643.
8. Marchioro, A.; Teuscher, J.; Friedrich, D.; Kunst, M.; van de Krol, R.; Moehl, T.; Gratzel, M.; Moser, J.-E. *Nature Photon.* **2014,** 8, (3), 250-255.
9. Nie, W.; Tsai, H.; Asadpour, R.; Blancon, J.-C.; Neukirch, A. J.; Gupta, G.; Crochet, J. J.; Chhowalla, M.; Tretiak, S.; Alam, M. A.; Wang, H.-L.; Mohite, A. D. *Science* **2015,** 347, (6221), 522-525.
10. Stranks, S. D.; Eperon, G. E.; Grancini, G.; Menelaou, C.; Alcocer, M. J. P.; Leijtens, T.; Herz, L. M.; Petrozza, A.; Snaith, H. J. *Science* **2013,** 342, (6156), 341.
11. Yang, W. S.; Noh, J. H.; Jeon, N. J.; Kim, Y. C.; Ryu, S.; Seo, J.; Seok, S. I. *Science* **2015,** 348, (6240), 1234.

12. Zhou, H.; Chen, Q.; Li, G.; Luo, S.; Song, T.-b.; Duan, H.-S.; Hong, Z.; You, J.; Liu, Y.; Yang, Y. *Science* **2014,** 345, (6196), 542-546.

13. Lin, Q.; Armin, A.; Nagiri, R. C. R.; Burn, P. L.; Meredith, P. *Nature Photon.* **2015,** 9, (2), 106-112.

14. Shao, Y.; Xiao, Z.; Bi, C.; Yuan, Y.; Huang, J. *Nat. Commun.* **2014,** 5, 5784.

15. Im, J.-H.; Lee, C.-R.; Lee, J.-W.; Park, S.-W.; Park, N.-G. *Nanoscale* **2011,** 3, (10), 4088-4093.

16. Xing, G.; Mathews, N.; Sun, S.; Lim, S. S.; Lam, Y. M.; Grätzel, M.; Mhaisalkar, S.; Sum, T. C. *Science* **2013,** 342, (6156), 344-347.

17. Xiao, Z.; Yuan, Y.; Shao, Y.; Wang, Q.; Dong, Q.; Bi, C.; Sharma, P.; Gruverman, A.; Huang, J. *Nature Mater.* **2015,** 14, (2), 193-198.

18. Bai, S.; Wu, Z.; Wu, X.; Jin, Y.; Zhao, N.; Chen, Z.; Mei, Q.; Wang, X.; Ye, Z.; Song, T.; Liu, R.; Lee, S.-t.; Sun, B. *Nano Res.* **2014,** 7, (12), 1749-1758.

19. Tan, Z.-K.; Moghaddam, R. S.; Lai, M. L.; Docampo, P.; Higler, R.; Deschler, F.; Price, M.; Sadhanala, A.; Pazos, L. M.; Credgington, D.; Hanusch, F.; Bein, T.; Snaith, H. J.; Friend, R. H. *Nature Nanotech.* **2014,** 9, (9), 687-692.

20. Chin, X. Y.; Cortecchia, D.; Yin, J.; Bruno, A.; Soci, C. *Nat. Commun.* **2015,** 6, 7383.

21. Xing, G.; Mathews, N.; Lim, S. S.; Yantara, N.; Liu, X.; Sabba, D.; Grätzel, M.; Mhaisalkar, S.; Sum, T. C. *Nature Mater.* **2014,** 13, (5), 476-480.

22. Zhang, Q.; Ha, S. T.; Liu, X.; Sum, T. C.; Xiong, Q. *Nano Lett.* **2014,** 14, (10), 5995-6001.

23. Dong, R.; Fang, Y.; Chae, J.; Dai, J.; Xiao, Z.; Dong, Q.; Yuan, Y.; Centrone, A.; Zeng, X. C.; Huang, J. *Adv. Mater.* **2015,** 27, (11), 1912-1918.

24. Lee, Y.; Kwon, J.; Hwang, E.; Ra, C.-H.; Yoo, W. J.; Ahn, J.-H.; Park, J. H.; Cho, J. H. *Adv. Mater.* **2015,** 27, (1), 41-46.

25. Dou, L.; Yang, Y.; You, J.; Hong, Z.; Chang, W.-H.; Li, G.; Yang, Y. *Nat. Commun.* **2014,** 5, 5404.

26. Li, F.; Ma, C.; Wang, H.; Hu, W.; Yu, W.; Sheikh, A. D.; Wu, T. *Nat. Commun.* **2015,** 6, 8238.

27. Wang, L.; Meric, I.; Huang, P. Y.; Gao, Q.; Gao, Y.; Tran, H.; Taniguchi, T.; Watanabe, K.; Campos, L. M.; Muller, D. A.; Guo, J.; Kim, P.; Hone, J.; Shepard, K. L.; Dean, C. R. *Science* **2013,** 342, (6158), 614.

28. Liu, Y.; Wu, H.; Cheng, H.-C.; Yang, S.; Zhu, E.; He, Q.; Ding, M.; Li, D.; Guo, J.; Weiss, N. O.; Huang, Y.; Duan, X. *Nano Lett.* **2015,** 15, (5), 3030-3034.

29. Withers, F.; Del Pozo-Zamudio, O.; Mishchenko, A.; Rooney, A. P.; Gholinia, A.; Watanabe, K.; Taniguchi, T.; Haigh, S. J.; Geim, A. K.; Tartakovskii, A. I.; Novoselov, K. S. *Nature Mater.* **2015,** 14, (3), 301-306.

30. Britnell, L.; Ribeiro, R. M.; Eckmann, A.; Jalil, R.; Belle, B. D.; Mishchenko, A.; Kim, Y. J.; Gorbachev, R. V.; Georgiou, T.; Morozov, S. V.; Grigorenko, A. N.; Geim, A. K.; Casiraghi, C.; Neto, A. H. C.; Novoselov, K. S. *Science* **2013,** 340, (6138), 1311.

31. Wang, J. I. J.; Yang, Y.; Chen, Y.-A.; Watanabe, K.; Taniguchi, T.; Churchill, H. O. H.; Jarillo-Herrero, P. *Nano Lett.* **2015,** 15, (3), 1898-1903.

32. Sandroff, C. J.; Kelty, S. P.; Hwang, D. M. *J. Chem. Phys.* **1986,** 85, (9), 5337-5340.

33. Zhang, J.; Song, T.; Zhang, Z.; Ding, K.; Huang, F.; Sun, B. *J. Mater. Chem. C* **2015,** 3, (17), 4402-4406.

34. Wang, G.; Li, D.; Cheng, H.-C.; Li, Y.; Chen, C.-Y.; Yin, A.; Zhao, Z.; Lin, Z.; Wu, H.; He, Q.; Ding, M.; Liu, Y.; Huang, Y.; Duan, X. *Sci. Adv.* **2015,** 1, (9).

35. Ha, S. T.; Liu, X.; Zhang, Q.; Giovanni, D.; Sum, T. C.; Xiong, Q. *Adv. Opt. Mater.* **2014,** 2, (9), 838-844.

36. Cao, Y.; Mishchenko, A.; Yu, G. L.; Khestanova, E.; Rooney, A. P.; Prestat, E.; Kretinin, A. V.; Blake, P.; Shalom, M. B.; Woods, C.; Chapman, J.; Balakrishnan, G.; Grigorieva, I. V.; Novoselov, K. S.; Piot, B. A.; Potemski, M.; Watanabe, K.; Taniguchi, T.; Haigh, S. J.; Geim, A. K.; Gorbachev, R. V. *Nano Lett.* **2015,** 15, (8), 4914-4921.

37. Yu, W. J.; Liu, Y.; Zhou, H.; Yin, A.; Li, Z.; Huang, Y.; Duan, X. *Nature Nanotech.* **2013,** 8, (12), 952-958.

38. Jariwala, D.; Sangwan, V. K.; Wu, C.-C.; Prabhumirashi, P. L.; Geier, M. L.; Marks, T. J.; Lauhon, L. J.; Hersam, M. C. *Proc Natl Acad Sci USA* **2013,** 110, (45), 18076-18080.

39. Pospischil, A.; Furchi, M. M.; Mueller, T. *Nature Nanotech.* **2014,** 9, (4), 257-261.

40. Eames, C.; Frost, J. M.; Barnes, P. R. F.; O'Regan, B. C.; Walsh, A.; Islam, M. S. *Nat. Commun.* **2015,** 6, 7497.

H. Figures and legends

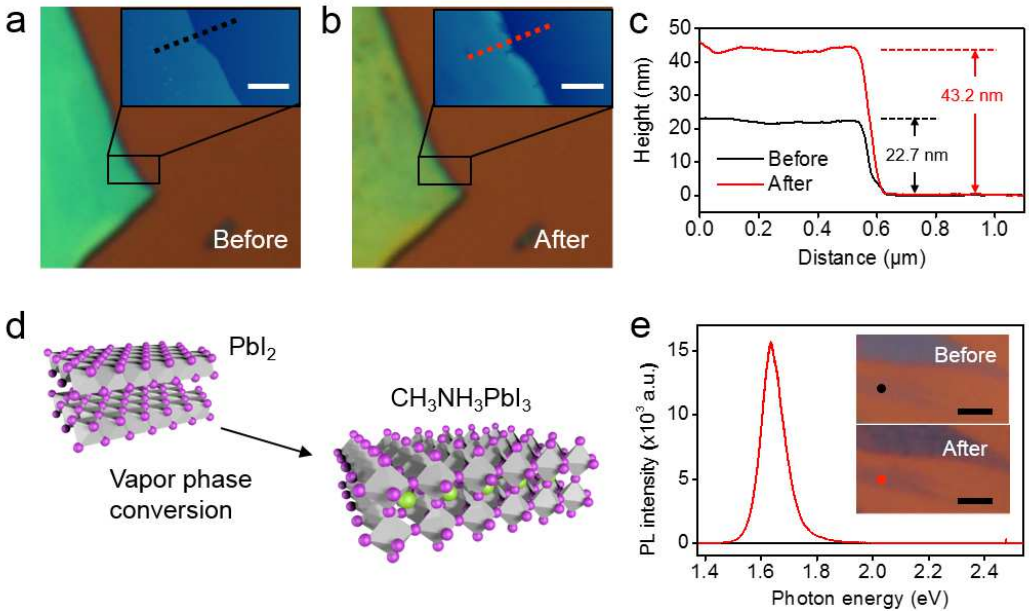

Figure 3-1. Conversion of exfoliated lead iodide flake into perovskite.

(a, b) The optical images of an exfoliated lead iodide flake before and after conversion process, the corresponding insets show the AFM images of the area marked by black rectangles in optical images. The white scale bars for AFM images in (a) and (b) are both 500 nm. (c) The sectional height profile extract from black and red dashed lines from the insets of (a) and (b), respectively. An increased thickness was observed after conversion. (d) Schematic of the structure change from layered PbI_2 to perovskite. (e) The black and red curves represent the corresponding photoluminescence spectra taken from the black and red spots shown in insets (optical images), respectively. A prominent emission peak at 1.63 eV was detected after conversion, which indicates a successful perovskite formation. (Adapted from [1])

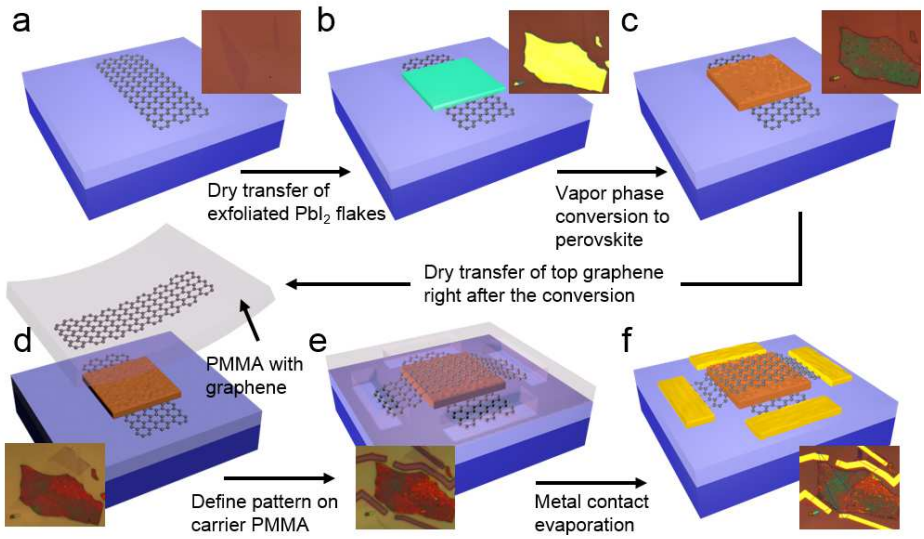

Figure 3-2. Schematics and optical images for each of steps of GPG device fabrication process.

(a) The bottom-graphene was first exfoliated on the top of 290 nm SiO_2/highly doped Si substrate. (b) The PbI_2 was exfoliated into small flakes and transferred to graphene. (c) The PbI_2/graphene stack was then converted into perovskite in the furnace with methylammonium iodide vapor carried by argon gas flow. (d) The as-converted perovskite was immediately covered with the separately prepared graphene/carrier PMMA stack. (e) The electrode patterns were defined directly on the carrier PMMA by e-beam lithography without additional spin-coating process. (f) After metal evaporation, the device was lift-off in chloroform. (Adapted from [1])

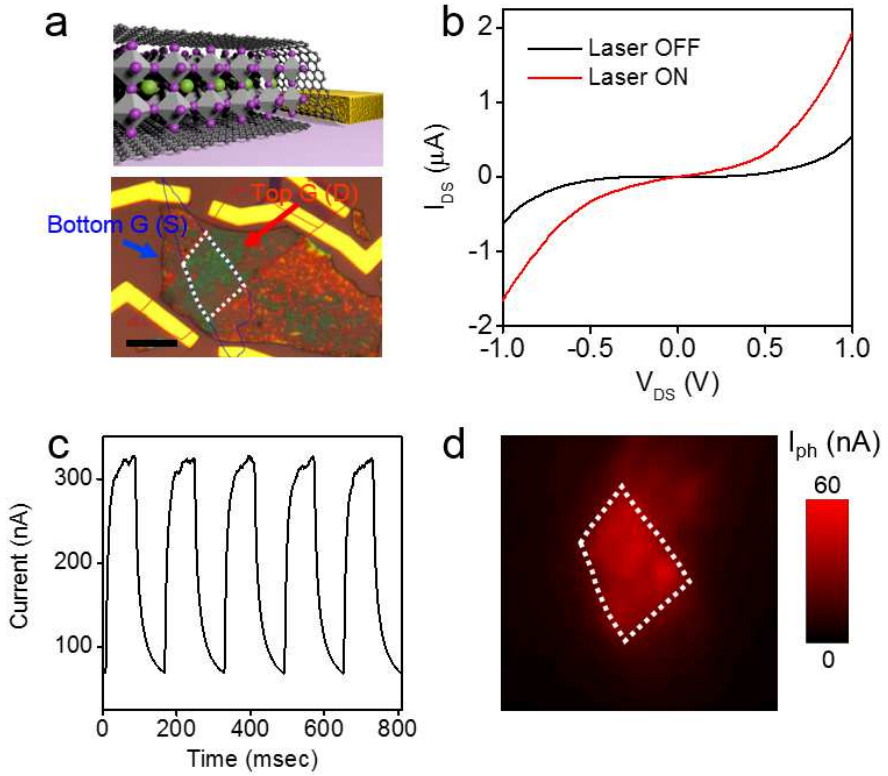

Figure 3-3. Photoconductive characterization of graphene/perovskite/graphene (GPG) vertical device.

(a) Schematic illustration and optical image of a GPG heterostructure device. The white dashed line outlines the overlapping area, the bottom-graphene and top-graphene are outlined by the blue and red solid lines, respectively. The top-graphene is biased (drain) while the bottom graphene is grounded (source) during all measurement. The black scale bar is 10 μm. (b) I_{DS}-V_{DS} curves of GPG device measured at room temperature (298 K) with/without laser illumination. A photo-induced current offset was observed. (c) The time-domain photocurrent response measured with constantly applied bias while illuminated by 532 nm laser (chopping frequency at 7 Hz). (d) The corresponding photocurrent map for the device shown in (a). The major contribution of photocurrent was from the outlined GPG overlapping area in (a). All measurement presented above were conducted at 298 K. (Adapted from [1])

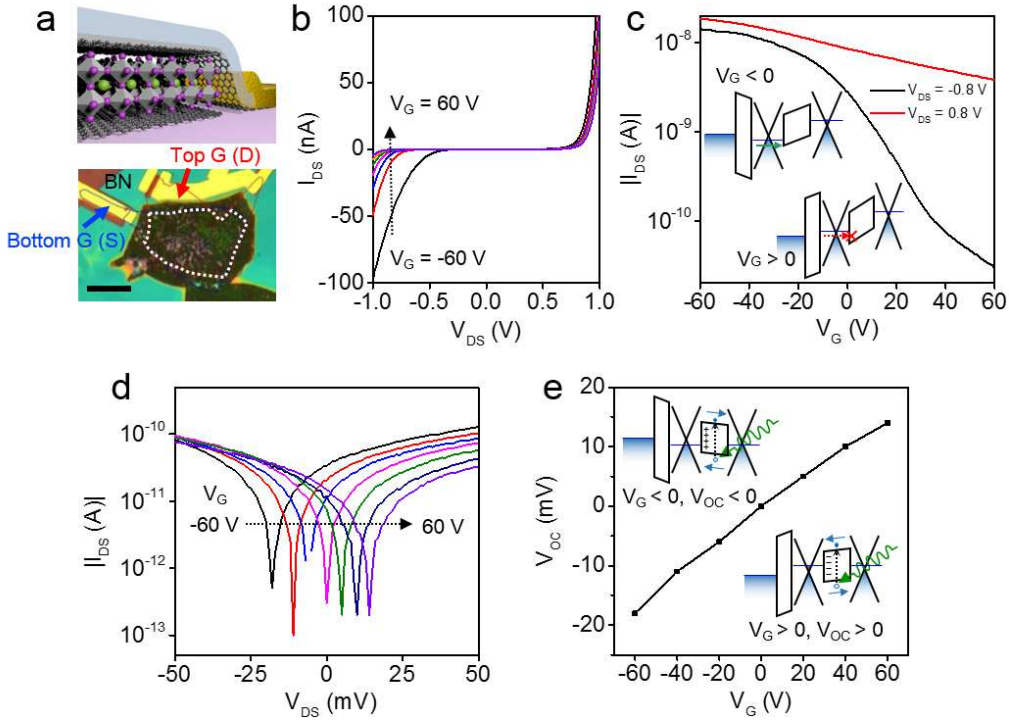

Figure 3-4. Optoelectronic characterization on BN-covered GPG device at 77K.

(a) The device schematic and optical image of a BN-covered GPG device. The BN-covered top- and bottom-graphene were connected to the metal electrodes by edge contacts. The red and blue lines framed the top- and bottom-graphene, respectively; and the white dashed line outlines the GPG overlapping area. The bias is applied to top-graphene while the bottom graphene is grounded during all measurement. The black scale bar is 10 μm. (b) The dark I_{DS}-V_{DS} characteristics measured under different gate voltage. The negatively-biased regime show much bigger gate modulation than the positively-biased regime. (c) The transfer characteristics of the device when biased at -0.8 V (black) and 0.8 V (red). The negatively-biased curve shows a larger on/off ratio of ~500 compared to positively-biased one which is only about ~5. The two band diagrams show negatively-biased condition under positive and negative gate voltage. As $V_G < 0$ (> 0), the hole-injection barrier decreases (increases), the device current increases (decreases). The green arrow indicates an effective hole-injection while the red dashed arrow indicates the blocked hole injection. (d) The logarithmic plot of I_{DS}-V_{DS} curves obtained by sweeping at smaller bias voltage range under continuous laser illumination. The open-circuit voltage (V_{OC}) was obtained from current minima and able to be modulated from negative to positive while

the gate voltage is varied from -60 V to 60 V (20 V increment). The dashed arrow indicates the order of gate-voltage varying sequence. (e) The gate-dependent V_{OC} extracted from (d). The band diagrams depict the gate-tunable V_{OC} and the ion accumulation effect that reduces the gate-modulation of photovoltaic effect in GPG device. All measurement presented above were conducted at 77 K. (Adapted from [1])

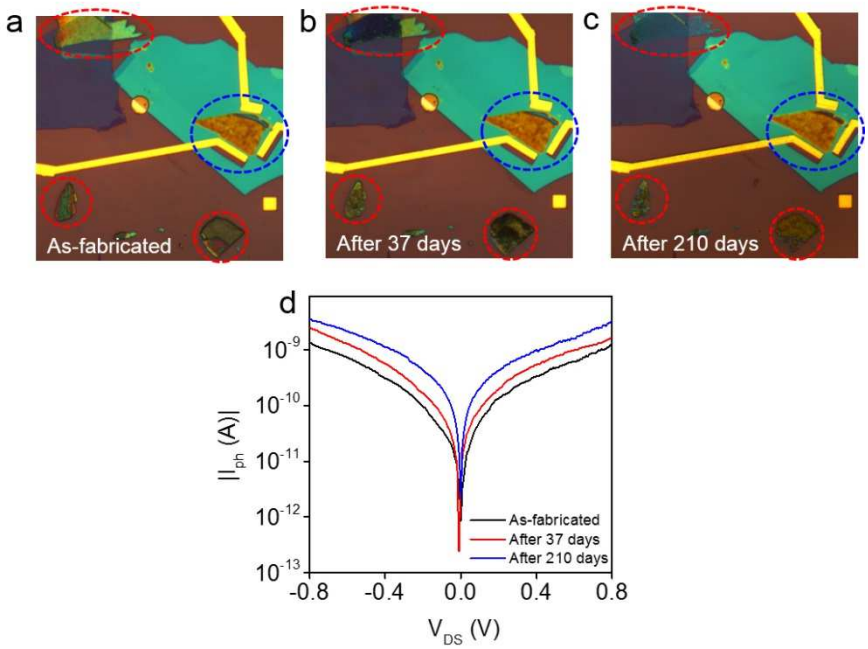

Figure 3-5. Improved stability of BN-covered GPG device.

(a) Optical image of a BN-covered GPG device taken right after lift-off process. The red dashed circles indicate some other perovskite flakes that were not covered by BN, while the BN-covered device is indicated by a blue dashed circle. (b) Optical image of the same spot taken after 37 days stored in desiccator. All exposed perovskite flakes showed some damage, especially the one sitting on the multilayer graphene (upper left corner) had a considerable damage compared other part that sitting on the SiO_2. It might be due to the reactivity of graphene that accelerates the decomposition of perovskite. On the other hand, no visible damage was observed in BN-covered device. (c) Optical image of the same spot taken after 210 days stored in desiccator. The uncovered flakes were seriously damaged, while the covered device remains intact. (d) The logarithmic plots of photocurrent I_{ph} = ($I_{illuminated} - I_{dark}$) versus bias voltage were obtained by measuring at the conditions shown in (a), (b) and (c). No degradation in terms of photocurrent performance was observed. The

photocurrent gain seems to increase over time, the reason for that is unclear, possibly due to the improved contact between perovskite and graphene. (Adapted from [1])

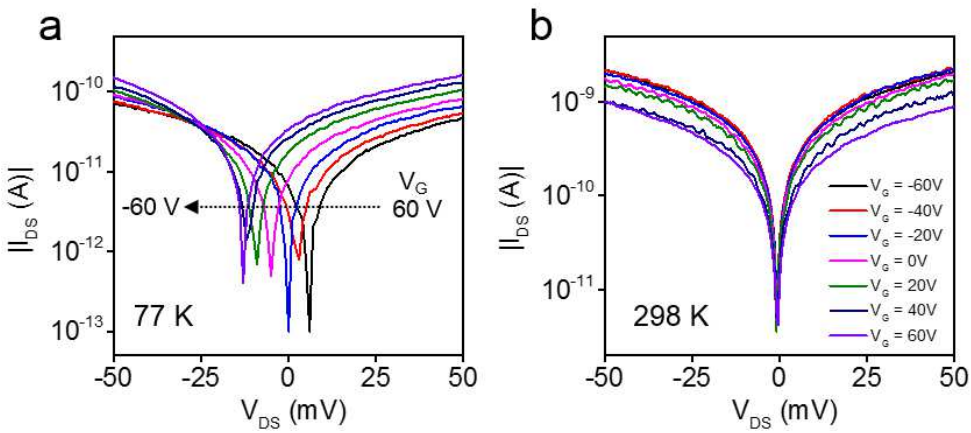

Figure 3-6. Gate-tunable photovoltaic effect in GPG device.

(a) The illuminated I_{DS}-V_{DS} curves of GPG device measured at 77 K with the back gate voltage swept from 60V to -60V, which shows a consistent V_{OC} shift as the one shown in Fig. 3d of the main text (from -60 V to 60 V). (b) Room temperature measurement of the same device shown in (a). No gate-dependent V_{OC} shift was obtained. (Adapted from [1])

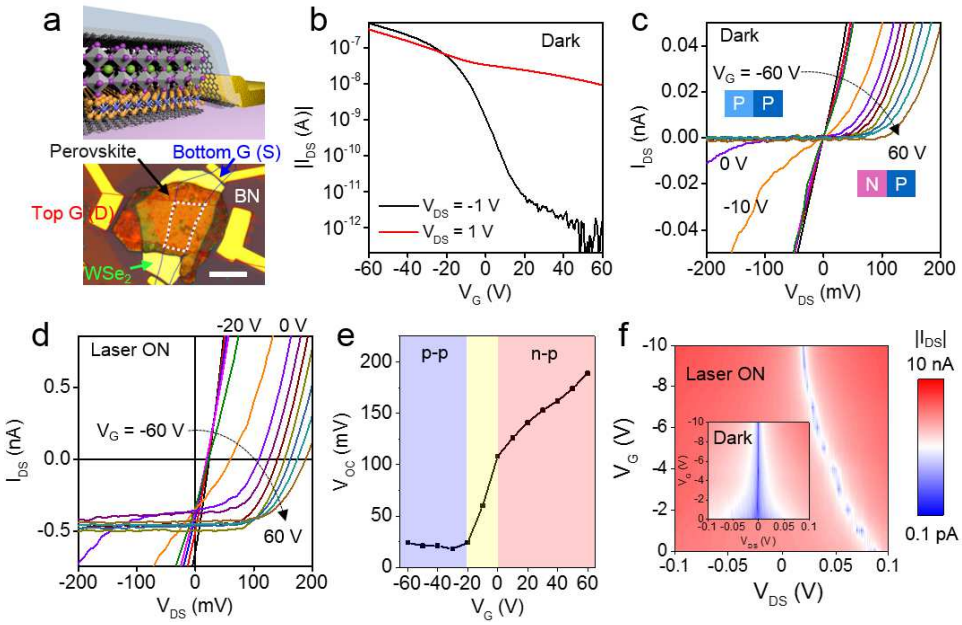

Figure 3-7. Optoelectronic characteristics of graphene/WSe_2/perovskite/graphene (GWPG) heterostructure devices.

(a) The schematic illustration and optical image of a BN-covered GWPG device. The red and blue lines framed the top- and bottom-graphene, respectively; the perovskite and WSe_2 are indicated by black and green arrows, respectively; the white dashed lines outline the overlapping area of GWPG structure. The top-graphene is biased while the bottom graphene is grounded for all measurements. (b) The transfer characteristics of the GWPG device when biased at -1 V (black) and 1 V (red). The negatively-biased curve shows a large on/off ratio around 10^6 while the positively-biased one is only ~35. (c) The dark I_{DS}-V_{DS} characteristics of GWPG device show an obvious transition from symmetric p-p junction to rectifying n-p diode as V_G varied from -60 V to 60 V (10 V increment). In the negative bias range, the I_{DS} current shows a dramatic decrease from V_G = -10 V (orange) to 0 V (purple). (d) The I_{DS}-V_{DS} obtained under laser 532 nm illumination with varied V_G (10 V increment). (e) The gate-dependent V_{OC} extracted from (d). The blue area is p-p junction regime (V_G = -60 V to -20 V) where V_{OC} is small with little gate-modulation; the yellow area (V_G = -20 V to 0 V) is the transition region where V_{OC} shows dramatic change with gate voltage; the red area is n-p junction region where V_{OC} increases slightly less than transition area with gate voltage. (f) The logarithmic plot of laser-illuminated I_{DS}-V_{DS} curves under different gate voltage (1V increment) within transition region. A significant

open-circuit voltage V_{OC} (current minima) shift was observed as the gate bias varied, while the dark I_{DS}-V_{DS} plots shown in the inset has no change of current minima with the gate bias. All measurement presented above were conducted at 77 K. (Adapted from [1])

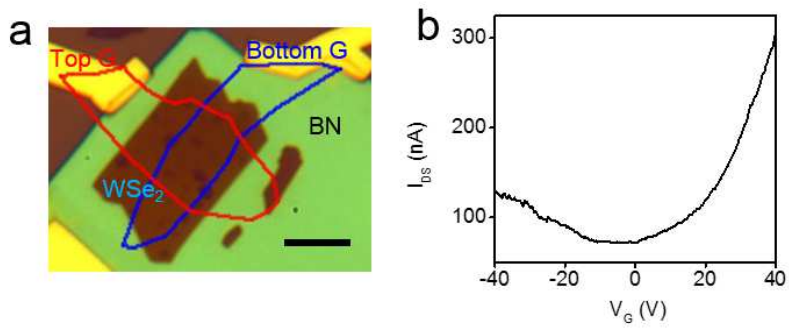

Figure 3-8. Ambipolarity of graphene/WSe_2/graphene (GWG) heterostructure device.

(a) Optical image of GWG device. The red and blue lines framed the top- and bottom-graphene. A WSe_2 flake with similar thickness to GWPG device was used. The black scale bar is 5 μm. (b) An ambipolar transfer characterisitic of GWG device was obtained with bias voltage = -0.5 V. (Adapted from [1])

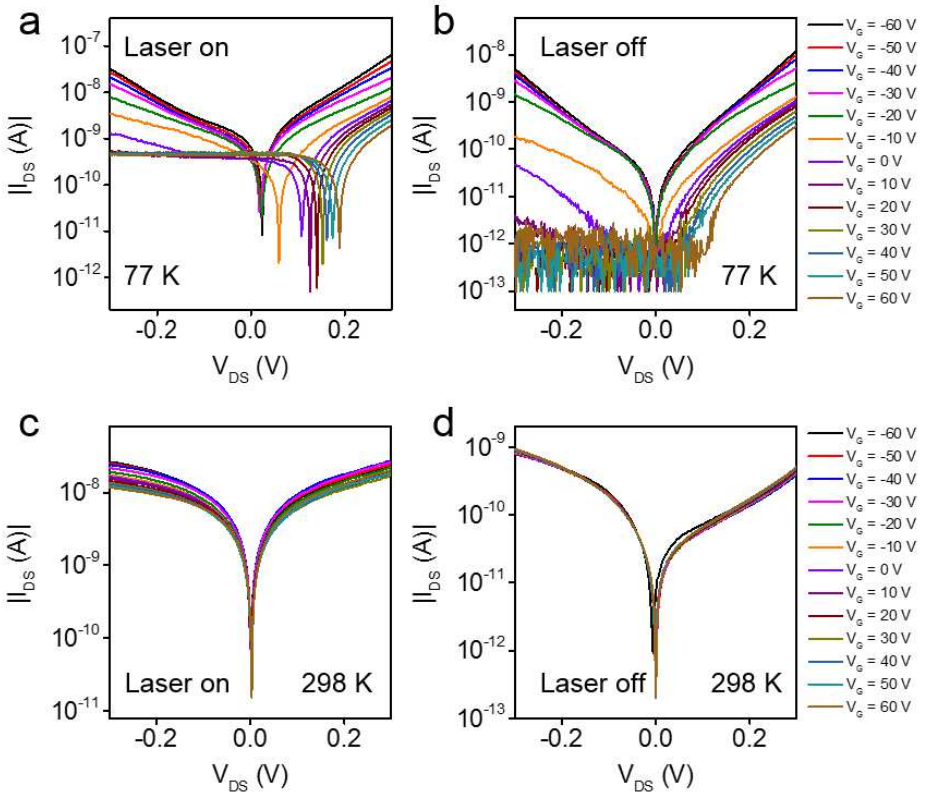

Figure 3-9. Gate-tunable photovoltaic effect in GWPG device.

(a, b) Logarithmic plot of I_{DS}-V_{DS} characteristics of GWPG device measured at 77 K with/without 532 nm laser illumination, respectively. Under illumination, the V_{OC} can be effectively modulated by gate voltage. The dark I_{DS}-V_{DS} shows a distinct transition from p-p to n-p regime. (c, d) Room temperature measurement of the same device shown in (a, b). No p-p to n-p transition and gate-tuning V_{OC} were observed. (Adapted from [1])

CHAPTER IV: IONIC SOLID INDUCED DOPING IN TWO-DIMENSIONAL MATERIAL DEVICES

A. Introduction

Electrostatic doping has been widely used in low-dimensional materials, including carbon nanotube (CNT), graphene and atomically thin transitional metal dichalcogenides (TMDCs).[1-11] The traditional doping method involving alien atom insertion may damage the lattice of these materials, and affect the carrier transport in low-dimensional materials. A well-adopted method to control the carrier density as well as the dominant carrier type is to fabricate devices in field-effect geometry. For example, a p-n junction can be readily created on an ambipolar material *via* split gates.[1, 3-7, 9-11] With field-effect doping, the fundamental junction properties can be examined and reconfigured without physically damaging the materials. Despite the fact that the split gates provide a well-controlled junction and effective carrier doping, such devices usually require complicated fabrication process. Recently, ionic liquid induced doping has been applied to monolayer WSe_2 to create a p-n junction, which allows effective circularly polarized emission generated from strong spin-valley coupling.[2, 8] In this configuration, split gates are no longer needed to create a p-n junction, instead, the positive and negative ions in ionic liquid can electrostatically modulate the carrier density in WSe_2 devices. By poling the ionic liquid at room temperature, the positive and negative ions can accumulate at both ends of the device and actively induce a n-type and p-type region in WSe_2 under enough large bias voltage. Such a p-n junction can be further stabilized at low temperature to freeze the ions and keep the status of the devices.[2, 8] However, the ionic liquid can only be applied to entire sample, and its liquid form may limit the design of solid-state electronic devices. Here we propose

a doping strategy for two-dimensional materials by employing ionic solid to facilitate the doping and even the formation of p-n junction in TMDC based materials. In this study, we investigated the space charge doping effect in ionic solids including lead halide and organometal perovskites. We demonstrated that a p-n junction can be created on monolayer TMDC field-effect transistors (FETs) *via* solid-state electrical poling process. Moreover, unlike ionic liquid, the ionic solid offers local control of doping in 2D materials, enabling various design for solid-state electronic devices.

B. Ion migration in lead halide based materials

Recently, organometal halide perovskite has become a promising material because of their excellent properties for solar cell application.[12-23] However, this type of perovskite is an ionic solid composed of organic cations, metal cations and halide anions. It has been reported that the ion migration in perovskite may occur under applied electric field, which is also considered as one of the origins causing the hysteresis in the voltage dependent photocurrent.[24-28] On the other hand, Xiao *et al.* reported a switchable photovoltaic effect in $MAPbI_3$.[29] They have created a switchable p-i-n junction on $MAPbI_3$ both in lateral and vertical direction by poling the material with electric field. Both switchable open-circuit voltage (V_{OC}) and short-circuit current (J_{SC}) were observed after poling process. They suggest the migration of positively charged ions and negatively charged ions could induce an n-type and p-type regions in the perovskite, respectively. Such ion migration effect is similar to ion accumulation effect in ionic liquid under electric field.[2, 8] Here we investigated ionic doping effect in TMDC FETs by using ionic solid including lead halides and lead halide perovskites. We show that the $MAPbI_3$ can serve a non-covalent doping

agent which could locally induce p-type and n-type regions in TMDC devices. Lead halides including PbI_2 and $PbBr_2$ can induce p-type doping effect to TMDC devices. Moreover, $PbBr_2$ were found to be able to readily change the threshold voltage of WSe_2 devices by changing the gate-sweeping direction. With well-defined geometry of ionic solid, we are able to partially dope on one side of the device and create functional heterostructure, which could enable more design capability than previous ionic liquid based doping. Such controllable doping effect can be used to enhance to optoelectronic properties of TMDCs based devices or even create a switchable p-n junction, thus facilitating the extraction of photo-generated carriers due to strong built-in electric field. Such platform can be further applied to other 2D materials based electronic devices.

C. Methods

Device fabrication

To fabricate WSe_2 device in field-effect geometry, WSe_2 monolayer samples were first exfoliated on an oxygen plasma treated 290 nm SiO_2/Si substrate. The device pattern is defined by electron-beam lithography, followed by metal deposition (30 nm Au) in an electron-beam evaporator for the contact electrodes of WSe_2 devices. The PbI_2 preparation is described in Chapter II. After PbI_2 transfer process, the PbI_2 sitting on WSe_2 can be further converted into MAPbI3 using the method discussed in Chapter II.[30] To ensure the stability of the devices, another separately prepared boron nitride (BN) is used to cover the entire area of perovskite after conversion process.

Device characterization

The device characterization details is described in the Methods of Chapter III.

D. PbI_2 and $MAPbI_3$ induced p-type doping in WSe_2 FETs

To elucidate the doping effect introduced by ionic solid, field-effect transistors based on monolayer WSe_2 were adopted due to their ambipolarity which may facilitate the observation of both n-type and p-type doping effect. As shown in Figure 4-1, for the sake of comparison, two of three equally spaced electrodes were placed on WSe_2, followed by the dry transfer of PbI_2 flake covering all three electrodes, in which we are able to compare the device properties of PbI_2/WSe_2 and $MAPbI_3/WSe_2$ hybrid structure, and the pure PbI_2 and $MAPbI_3$ device. The transfer curves are summarized in Figure 4-1d, e. Before the PbI_2 transfer step, the WSe_2 FET shows a regular ambipolarity with slightly p-doping. After PbI_2 transfer, the WSe_2 was apparently p-doped, which might be due the large work function difference (φ = 6.35 eV) between PbI_2 and WSe_2 (φ = 4.04 eV).[31, 32] On the other hand, the PbI_2 channel shows no detectable current under dark condition, while the current is 10 times higher at illuminated condition due to photo-generated carriers driven by the applied electric field in PbI_2. It is noted that after the conversion process, the $MAPbI_3/WSe_2$ hybrid device shows even stronger p-doping than PbI_2 doped device, however, the transconductance is reduced. This might be due to more prominent ion migration effect in $MAPbI_3$, which could screen the gate electric field and result in smaller gate-modulation.[17, 33, 34] The current in $MAPbI_3$ channel is at least three orders of magnitude less than $MAPbI_3/WSe_2$ channel, hence, the $MAPbI_3$ only serves as a doping agent instead of a conducting channel. By comparing the device current measured under illumination and dark condition, we obtained the photocurrent ($I_{ph} = I_{light} - I_{dark}$) for both hybrid $MAPbI_3/WSe_2$ ($I_{ph,\ hybrid}$) device and $MAPbI_3$ ($I_{ph,\ MAPbI3}$) device. We found that the $I_{ph,\ hybrid}$

is more than 4 orders of magnitude higher than ($I_{ph, MAPbI3}$) as V_G = -40 V and more than 3 orders of magnitude higher when V_G = 40 V, implying that the $MAPbI_3/WSe_2$ channel can be much more efficient than $MAPbI_3$ itself in terms of photo-carrier extraction.

E. Ionic doping effect in partial $MAPbI_3/MoS_2$ hybrid devices

Unlike ionic liquid doping, the ionic solid allows more flexible design for solid-state electronic devices. Here we investigate the doping effect of $MAPbI_3$ in MoS_2 FET by partially covering the MoS_2 channel with $MAPbI_3$, creating a junction of p-doped MoS_2 and intrinsic n-type MoS_2. As shown in Figure 4-2, the device shows a right shift of the threshold voltage due to p-doping induced by $MAPbI_3$ at room temperature, which is consistent to what we have observed in WSe_2 FET. On the other hand, we also investigated the doping effect when the ion migration is suppressed. The transfer curves of the same device measured at 77 K shows a left shift in threshold voltage, implying that the migrating halide ions might be the dominant doping agents which are known to induce prominent p-doping[29] and migrate easily than positive charged cations in $MAPbI_3$.[28] With such a partially doped device, a p-n junction can be created on the monolayer MoS_2 channel. Figure 4-3 shows the transfer and output characteristics of the $MAPbI_3/MoS_2$ hybrid device measured under dark condition. It is shown that, the positively biased condition has larger on current and gate response than negatively biased condition. The reason can be understood by the difference of conductivity in these two distinct region ($MAPbI_3/MoS_2$ and pristine MoS_2). Under positive bias voltage, the device current is controlled by the injecting electrons from B electrode (grounded) to A electrode in Figure 4-2. At the junction region, the electrons is injected from intrinsic part to doped part of MoS_2, in which

the intrinsic part can readily be modulated by gate-field, thus the device current can be easily modulated by the varying gate voltage. On the other hand, under negatively bias voltage, the device current is now controlled by electron injection doped part to intrinsic part of MoS_2. Due to the larger resistivity and ionic screening effect of doped-MoS_2, the device current is much smaller and less affected by the gate-modulation, therefore a clear asymmetric output characteristics were observed. Ionic solid provides a more flexible way to dope the channel of 2D materials than ionic liquid, which can also facilitate the design of 2D material based electronic devices.

F. Controllable p-n junction formation in $MAPbI_3/WSe_2$ hybrid devices

To explore more capability of doping with ionic solid, we have investigated the possibility to directly create a switchable p-n junction diode in $MAPbI_3/WSe_2$ hybrid devices. As an ionic solid with migrating ion species, the $MAPbI_3$ can be polarized with electric field, thereby facilitating conceivable ion migration which could induce p-type and n-type doping in WSe_2 by the accumulated negative ions and positive ions on both ends, respectively.

The transfer curves and current-voltage characteristics (I_{DS}-V_{DS}) of a pristine monolayer WSe_2 devices are shown in Figure 4-4a. At $V_G = 0$ V, the device is in the OFF-state, no current was measured even under white light excitation. By using aforementioned water-free dry transfer method, we transferred a thin flake of lead iodide to cover the entire channel of WSe_2. The lead iodide was then converted to $MAPbI_3$ using the method described in Chapter II. For stability consideration, the as-converted device was then covered with a thin boron-nitride (BN) layer. Subsequently, the $MAPbI_3/WSe_2$ hybrid

device was measured under white light and laser excitation in vacuum. The I_{DS}-V_{DS} curves in Figure 4-4d show an asymmetric behavior as well as a small open-circuit voltage V_{OC} (~30 mV) under light and laser excitation was measured. This may be due to a slight poling effect by an initial applied bias at the A electrode with the B electrode grounded. In order to achieve effective poling effect on WSe_2, the substrate temperature is raised up to 400 K to enhance the ion migration process. In order to highlight the effect of poling, a large bias voltage (-10 V) was applied against the initial polarity of the device at 400 K. The substrate was then cooled down to 77 K after 5 min poling at 400 K with continuously applied bias voltage to stabilize the ions. During this negative poling process, the negative ions is supposed to migrate to B electrode while the positive ions should migrate to A electrodes. As shown in Figure 4-5, after negative poling, the output curves (measured with B electrode grounded) shows a completely opposite diode behavior compared to original condition, in which the turn-on voltage become negative. In addition, a V_{OC} = -0.88 V under white light excitation is achieved, while V_{OC} = -0.78 V is obtained under laser excitation. In order to estimate the performance of this $MAPbI_3/WSe_2$ hybrid structure device, we compared the output curves measured under dark and laser excitation. A short-circuit current I_{SC} ~49.4 pA is obtained, hence, we can extract the external quantum efficiency (EQE) by the formula EQE = $(I_{SC}/P_{laser})(hc/e\lambda)$, where P_{laser} is the total effective power of incident photons, *h, c* and *e* are Planck's constant, the speed of light and electron charge, respectively. The EQE of 66.65% at 532 nm was extracted, which is much higher than previously reported EQE of 0.2% at 522 nm in WSe_2 FET with split-gate defined p-n junction.[1] Such strong enhancement can be understood by the strong optical absorption and re-emission from the $MAPbI_3$, thereby enhancing the photoresponse of WSe_2. To

understand the stability of this p-n junction, the sample temperature was raised up to 298 K, 350 K and 400 K. As shown in Figure 4-6 The V_{OC} decreases from -0.9 V (77 K), -0.55 V (298 K), -0.5 V (350 K) and finally drop to -0.25 V at 400 K, showing that the ions tend to redistribute at high temperature and eliminate the internal field built up at both ends. In order to verify the ion migration induced p-n junction is a controllable process, a positive bias (+10 V) was then applied to the same device at 400 K, followed by the same cool down process as we previously used for negative poling. The results show that the V_{OC} is switched to 0.89 V (under white light) and 0.75 V (under laser excitation), which are both very close to the previous results achieved by negative poling. The V_{OC} dropped to 0.6 V after heating up the sample to room temperature, which is also consistent with what we obtained in negative poling (-0.55 V). Such highly consistent and switchable diode behaviors demonstrate that the polarity of the $MAPbI_3/WSe_2$ hybrid diode is indeed governed by the controllable ion migration. To elucidate the photocurrent contribution in the hybrid diode, we have examined the poling effect in the $MAPbI_3/WSe_2$ hybrid device and the $MAPbI_3$ only device in Figure 4-1c. During the poling process, the voltage is applied to both top and bottom electrode at all times with the middle electrode grounded. Figure 4-7 show that the I_{DS}-V_{DS} curves after poling process for both devices. It is noted that the $WSe_2/MAPbI_3$ hybrid device shows prominent ON-OFF diode behaviors under dark and laser excitation, while the $MAPbI_3$ device shows negligible current and diode behavior under dark condition. This has demonstrated that the device current and diode behaviors are mainly contributed by the WSe_2 channel instead of the $MAPbI_3$. The $MAPbI_3$ here is acting more like a sensitizer and a tunable doping agent.

G. Ion-migration induced p-n junction in graphene contact WSe_2 FETs

Graphene has been recently demonstrated to be a promising contact material for MoS_2 FETs due to its tunable work function which eliminates the contact barrier between graphene and MoS_2 as the device in the ON-state.[35] To further improve the performance of $MAPbI_3/WSe_2$ hybrid diode, we have investigated the device performance by using graphene as tunable electrical contacts. Unlike metal based electrode, the work function of graphene can also be tuned by accumulated ions during the poling process, resulting preferable p-type (n-type) electrical contact for p-type (n-type) region of WSe_2. Similar to metal contacted device, we have first investigated the doping effect induced by ionic solid in graphene contacted devices. Figure 4-8 shows transfer curves measured under dark and illuminated conditions before PbI_2 transfer, after PbI_2 transfer and after conversion to $MAPbI_3$. The pristine graphene-contacted WSe_2 FET shows a symmetric gate response despite some hysteresis observed during the sweeping, which may be due to the residual moisture at the interface between WSe_2 and substrate.[36] After PbI_2 transfer, the transfer curves shows a clear p-type doping similar to metal-contacted hybrid device. However, the gate-response is reduced under illuminated condition, which may be due to screening effect from the photo-generated carriers. In Figure 4-8c, the $MAPbI_3/WSe_2$ hybrid device shows more prominent p-doping and photoresponse than PbI_2/WSe_2 device in the transfer curve, which are consistent with results obtained from metal-contacted devices.

By using the equivalent electric field (1.67 V/μm) as used for the device in Figure 4-5 and 4-6, we have observed an improved prominent V_{OC} compared to the device shown in Figure 4-5 and 4-6. Moreover, the I_{DS}-V_{DS} curves under laser excitation exhibits a gate-tunable V_{OC} from 0 to -0.96 V, along with widely tunable EQE from 2.7 to 91.3% (see

Figure 4-9d), demonstrating that the tunable graphene contact, compared to metal electrodes, allows efficient extraction of photo-generated carriers as well as offering more tunability to the optoelectronic properties of the devices.

H. Summary

In Summary, the $MAPbI_3/WSe_2$ hybrid device has been demonstrated to have an enhanced photoresponse because of greatly improved optical absorption with $MAPbI_3$ absorber. We have further employed perovskites as an efficient and controllable doping agents in MoS_2 and WSe_2 as well as demonstrating that a switchable $MAPbI_3/WSe_2$ hybrid p-n diode can deliver a large $V_{OC,}$ up to 0.78 V with an EQE of 66.65% at 532 nm. Moreover, the $MAPbI_3/WSe_2$ hybrid diode with graphene contacts shows improved gate-tunable optoelectronic properties with a V_{OC} up to 0.96 V, along with an electrostatically tunable EQE from 2.7 to 91.3% at 532 nm has been achieved. With the ionic solid induced p-n junction in 2D materials, we could explore more intriguing electronic and optoelectronic properties of 2D materials with a much simpler device design as well as the enhanced optoelectronic properties with a ionic light absorber or emitter.

I. Reference

1. Baugher, B. W. H.; Churchill, H. O. H.; Yang, Y.; Jarillo-Herrero, P. *Nature Nanotech.* **2014,** 9, (4), 262-267.
2. Zhang, Y. J.; Ye, J. T.; Yomogida, Y.; Takenobu, T.; Iwasa, Y. *Nano Lett.* **2013,** 13, (7), 3023-3028.
3. Ross, J. S.; Klement, P.; Jones, A. M.; Ghimire, N. J.; Yan, J.; Mandrus, D. G.; Taniguchi, T.; Watanabe, K.; Kitamura, K.; Yao, W.; Cobden, D. H.; Xu, X. *Nature Nanotech.* **2014,** 9, (4), 268-272.
4. Pospischil, A.; Furchi, M. M.; Mueller, T. *Nature Nanotech.* **2014,** 9, (4), 257-261.
5. Williams, J. R.; DiCarlo, L.; Marcus, C. M. *Science* **2007,** 317, (5838), 638.
6. Choi, J.-H.; Lee, G.-H.; Park, S.; Jeong, D.; Lee, J.-O.; Sim, H. S.; Doh, Y.-J.; Lee, H.-J. *Nat. Commun.* **2013,** 4, 2525.
7. Gabor, N. M.; Zhong, Z.; Bosnick, K.; Park, J.; McEuen, P. L. *Science* **2009,** 325, (5946), 1367.
8. Zhang, Y. J.; Oka, T.; Suzuki, R.; Ye, J. T.; Iwasa, Y. *Science* **2014,** 344, (6185), 725.
9. Mueller, T.; Kinoshita, M.; Steiner, M.; Perebeinos, V.; Bol, A. A.; Farmer, D. B.; Avouris, P. *Nature Nanotech.* **2010,** 5, (1), 27-31.
10. Sundaram, R. S.; Engel, M.; Lombardo, A.; Krupke, R.; Ferrari, A. C.; Avouris, P.; Steiner, M. *Nano Lett.* **2013,** 13, (4), 1416-1421.
11. Gabor, N. M.; Song, J. C. W.; Ma, Q.; Nair, N. L.; Taychatanapat, T.; Watanabe, K.; Taniguchi, T.; Levitov, L. S.; Jarillo-Herrero, P. *Science* **2011,** 334, (6056), 648.

12. Dong, Q.; Fang, Y.; Shao, Y.; Mulligan, P.; Qiu, J.; Cao, L.; Huang, J. *Science* **2015,** 347, (6225), 967.

13. De Wolf, S.; Holovsky, J.; Moon, S.-J.; Löper, P.; Niesen, B.; Ledinsky, M.; Haug, F.-J.; Yum, J.-H.; Ballif, C. *J. Phys. Chem. Lett.* **2014,** 5, (6), 1035-1039.

14. Lee, M. M.; Teuscher, J.; Miyasaka, T.; Murakami, T. N.; Snaith, H. J. *Science* **2012,** 338, (6107), 643.

15. Stranks, S. D.; Eperon, G. E.; Grancini, G.; Menelaou, C.; Alcocer, M. J. P.; Leijtens, T.; Herz, L. M.; Petrozza, A.; Snaith, H. J. *Science* **2013,** 342, (6156), 341.

16. Yang, W. S.; Noh, J. H.; Jeon, N. J.; Kim, Y. C.; Ryu, S.; Seo, J.; Seok, S. I. *Science* **2015,** 348, (6240), 1234.

17. Cheng, H.-C.; Wang, G.; Li, D.; He, Q.; Yin, A.; Liu, Y.; Wu, H.; Ding, M.; Huang, Y.; Duan, X. *Nano Lett.* **2016,** 16, (1), 367-373.

18. Jeon, N. J.; Noh, J. H.; Yang, W. S.; Kim, Y. C.; Ryu, S.; Seo, J.; Seok, S. I. *Nature* **2015,** 517, (7535), 476-480.

19. Im, J.-H.; Lee, C.-R.; Lee, J.-W.; Park, S.-W.; Park, N.-G. *Nanoscale* **2011,** 3, (10), 4088-4093.

20. Dou, L.; Yang, Y.; You, J.; Hong, Z.; Chang, W.-H.; Li, G.; Yang, Y. *Nat. Commun.* **2014,** 5, 5404.

21. Cho, H.; Jeong, S.-H.; Park, M.-H.; Kim, Y.-H.; Wolf, C.; Lee, C.-L.; Heo, J. H.; Sadhanala, A.; Myoung, N.; Yoo, S.; Im, S. H.; Friend, R. H.; Lee, T.-W. *Science* **2015,** 350, (6265), 1222.

22. Veldhuis, S. A.; Boix, P. P.; Yantara, N.; Li, M.; Sum, T. C.; Mathews, N.; Mhaisalkar, S. G. *Adv. Mater.* **2016,** 28, (32), 6804-6834.

23. Brenner, T. M.; Egger, D. A.; Kronik, L.; Hodes, G.; Cahen, D. *Nature Reviews Materials* **2016,** 1, 15007.

24. Miyano, K.; Yanagida, M.; Tripathi, N.; Shirai, Y. *J. Phys. Chem. Lett.* **2016,** 7, (12), 2240-2245.

25. Levine, I.; Nayak, P. K.; Wang, J. T.-W.; Sakai, N.; Van Reenen, S.; Brenner, T. M.; Mukhopadhyay, S.; Snaith, H. J.; Hodes, G.; Cahen, D. *J. Phys. Chem. C* **2016,** 120, (30), 16399-16411.

26. Li, C.; Tscheuschner, S.; Paulus, F.; Hopkinson, P. E.; Kießling, J.; Köhler, A.; Vaynzof, Y.; Huettner, S. *Adv. Mater.* **2016,** 28, (12), 2446-2454.

27. Eames, C.; Frost, J. M.; Barnes, P. R. F.; O'Regan, B. C.; Walsh, A.; Islam, M. S. *Nat. Commun.* **2015,** 6, 7497.

28. Meloni, S.; Moehl, T.; Tress, W.; Franckevičius, M.; Saliba, M.; Lee, Y. H.; Gao, P.; Nazeeruddin, M. K.; Zakeeruddin, S. M.; Rothlisberger, U.; Graetzel, M. *Nat. Commun.* **2016,** 7, 10334.

29. Xiao, Z.; Yuan, Y.; Shao, Y.; Wang, Q.; Dong, Q.; Bi, C.; Sharma, P.; Gruverman, A.; Huang, J. *Nature Mater.* **2015,** 14, (2), 193-198.

30. Wang, G.; Li, D.; Cheng, H.-C.; Li, Y.; Chen, C.-Y.; Yin, A.; Zhao, Z.; Lin, Z.; Wu, H.; He, Q.; Ding, M.; Liu, Y.; Huang, Y.; Duan, X. *Sci. Adv.* **2015,** 1, (9).

31. Cao, D. H.; Stoumpos, C. C.; Malliakas, C. D.; Katz, M. J.; Farha, O. K.; Hupp, J. T.; Kanatzidis, M. G. *APL Mater.* **2014,** 2, (9), 091101.

32. Lee, S. Y.; Kim, U. J.; Chung, J.; Nam, H.; Jeong, H. Y.; Han, G. H.; Kim, H.; Oh, H. M.; Lee, H.; Kim, H.; Roh, Y.-G.; Kim, J.; Hwang, S. W.; Park, Y.; Lee, Y. H. *ACS Nano* **2016,** 10, (6), 6100-6107.

33. Chin, X. Y.; Cortecchia, D.; Yin, J.; Bruno, A.; Soci, C. *Nat. Commun.* **2015,** 6, 7383.

34. Yuan, Y.; Huang, J. *Acc. Chem. Res.* **2016,** 49, (2), 286-293.

35. Liu, Y.; Wu, H.; Cheng, H.-C.; Yang, S.; Zhu, E.; He, Q.; Ding, M.; Li, D.; Guo, J.; Weiss, N. O.; Huang, Y.; Duan, X. *Nano Lett.* **2015,** 15, (5), 3030-3034.

36. Late, D. J.; Liu, B.; Matte, H. S. S. R.; Dravid, V. P.; Rao, C. N. R. *ACS Nano* **2012,** 6, (6), 5635-5641.

J. Figures and legends

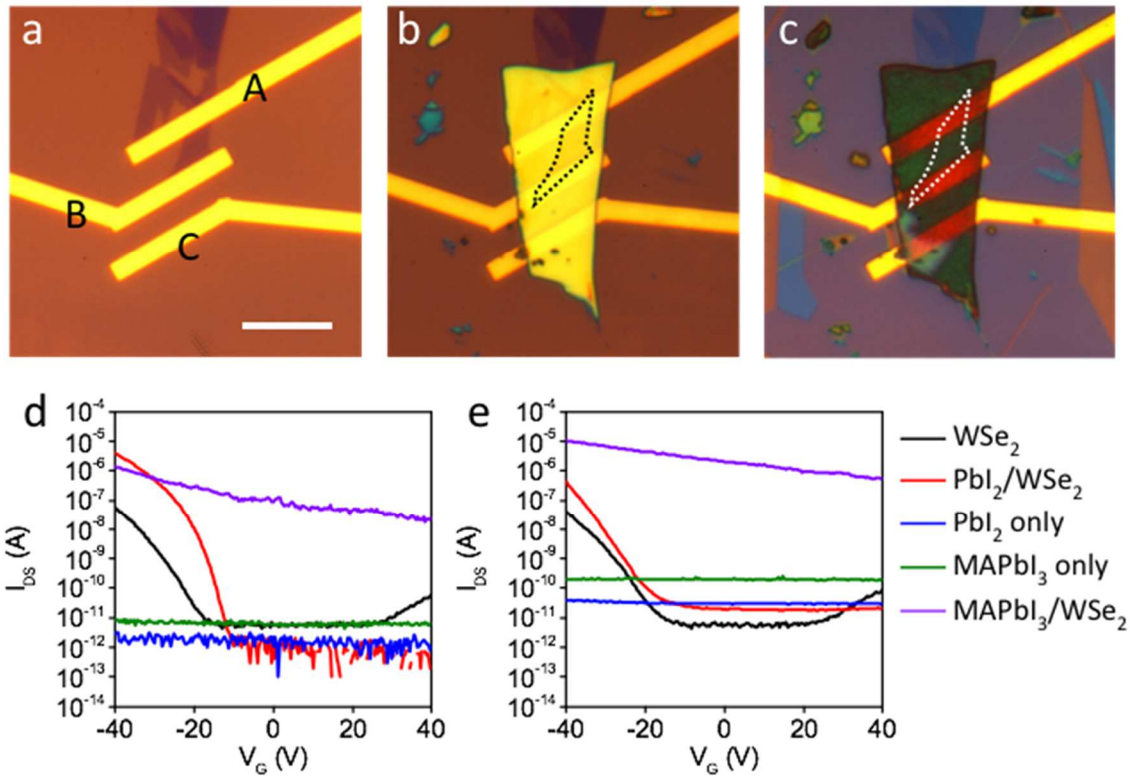

Figure 4-1. The optical images and the transfer curves of monolayer WSe_2, PbI_2, $MAPbI_3$ and PbI_2 ($MAPbI_3$)/WSe_2 hybrid devices.

(a-c) The optical images of as-fabricated WSe_2, PbI_2/WSe_2 hybrid, $MAPbI_3/WSe_2$ hybrid devices, respectively. The white scale bar in (a) is 10 μm. The black (b) and white (c) dashed frames indicate the position of WSe_2 monolayer. (d) The transfer curves of each device measured under dark condition. (e) The transfer curves (plot in the same scale with (d)) of each devices measured under white light illumination.

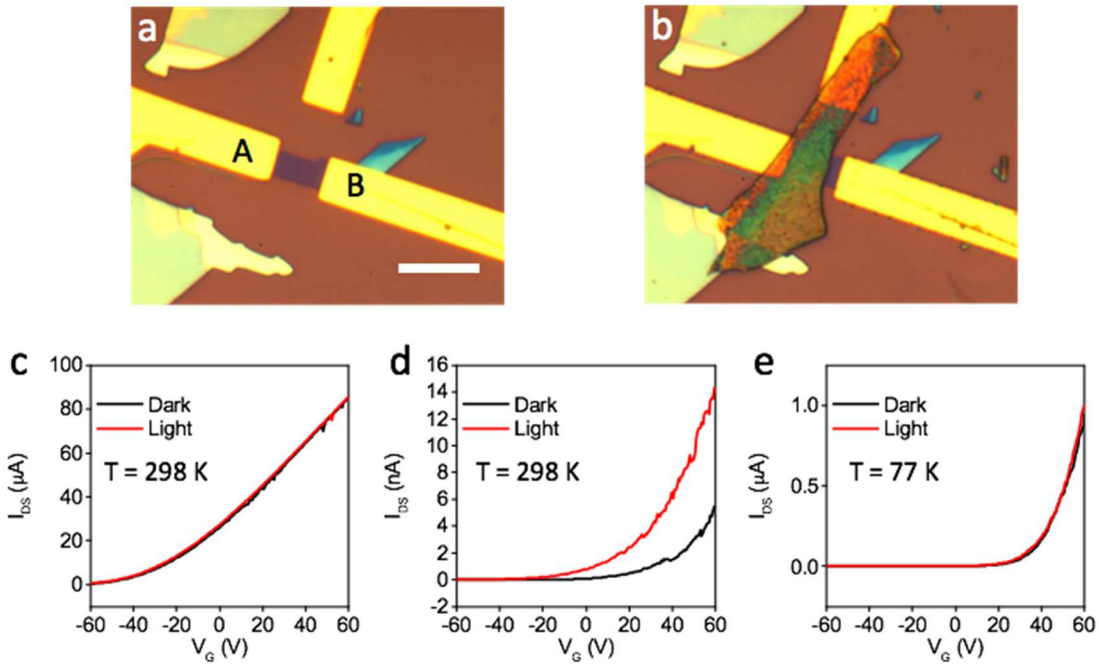

Figure 4-2. The optical images and transfer curves of partially doped MoS_2 FET.

(a,b) The optical image of a monolayer MoS_2 FET before (a) and after MAPbI3 integration (b). (c-e) The transfer curves of MoS_2 device measured at room temperature (c,d) and 77 K (e) before and after $MAPbI_3$ integration, respectively. The black and red curves represent the measurement conducted under dark and illuminated conditions, respectively.

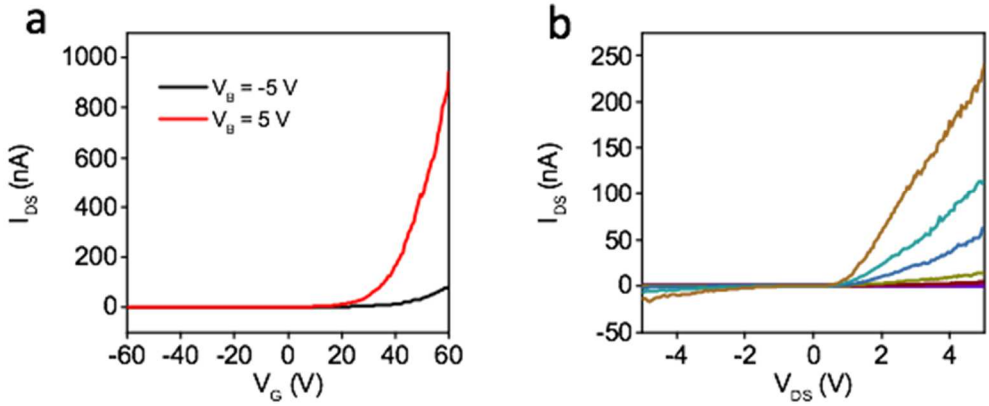

Figure 4-3. The transfer curves and output characteristics of a partially doped MoS_2.

(a,b) The transfer (a) and output (b) curves measured under dark condition. The positive bias voltages show larger gate-modulation.

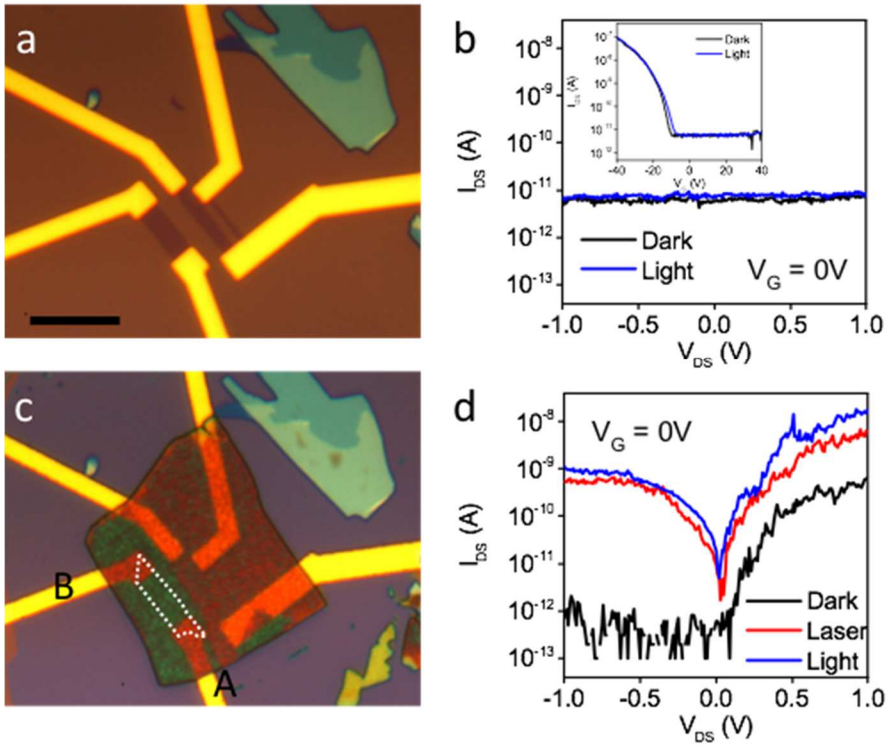

Figure 4-4. The optical images and the output characteristics of a monolayer WSe_2 FET and $MAPbI_3/WSe_2$ hybrid FET.

(a) The optical image of a WSe_2 FET device. (b) The output characteristics of the device shown in (a) when V_G = 0 V. The inset depicts the transfer curves of WSe_2 FET. (c) The optical image of the device shown in (a) after $MAPbI_3$ integration and BN encapsulation. The bias voltage is applied to A with B electrode grounded. (d) The I_{DS}-V_{DS} characteristics of the hybrid device shown in (c) measured under dark, laser (532 nm), light (white light illumination). An initial asymmetry contact was observed due to a small poling effect when bias voltage was applied.

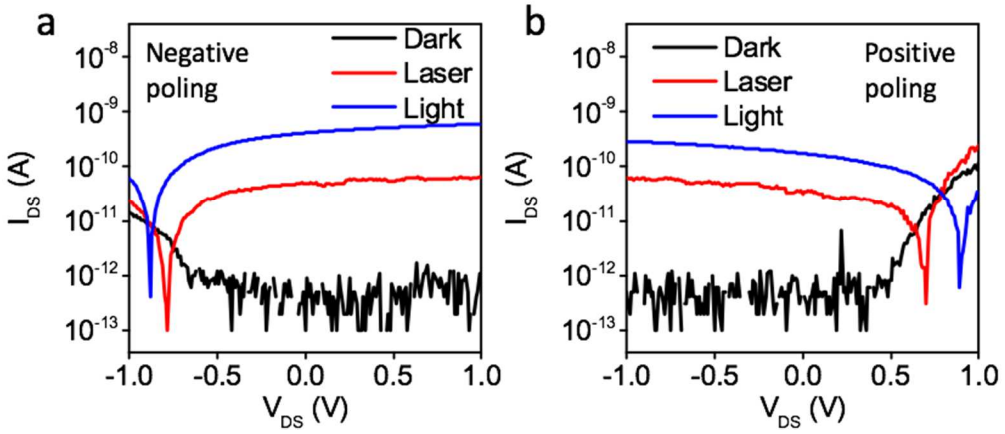

Figure 4-5. The I_{DS}-V_{DS} curves under dark, laser and light condition after negative/positive poling process.

(a,b) The I_{DS}-V_{DS} curves measured after negative (-10 V) or positive (+10 V) poling process under dark, laser (532 nm) and white light excitation, respectively.

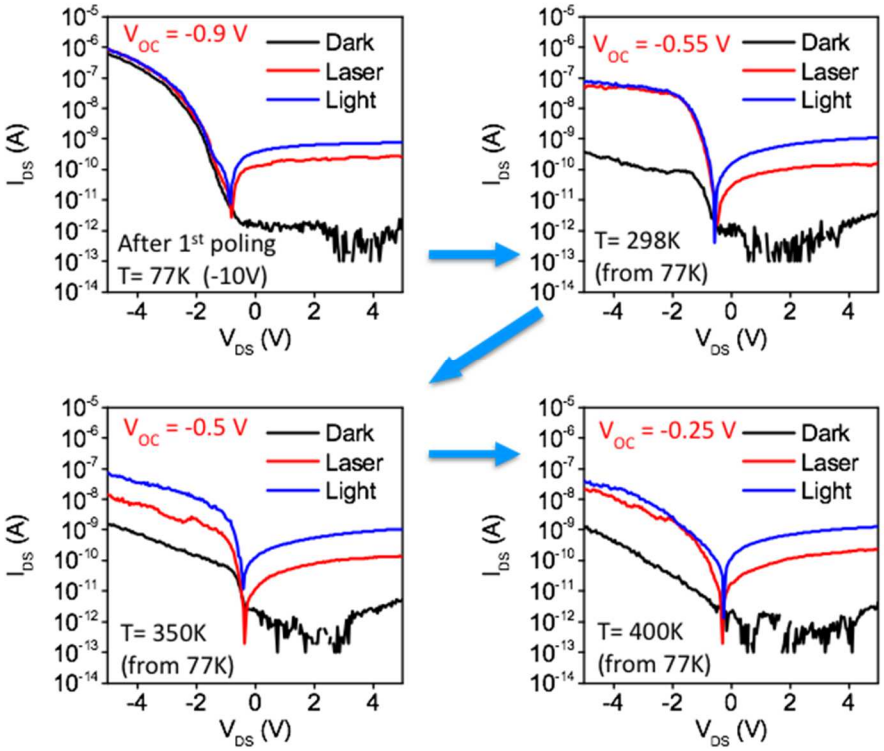

Figure 4-6. Thermal stability of the created p-n junction on $MAPbI_3/WSe_2$ hybrid device.

These output curves shows how the p-n junction (created by negative poling) affect by temperature. The blue arrows indicate the order of process.

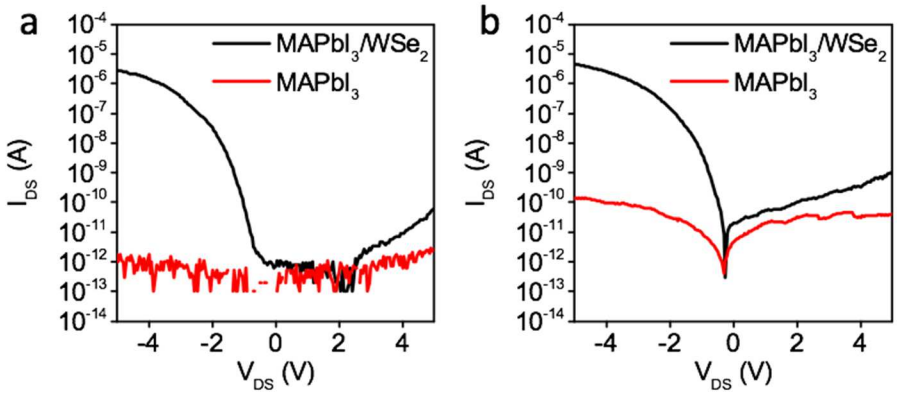

Figure 4-7. The comparison of diode behaviors in $MAPbI_3/WSe_2$ and $MAPbI_3$ device.

(a,b) The output curves measured under dark (a) and 532 nm laser excitation (b). Compared to $MAPbI_3/WSe_2$ hybrid device, the $MAPbI_3$ device shows negligible diode behaviors.

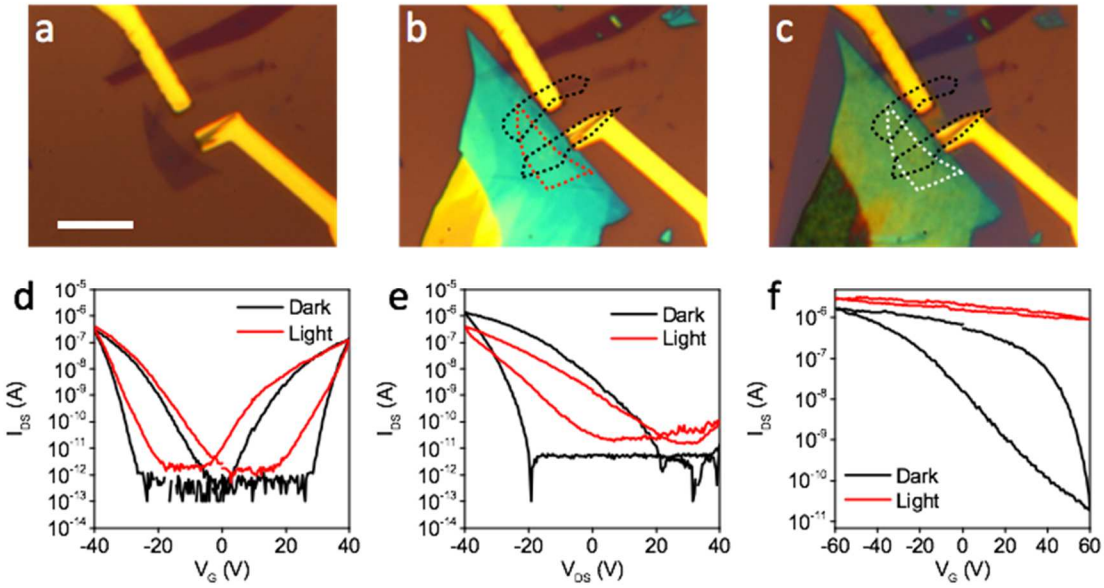

Figure 4-8. The optical images of the graphene-contacted $MAPbI_3/WSe_2$ hybrid device.

(a-c) The optical images of a monolayer WSe_2 device, after PbI_2 and after conversion to $MAPbI_3$, respectively. (d-e) The transfer curves measured under corresponding status listed in (a-c), respectively.

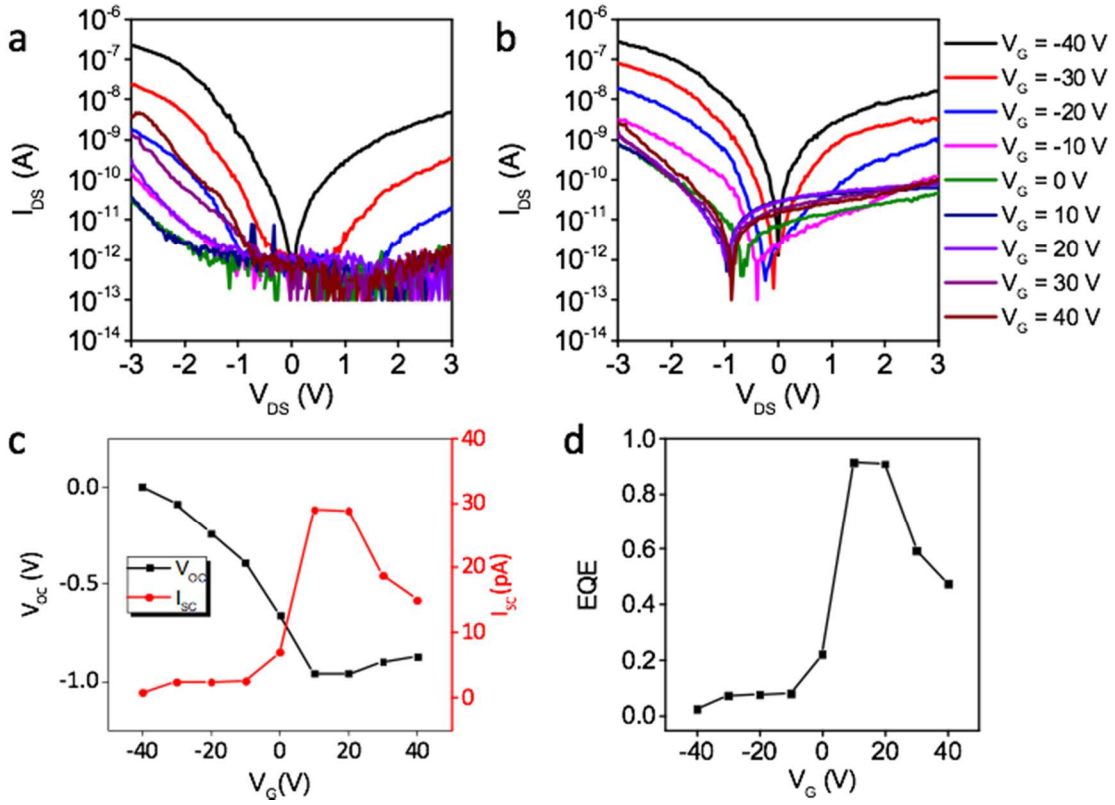

Figure 4-9. The optoelectronic properties of graphene contacted $MAPbI_3/WSe_2$ hybrid device.

(a,b) The output characteristics of the $MAPbI_3/WSe_2$ hybrid device shown in Figure 4-8 measured under dark (a) and laser excitation (b) after negative poling process. (c) The gate-dependent open-circuit voltage (V_{OC}) and short-circuit current (I_{SC}) extracted from (b). The gate-tunable EQE extracted from (c).

CHAPTER V: PERSPECTIVE

The rise of graphene and other two-dimensional materials (2DLMs) has triggered a rapid development of van der Waals heterostructure (vdWH) devices.[1-3] Held by weak van der Waals forces, these artificial vdWHs allow highly disparate materials to restack and combine in desired sequences without the constraints of lattice matching issues in conventional heterostructures. The atomically thin layers and dangling-bond-free surface of 2DLMs ensure a nearly ideal heterointerface, which has enabled several unprecedented device structures, including the atomically sharp vertical junctions and quantum wells,[4-9] the scattering-free substrate for high-mobility transport,[10, 11] and the barrier-free and tunable electrical contact,[5-7, 12, 13] etc. These structures are specifically designed to fulfill different applications.

For example, a large ON-OFF ratio is usually required for the designs of transistors. In the basic 2DLMs based transistors, planar designs are usually adopted,[14] in which the gate-field is perpendicular to the channel, similar to the conventional MOSFET (metal-oxide-semiconductor field-effect transistor). On the other hand, in vertical transistor architecture, the gate-field is parallel to the vertical channel (as shown in Figure 1-6). Such a configuration is favorable due to its high current density and ultrashort channel length that is solely determined by the thickness of channel materials instead of lithographic resolution. As we have discussed in Chapter I, the switching behaviors in vertical transistors are largely controlled by the barrier height between graphene and semiconducting channel.[5-7, 12, 15, 16] The further improvement can be implemented by inserting a charge-injection-control layer as we have discussed in Chapter III, which involves a combination of a Schottky barrier and a tunable p-n junction.[7] The design rules

for vertical transistors are based on the gate-tunable barriers, which are fundamentally different from the conventional planar transistors that are controlled *via* channel pinch-off.

The vertical vdWHs devices are particularly beneficial for optoelectronic applications due to the larger photoactive area compared to planar configuration. In order to build high performance vdWHs optoelectronic devices, semiconducting 2D crystals are generally used as the active materials, while graphene can serve as the top transparent electrode (allowing penetration of light) and the bottom electrode (for gate-modulation). The efficient light-harvesting and detection devices require enough optical absorption, along with an effective separation and extraction of photo-generated electron-hole pairs. In this regard, an internal electric field can be created by asymmetric contacts at top and bottom electrodes due to a slight work function difference between top and bottom graphene. As the light is incident on the top graphene electrode, an appreciable photocurrent under zero-bias condition can be measured, which could even be enhanced by adjusting the work function of bottom graphene *via* gate-field.

The performance of vdWHs optoelectronic devices can be further enhanced by using a direct band gap active materials to replace the semiconducting layer in the stack. In addition to MoS_2 or other transition metal dichalcogenides (TMDCs). The hybrid perovskites, as we have discussed in Chapter II, are the newly emerging direct-gap materials with strong optical absorption.[17] These perovskites can be converted from exfoliated lead halides through vapor phase intercalation.[7, 18] The band gaps and other optical properties of these perovskites can easily be adjusted by the composition.[19] Moreover, the structures of hybrid perovskites can be controlled from bulk to layered structures by intercalating different types of organic molecules.[20, 21] With our water-free

dry transfer and specially designed fabrication process, we are able to build vdWHs devices based on hybrid perovskites and 2D materials. In fact, such perovskite materials not only can serve as photoactive semiconductors, but also efficient light-absorbers and electrically tunable doping agents as we have discussed in Chapter IV.

In the future, the ever-expanding 2DLMs family and the compositionally tunable hybrid perovskites could enable more efficient device designs by selecting well-matched band structures of each layer in the devices. On the other hand, light-emitting devices are also of interest to develop through such vdWHs.[4, 8] Despite such a promising platform offered by vdWHs, scalable fabrication should be developed for future practical applications. The current material transfer techniques have indeed provided quick and proof-of-concept demonstrations, however, the synthetic approaches for the growth of vdWHs are still required for scalable production. In addition, a controllable layer-by-layer etching of 2D materials remains a considerable challenge. Atomic layer etching (ALE),[22] which is the counterpart of atomic layer deposition (ALD), has been used for removing materials layer-by-layer through sequential self-limiting process, might be one possible way to develop. Nevertheless, vdWHs still play very important roles in fundamental studies, as they offer quick assessment and characterization of new heterostructures as well as facilitating the observation of unique physical properties due to atomically smooth interface that are unable to achieve in other heterostructure systems.

A. Reference

1. Liu, Y.; Weiss, N. O.; Duan, X.; Cheng, H.-C.; Huang, Y.; Duan, X. *Nature Reviews Materials* **2016,** 1, 16042.
2. Geim, A. K.; Grigorieva, I. V. *Nature* **2013,** 499, (7459), 419-425.
3. Novoselov, K. S.; Mishchenko, A.; Carvalho, A.; Castro Neto, A. H. *Science* **2016,** 353, (6298).
4. Withers, F.; Del Pozo-Zamudio, O.; Schwarz, S.; Dufferwiel, S.; Walker, P. M.; Godde, T.; Rooney, A. P.; Gholinia, A.; Woods, C. R.; Blake, P.; Haigh, S. J.; Watanabe, K.; Taniguchi, T.; Aleiner, I. L.; Geim, A. K.; Fal'ko, V. I.; Tartakovskii, A. I.; Novoselov, K. S. *Nano Lett.* **2015,** 15, (12), 8223-8228.
5. Yu, W. J.; Li, Z.; Zhou, H.; Chen, Y.; Wang, Y.; Huang, Y.; Duan, X. *Nature Mater.* **2013,** 12, (3), 246-252.
6. Georgiou, T.; Jalil, R.; Belle, B. D.; Britnell, L.; Gorbachev, R. V.; Morozov, S. V.; Kim, Y.-J.; Gholinia, A.; Haigh, S. J.; Makarovsky, O.; Eaves, L.; Ponomarenko, L. A.; Geim, A. K.; Novoselov, K. S.; Mishchenko, A. *Nature Nanotech.* **2013,** 8, (2), 100-103.
7. Cheng, H.-C.; Wang, G.; Li, D.; He, Q.; Yin, A.; Liu, Y.; Wu, H.; Ding, M.; Huang, Y.; Duan, X. *Nano Lett.* **2016,** 16, (1), 367-373.
8. Withers, F.; Del Pozo-Zamudio, O.; Mishchenko, A.; Rooney, A. P.; Gholinia, A.; Watanabe, K.; Taniguchi, T.; Haigh, S. J.; Geim, A. K.; Tartakovskii, A. I.; Novoselov, K. S. *Nature Mater.* **2015,** 14, (3), 301-306.

9. Jariwala, D.; Sangwan, V. K.; Wu, C.-C.; Prabhumirashi, P. L.; Geier, M. L.; Marks, T. J.; Lauhon, L. J.; Hersam, M. C. *Proc Natl Acad Sci USA* **2013,** 110, (45), 18076-18080.
10. Dean, C. R.; Young, A. F.; MericI; LeeC; WangL; SorgenfreiS; WatanabeK; TaniguchiT; KimP; Shepard, K. L.; HoneJ. *Nature Nanotech.* **2010,** 5, (10), 722-726.
11. Wang, L.; Meric, I.; Huang, P. Y.; Gao, Q.; Gao, Y.; Tran, H.; Taniguchi, T.; Watanabe, K.; Campos, L. M.; Muller, D. A.; Guo, J.; Kim, P.; Hone, J.; Shepard, K. L.; Dean, C. R. *Science* **2013,** 342, (6158), 614.
12. Yu, W. J.; Liu, Y.; Zhou, H.; Yin, A.; Li, Z.; Huang, Y.; Duan, X. *Nature Nanotech.* **2013,** 8, (12), 952-958.
13. Liu, Y.; Wu, H.; Cheng, H.-C.; Yang, S.; Zhu, E.; He, Q.; Ding, M.; Li, D.; Guo, J.; Weiss, N. O.; Huang, Y.; Duan, X. *Nano Lett.* **2015,** 15, (5), 3030-3034.
14. RadisavljevicB; RadenovicA; BrivioJ; GiacomettiV; KisA. *Nature Nanotech.* **2011,** 6, (3), 147-150.
15. Britnell, L.; Gorbachev, R. V.; Jalil, R.; Belle, B. D.; Schedin, F.; Mishchenko, A.; Georgiou, T.; Katsnelson, M. I.; Eaves, L.; Morozov, S. V.; Peres, N. M. R.; Leist, J.; Geim, A. K.; Novoselov, K. S.; Ponomarenko, L. A. *Science* **2012,** 335, (6071), 947.
16. Yang, H.; Heo, J.; Park, S.; Song, H. J.; Seo, D. H.; Byun, K.-E.; Kim, P.; Yoo, I.; Chung, H.-J.; Kim, K. *Science* **2012,** 336, (6085), 1140.
17. Im, J.-H.; Lee, C.-R.; Lee, J.-W.; Park, S.-W.; Park, N.-G. *Nanoscale* **2011,** 3, (10), 4088-4093.

18. Wang, G.; Li, D.; Cheng, H.-C.; Li, Y.; Chen, C.-Y.; Yin, A.; Zhao, Z.; Lin, Z.; Wu, H.; He, Q.; Ding, M.; Liu, Y.; Huang, Y.; Duan, X. *Sci. Adv.* **2015,** 1, (9).
19. Jeon, N. J.; Noh, J. H.; Yang, W. S.; Kim, Y. C.; Ryu, S.; Seo, J.; Seok, S. I. *Nature* **2015,** 517, (7535), 476-480.
20. Tsai, H.; Nie, W.; Blancon, J.-C.; Stoumpos, C. C.; Asadpour, R.; Harutyunyan, B.; Neukirch, A. J.; Verduzco, R.; Crochet, J. J.; Tretiak, S.; Pedesseau, L.; Even, J.; Alam, M. A.; Gupta, G.; Lou, J.; Ajayan, P. M.; Bedzyk, M. J.; Kanatzidis, M. G.; Mohite, A. D. *Nature* **2016,** 536, (7616), 312-316.
21. Stoumpos, C. C.; Cao, D. H.; Clark, D. J.; Young, J.; Rondinelli, J. M.; Jang, J. I.; Hupp, J. T.; Kanatzidis, M. G. *Chem. Mater.* **2016,** 28, (8), 2852-2867.
22. Kanarik, K. J.; Lill, T.; Hudson, E. A.; Sriraman, S.; Tan, S.; Marks, J.; Vahedi, V.; Gottscho, R. A. *Journal of Vacuum Science & Technology A* **2015,** 33, (2), 020802.